ISBN 978-82-326-6570-9 (printed ver.)
ISBN 978-82-326-5716-2 (electronic ver.)
ISSN 1503-8181 (printed ver.)
ISSN 2703-8084 (electronic ver.)

Kristian Forfot Sagmo

Doctoral thesis

Doctoral theses at NTNU, 2021:42

NTNU
Norwegian University of
Science and Technology
Thesis for the degree of
Philosophiae Doctor
Faculty of Engineering
Department of Energy and Process Engineering

NTNU
Norwegian University of
Science and Technology

NTNU

Doctoral theses at NTNU, 2021:42

Kristian Forfot Sagmo

Trailing edge vortex shedding in hydraulic turbines and the effect of stream-wise vorticity on vortex induced vibrations

NTNU
Norwegian University of
Science and Technology

Kristian Forfot Sagmo

Trailing edge vortex shedding in hydraulic turbines and the effect of stream-wise vorticity on vortex induced vibrations

Thesis for the degree of Philosophiae Doctor

February 2021

Norwegian University of Science and Technology
Faculty of Engineering
Department of Energy and Process Engineering

NTNU
Norwegian University of
Science and Technology

NTNU
Norwegian University of Science and Technology

Thesis for the degree of Philosophiae Doctor

Faculty of Engineering
Department of Energy and Process Engineering

ISBN 978-82-326-6570-9 (printed ver.)
ISBN 978-82-326-5716-2 (electronic ver.)
ISSN 1503-8181 (printed ver.)
ISSN 2703-8084 (electronic ver.)

Doctoral theses at NTNU, 2021:42

PRINTED IN
NORWAY
NO - 1598

NORDIC SWAN ECOLABEL
Printed matter
2041 0731

Printed by Skipnes Kommunikasjon AS

'All models are wrong, but some models are useful'
- George Box (1919-2013)

To my family

Preface

This thesis is submitted in partial fulfillment of the requirements for the degree of *Philosophiae Doctor* at the Norwegian University of Science and Technology (NTNU). The research was conducted at the Waterpower Laboratory at the Department of Energy and Process Engineering. A substantial part of the work is considered a natural progression of the research activities of the Francis-99 project hosted at the laboratory. In addition, much of the experimental equipment was funded by the HiFrancis project, also affiliated with the laboratory. The work was funded in part by NTNU and in part by the research center HydroCen. The project has been carried out under the main supervision of Associate Professor Pål-Tore S. Storli and co-supervision of Professor Ole Gunnar Dahlhaug at the department.

The thesis is a collection of four papers, presented in chronological order of writing. A summary part precedes the string of papers, linking the papers together and providing background information as well as motivation for the work. The common theme for the articles is passive flow manipulation especially relevant for control of trailing edge vortex shedding in hydraulic machinery.

Acknowledgements

First of all let me extend my gratitude towards my supervisors Pål-Tore Storli and Ole Gunnar Dahlhaug, for entrusting me with this work and for all their support and feedback regarding the different projects. I would also like to extend my gratitude to the technicians and staff at the Waterpowerlab for their help with setting up and acquiring some of the measurement equipment. In particular, thank you to Halvor Haukvik, for all your help with milling designs and mounting of sensors. Thanks to my friends and colleagues at the Waterpowerlab for providing such a welcoming and fun place to work. It's been a pleasure working with you all. My sincerest thanks to my family for their unwavering support through the years and for what probably seemed like a "never-ending" pursuit of studies. Finally, thanks to my partner, Claudia, for all your patience and understanding during my work at the lab and time of writing. It has meant a lot.

Kristian F. Sagmo
Trondheim, February 2021

Abstract

Experiments as well as some numerical simulations were conducted investigating the resonance region of vortex induced vibrations for different trailing edges of a hydrofoil in channel flow. The study focuses on the usefulness of stream-wise vorticity for the mitigation of vortex induced vibrations for the different trailing edge geometries. Though applicable to several different engineering disciplines, the topic is pursued in the context of hydraulic machinery. To this end, flow measurements were also conducted in the vane-less space of a high head model Francis turbine, to investigate the role trailing edge modifications of guide-vanes might play in such machines.

The flows were studied by use of particle image velocimetry. In the case of the individual hydrofoil vibrations were measured by means of embedded strain gauges for different trailing edge geometries. Purely computational fluid dynamics simulations were carried out to investigate different Reynolds-averaged Navier-Stokes based turbulence models capability to predict vortex shedding frequencies and wake velocity profiles for one geometry considered to be representative for hydrofoils utilized in hydraulic turbines.

Most notably, it was found that stream-wise vortexes, here introduced by the means of sub-boundary layer vortex generators, can substantially reduce the amplitudes of the vortex induced vibrations for a hydrofoil, even under resonant conditions. The set of measurements and initial numerical simulations lay the ground-work for further investigations and optimizations of such passive flow control devices.

List of Papers

The following is a list of papers which constitute the main body of work contained in this thesis.

Paper I

K. F. Sagmo, E. O. Tengs, C. W. Bergan and P.-T. Storli "PIV measurements and CFD simulations of a hydrofoil at lock-in". In: *IOP Conference Series: Earth and Environmental Science*. Vol. 240, (2019), pp. 062006. DOI: 10.1088/1755-1315/240/6/062006.

Paper II

K. F. Sagmo and P.-T. Storli "A test of the $v^2 - f\ k - \epsilon$ turbulence model for the prediction of vortex shedding in the Francis-99 hydrofoil test case". In: *Journal of Physics: Conference Series*. Vol. 1296, (2019), pp. 012004. DOI: 10.1088/1742-6596/1296/1/012004.

Paper III

K. F. Sagmo, A. Mærlie and P.-T. Storli "Particle image velocimetry measurements in the vaneless space of a model Francis turbine under steady state operation". Accepted for publication in: *Conference Series: Earth and Environmental Science as part of the (postponed) 30th IAHR Symposium of Hydraulic Machinery and Systems.*

Paper IV

K. F. Sagmo and P.-T. Storli "An experimental study regarding the effect of streamwise vorticity on trailing edge vortex induced vibrations of a hydrofoil". *To be submitted.*

Additional Papers

The following list of papers constitute work that the author has contributed to within the time-frame of the thesis work and that has some relevance to the present work, either through topic or methodology, but is not covered as part of the thesis.

Paper A

J. Bartl, K. F. Sagmo, T. Bracchi and L. Sætran “Performance of the NREL S826 airfoil at low to moderate Reynolds numbers—A reference experiment for CFD models”. In: *European Journal of Mechanics - B/Fluids*. Vol. 75, (2019), pp. 180-192. DOI: https://doi.org/10.1016/j.euromechflu.2018.10.002.

Paper B

E. Volent, K. Sagmo, B. W. Solemslie and O. G. Dahlhaug “Experimental Study of Flow Structure in Converging–Diverging Axisymmetric Geometry”. In: *Journal of Fluids Engineering*. Vol. 142, (2020), pp. 044501-6. DOI: 10.1115/1.4045853.

Paper C

H. Besirovic, K. F. Sagmo and P.-T. Storli “Vortex generator’s effect on trailing edge vortex shedding and fluid structure interaction”. In: *Journal of Physics: Conference Series*. Vol. 1608, (2020), pp. 012002. DOI: 10.1088/1742-6596/1608/1/012002.

Contents

List of Figures

List of Tables

Nomenclature

List of Abbreviations

2C	2-component
2D	2-Dimensional
3D	3-Dimensional
CFD	Computational fluid dynamics
DES	Detached eddy simulation
FFT	Fast Fourier transform
FOV	Field of view
GCI	Grid convergence index
IA	Interrogation area
IW	Interrogation window (same as interrogation area)
LD-V	Laser doppler vibrometer
LES	Large eddy simulation
PIV	Particle image velocimetry
PTV	Particle tracking velocimetry
RANS	Reynolds-averaged Navier-Stokes
RSI	Rotor stator interaction
SAS	Scale adaptive simulation
SST	Shear stress transport
URANS	Unsteady Reynolds-averaged Navier-Stokes
VG	Vortex generator
VIV	Vortex induced vibration

List of Symbols

β^*	Turbulence model constant

δ_{ij}	Kronecker delta	[-]
ϵ	Turbulent dissipation rate	[m^2/s^3]
ν_t	Eddy viscosity, turbulent viscosity	[m^2/s]
ρ	Density	[kg/m^3]
$\tilde{u}, \tilde{v}, \tilde{w}$	Instantaneous velocity components along x, y, and z axis, respectively	[m/s]
ε	Correction factor	[-]
ε'	Small corrector value	
$\vec{u}$	Velocity vector (instantaneous)	[m/s]
C_μ	Turbulence model constant	
c_μ	Turbulence model constant	
d	Diameter, or characteristic thickness	[m]
dt	Time difference	[s]
f	Frequency[1]	[1/s]
H	Height	[m]
I	Light intensity distribution	
i, j, n	Dummy indices	
k	Turbulent kinetic energy	[m^2/s^2]
L	Characteristic length	[m]
R	Discrete cross-correlation function	
r	Residual value	[m/s] or [px]
$r*$	Normalized residual value	[-]
R_p	Discrete cross-correlation function peak	
r_{med}	Residual median value	[m/s] or [px]
S	Scaling function	[m/px]
SI	Strain intensity	[-]
St	Strouhal number	[-]

---

[1] Except in the context of the $v^2 - f$ $k - \epsilon$ turbulence model

$t_1, t_2...$	Time instances	[s]
TI	Turbulence intensity	[-]
U, V, W	Mean (time-averaged) velocity components along x, y, and z axis, respectively	[m/s]
u, v, w	Fluctuating velocity components along x, y, and z axis, respectively[2]	[m/s]
U^*	Normalized stream-wise velocity	[-]
U_{bulk}	Channel bulk velocity	[m/s]
y^+	Dimensionless wall-normal distance	[-]

---

[2] u', v', w' are also used

Part One - Summary

Chapter 1

Introduction

1.1 Motivation

Self induced vibrations due to vortex shedding is a class of fluid structure interaction phenomena proven to be a pervasive problem in a number of engineering fields. In hydro-power turbines the problem of stay vane cracking due to vortex induced vibrations (VIVs) has been around for many years[1]. In recent years the problem seems aggravated by an increasing interest in pushing the limits of range of operation for such machines. This trend is a response to the increasing fluctuations in the power-market where the proportion of intermittent, renewable energy sources, in particular solar and wind, are on the rise[2, 3]. In addition, the increased demand for energy worldwide, renewable energy in particular, motivates the push for higher energy efficiencies of turbines which may in certain cases lead to reduced material thicknesses in such components as the turbine blades, thus increasing risks of fatigue and cracking.

Improvements in the knowledge and design of mechanical components, such as hydrofoils, with respect to VIVs can lead to substantial cost savings due to reduced risks of mechanical failures, and in the field of hydro-power allow larger ranges of operation. One school of thought that has gained increased interest in recent years, is the study of three-dimensional flow structures in bluff body flows rather than two-dimensional, relevant for the mitigation of VIVs[4–6]. The progression is natural, with the research community having built on decades worth of studies into more two-dimensional flows[7–10] [1]. What's more, on the numerical side increasing computational power has made it possible to study ever more complex structures in fluid-structure interaction phenomena, where previously many flows could only be studied in two dimensions. The effect of stream-wise vorticity on vortex shedding and pressure fluctuations through the modifications of trailing edges has re-emerged in the research community. Examples include both sub-boundary layer vortex generators[11] as well as trailing edge serrations[12], or undulations, both of which is part of the present study. The idea of introducing stream-wise vorticity as a means to passively control the flow is quite old however[13, 14], and overall this suggest that no definitive model has been attained for describing the complex wake interactions taking place, in particular for the fluid-structure interaction case.

---

[1] Of course, all turbulent flows exhibit a three-dimensional nature to some degree so the term "two-dimensional flows" is used here in the loose sense.

1.2 Objectives and limitations to scope

In accordance with the above mentioned motivation, the research question asked at the initiation of the project was the following; can the introduction of stream-wise vorticity reduce the amplitudes of vortex induced vibrations, even at resonance?

Considering that an experimental investigation into the topic would provide essential data for the validation of a numerical approach, but would be relatively limited in the description of the full flow field, a two-pronged approach was selected; one numerical and one experimental. The main objective was to design and conduct a set of experiments that could be used as relevant test cases for studying the effect of stream-wise vorticity on trailing edge vortex shedding and vibration, both in the general case as well as in the applied case. The test cases were here to be represented by flow over a generic hydrofoil with different trailing edge designs for passive flow control, as well as flow downstream a guide-vane in a Francis turbine. Seeing as the experimental investigation would likely prove time-consuming, the objective in the numerical study was merely to initiate an investigation into the state-of the art turbulence models that could be used to accurately predict the trailing edge boundary layer separation and vortex shedding.

In such complex flows as occurs in the separated flow regions in the immediate wake of bluff, or blunt objects, combined with boundary layers of adverse pressure gradients a large eddy simulation[15] (LES) is typically considered the "correct" approach. However, while such an approach is viable for industry relevant Reynolds numbers with todays computers, it is typically far too computationally expensive for iterative design exploration. A detached eddy simulation (DES)[16] would offer a less computationally expensive option, but the important boundary layer effects would still be simulated through unsteady Reynolds-averaged Navier-Stokes (RANS) equations with turbulence models, so the starting point again becomes; which state-of the art turbulence model offers the most accurate results with respect to boundary layer separation and vortex shedding?

With the above in mind the following activities were considered:

- To conduct PIV measurements in the wake of a generic hydrofoil and measurements of strain to serve as a reference case both for further experimental studies with modified trailing edge designs as well as for numerical modelling.

- Test different turbulence models with respect to estimation of wake properties and vortex shedding, in particular such models relevant for future DES of geometries of increasing complexity.

- Design and conduct an experiment analysing the effect of stream-wise vorticity on the vortex induced vibrations of a hydrofoil for a set of modified trailing edges.

- Initiate an experimental investigation of the use of such trailing edge modifications as mentioned above for guide-vanes in a high head Francis turbine.

1.3 Thesis outline

The thesis is presented as a collection of papers and is comprised of two parts. *Part one* aims to provide an overview and summary of the each of the individual works without going into details. *Part two* contains the papers, presented in chronological order, with the following titles:

- PIV measurements and CFD simulations of a hydrofoil at lock-in.
- A test of the $v^2 - f\ k - \epsilon$ turbulence model for the prediction of vortex shedding in the Francis-99 hydrofoil test case.
- Particle image velocimetry measurements in the vane-less space of a model Francis turbine under steady state operation.
- An experimental study regarding the effect of stream-wise vorticity on trailing edge vortex induced vibrations of a hydrofoil.

1.4 Main Research Contributions

The main research contributions can be summarized as follows:

- Experimental particle image velocimetry (PIV) data concerning VIVs of a hydrofoil moving through lock-in provides a valuable validation set for further numerical studies.
- New trailing edge designs tested demonstrate the usefulness of vortex generators (VGs) with respect to the mitigation of VIVs for hydrofoils. The detailed flow measurements obtained provide support for further numerical investigations and potential optimizations.
- The PIV measurements obtained in the vaneless space of a high head francis turbine provide insight into the role of guide-vane vortex shedding and it's wake, with respect to the rotor-stator interaction.

References

[1] Gummer, J. H. and Hensman, P. C., "A review of stayvane cracking in hydraulic turbines", International Water Power and Dam Construction; (United Kingdom) vol. 44, 32–42 (1992).

[2] Bo Yang, Makarov, Y., Desteese, J., Viswanathan, V., Nyeng, P., McManus, B., and Pease, J., “On the use of energy storage technologies for regulation services in electric power systems with significant penetration of wind energy”, 2008 5th International Conference on the European Electricity Market, 1–6 (2008).

[3] IPCC, “Climate change 2014: mitigation of climate change: working group iii contribution to the ipcc fifth assessment report: energy systems”, in (Cambridge University Press, 2015), pp. 511–598.

[4] Bearman, P. and Owen, J., “Reduction Of Bluff-Body Drag and Supression of Vortex Shedding by the introduction of Wavy Separation Lines”, Journal of Fluids and Structures vol. 12, no. 1, 123–130 (1998).

[5] Naghib-Lahouti, A., Doddipatla, L. S., and Hangan, H., “Secondary wake instabilities of a blunt trailing edge profiled body as a basis for flow control”, Experiments in Fluids vol. 52, no. 6, 1547–1566 (2012).

[6] Choi, H., Jeon, W.-P., and Kim, J., “Control of flow over a bluff body”, Annual Review of Fluid Mechanics vol. 40, no. 1, 113–139 (2008).

[7] Toebes, G. H. and Eagleson, P. S., “Hydroelastic Vibrations of Flat Plates Related to Trailing Edge Geometry”, Journal of Basic Engineering vol. 83, no. 4, 671 (1961).

[8] Heskestad, G. and Olberts, D. R., “Influence of Trailing-Edge Geometry on Hydraulic-Turbine-Blade Vibration Resulting From Vortex Excitation”, Journal of Engineering for Power vol. 82, 103–09 (1960).

[9] Bearman, P. W., “Vortex Shedding from Oscillating Bluff Bodies”, Annual Review of Fluid Mechanics vol. 16, no. 1, 195–222 (1984).

[10] Staubli, T. and Rockwell, D., “Pressure fluctuations on an oscillating trailing edge”, Journal of Fluid Mechanics vol. 203, 307–346 (1989).

[11] Lin, J. C., “Review of research on low-profile vortex generators to control boundary-layer separation”, Progress in Aerospace Sciences vol. 38, no. 4, 389–420 (2002).

[12] Thomareis, N. and Papadakis, G., “Effect of trailing edge shape on the separated flow characteristics around an airfoil at low reynolds number: a numerical study”, Physics of Fluids vol. 29, no. 1, 014101 (2017).

[13] Kuethe, A. M., “Effect of streamwise vortices on wake properties associated with sound generation.”, en, Journal of Aircraft vol. 9, no. 10, 715–719 (1972).

[14] Tanner, M., “Reduction of base drag”, Progress in Aerospace Sciences vol. 16, no. 4, 369–384 (1975).

[15] Lesieur, M. and Metais, O., “New Trends in Large-Eddy Simulations of Turbulence”, Annual Review of Fluid Mechanics vol. 28, no. 1, 45–82 (1996).

[16] Spalart, P. R., “Detached-Eddy Simulation”, Annual Review of Fluid Mechanics vol. 41, no. 1, 181–202 (2009).

Chapter 2

Background

2.1 Self induced vibrations due to vortex shedding

Vortex shedding due to the instability of separated shear layers from bluff bodies is present in a vast range of flows, both turbulent and laminar, at a vast range of scales. A rather large scale example is given in Figure 2.1, where a satellite image taken by NASA shows vortex shedding from a island made visible by clouds.

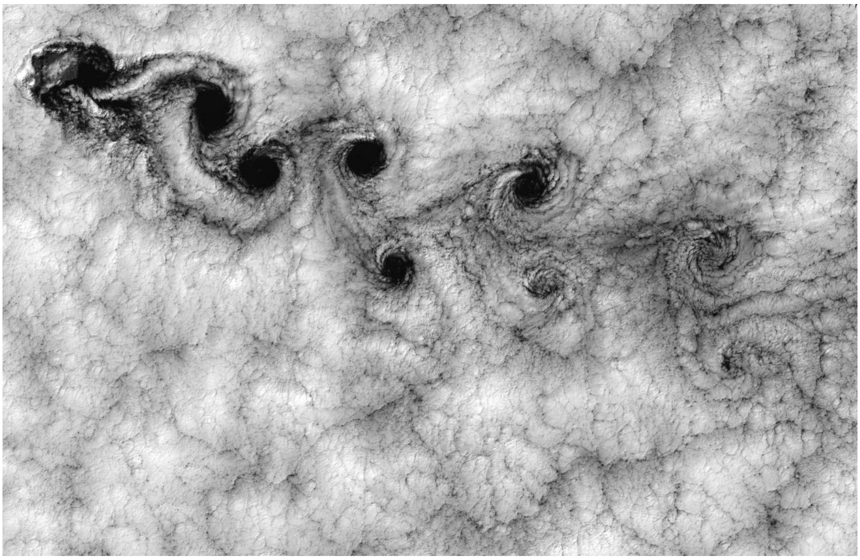

Figure 2.1: von Kármán vortex shedding downstream the Robinson Crusoe Islands, taken by NASA GSFS from Landsat 7 in 1999[1].

The Strouhal relation, $St = fd/U_\infty$, introduced by Vincenc Strouhal[2] is often utilized in engineering practices. For a cylinder of diameter d, in a free-stream velocity of U_∞, with a shedding frequency tending to f, its usefulness is demonstrated in the relatively constant value of around 0.2 across several decades of the diameter based Reynolds number. See for example the compiled data by Hucho et. al.[3]. While the traditional strouhal number attains a fairly constant value for cylinders, different values are found for different geometries. In contrast, Roshko, among others, demonstrated the validity of a universal Strouhal number that has been found to collapse data for bluff body geometries of a wide range of shapes[4–6]. The universal Strouhal number, St' is based on the on the wake properties, essentially the wake width, d', and wake edge velocity,

U', rather than a characteristic dimension of the object positioned within the flow.

Vortex shedding induces an oscillating pressure force which acts on the body generating the separated flow. When the shedding frequency is close the structural natural frequency, resonance may occur[7, 8]. Further, as has been demonstrated for both cylinders and foils[9], the vortex shedding may become locked on the structural natural frequency, rather than linearly increasing with the flow velocity as per the Strouhal relation. In hydraulic turbines this mutual fluid-structure interaction, sometimes referred to as singing vanes[10], can effectively increase the risk of blade cracking or component failure trough widening the velocity range where resonant vibrations can occur.

2.2 Particle Image Velocimetry

The present work makes extensive use of particle image velocimetry (PIV) for the measurement of trailing edge flows and vortex shedding. PIV has gained considerable traction in the research community in recent years[11]. The method relies on the use of tracer particles, acting as sensors, suspended in an otherwise optically transparent fluid. Through the use of a collimated light source and camera an accurate measurement volume can be defined and the tracer particles tracked. Though several types of techniques have been developed, we will here confine ourselves to the description of 2D, 2-component (2D-2C) PIV for digital cameras, which has been used throughout the work of the thesis. Figure 2.2 presents a general overview of the method.

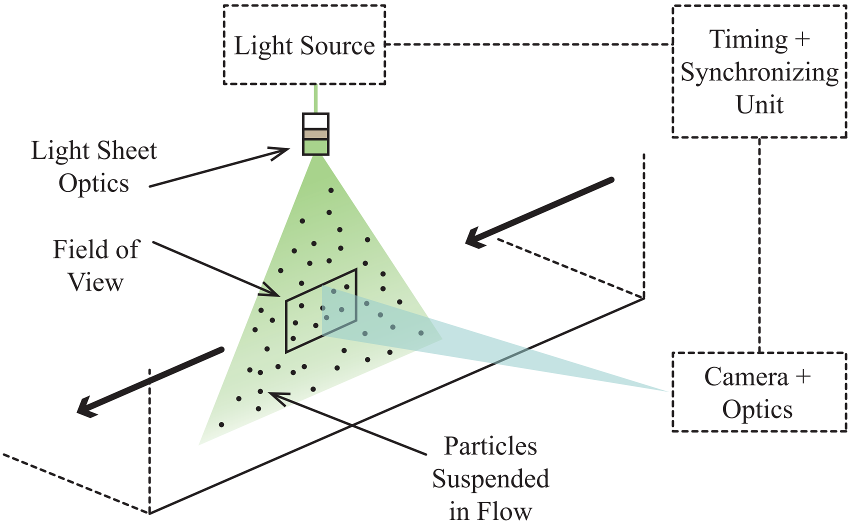

Figure 2.2: A conceptual overview of a generic 2D-2C PIV setup.

This section is only meant as a brief introduction to the essence of the technique and some of it's potential sources of errors. For a complete discussion see for example[12].

2.2.1 Particles

The ideal seeding, or tracer particles for PIV are those that have neutral buoyancy, are much smaller than the smallest scales to be resolved in the flow, does not significantly alter the fluid properties, and does not interact with each other. As PIV is an optical method, it is also clear that the particles should have a minimum degree of reflectivity, where this minimum degree is closely tied to the intensity of the illumination source and the light sensitivity of the camera sensor. It may be worthwhile to note that there will always be an error associated with the discrepancy between the true fluid path, and the path followed by a particle, as illustrated in figure 2.3, though this error may often be neglected[13] for an appropriately conditioned setup.

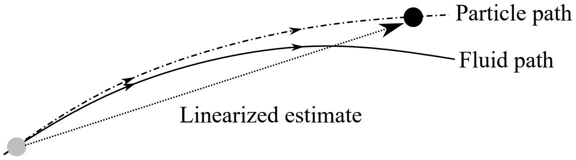

Figure 2.3: Illustration of particle path vs true fluid path and the average displacement.

2.2.2 Spatial correlation

Rather than estimating the velocity of single particles, as in particle tracking velocimetry (PTV), PIV relies on the spatial distribution of particle groups for the estimation of velocities. The full field of view (FOV) particle image is split into smaller interrogation windows (IW), where each interrogation window results in one velocity vector. See figure 2.4.

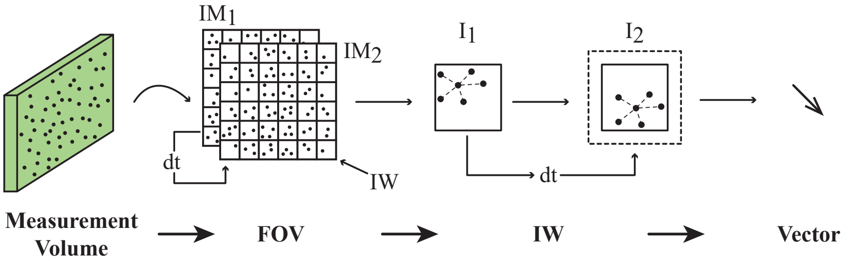

Figure 2.4: Two sets of images make up each vector field. Each image is split into IWs resulting in one vector through cross-correlation evaluation.

Let, $I(x, y)$ denote the 2D distribution of discrete pixel light intensity levels in a single exposure digital image. Then, for two particle image pairs, I_1 and I_2, separated by a known time delay, $dt = t_2 - t_1$, we may define the discrete cross-correlation function[1]

$$R(i, j) = \sum_{x=-L/2}^{L/2} \sum_{y=-H/2}^{H/2} I_1(x, y) I_2(x + i, y + j). \tag{2.1}$$

Here, L and H denote the length and height of the sample size of I_1 in pixels, and the variables i and j represent an image shift along the x and y axis, respectively. To allow this, the sample size of I_2 can be taken larger than I_1, or given some sort of appropriate padding m along x, and n along y, so that $-m \leq i \leq m$ and $-n \leq i \leq n$ [12]. For padding and sample sizes of even numbers, this gives rise to a $(2m+1) \times (2n+1)$ correlation plane. As an example, in the case of a 24 px x 24 px IW, with a uniform padding of 12 px, this would then give a correlation plane of size 25×25 units. Assuming that the shape of the particle spatial distribution remains essentially the same in a subset of I_2 as in I_1, and also is not rotated, both of which is a prerequisite for classical PIV, the spatial cross-correlation will yield a peak, $R_p(i_p, j_p)$ at the linear translation corresponding to the vector

$$\vec{r_p} = \vec{e}_1 i_p + \vec{e}_2 j_p, \tag{2.2}$$

where $\vec{e}_1$ and $\vec{e}_2$ are unit vectors in the x and y direction, respectively. Through applying some scaling function S(X,Y), converting the scale of pixels to dimensions of length, one obtains the first estimate for the velocity vector

$$\vec{u} = \frac{S(X, Y)(\vec{r_p})}{dt}. \tag{2.3}$$

In general the scaling operator depends on the location of the vector in the FOV image plane, here denoted (X, Y), due to optical effects such as lens aberration, or oblique viewing angles for 2D PIV.

In practice, local particle spatial variance and particle image distortion, though hopefully small, as well as intensity distribution differences in the two image pairs means that the cross correlation peak can become smeared out. The uncertainty generally decreases as the size of the IW increases and more particles contribute to the correlation, though this comes at the cost of spatial averaging of the velocity field. Also note that, for computational efficiency, it is customary for PIV algorithms to rely on the fast Fourier transform (FFT) to compute the cross-correlation function, exploiting the cross correlation theorem stating that the cross-correlation can be computed from a complex conjugate multiplication of the Fourier transforms of I_1 and I_2. For efficient implementation, the two image

---

[1] For fair relative comparison between the sample images which may have differences in background intensities and exposure, it is customary to work with the normalized cross-correlation coefficient, rather than the cross-correlation function, but the essence of the method remains the same.

samples are often set to equal size with a base number of 2, e.g. 16 px×16 px or 32 px×32 px, resulting in an equal size correlation-function plane[12]. While this can drastically decrease computational time, the drawback is a potential loss of particle pairs, and a limitation on the dynamic range set by the size of the IW. The solution that has evolved in the PIV research community is to utilize a so-called multi-pass approach with window shifts and shape adaptation, which is further described in section 2.2.4.

2.2.3 Image particle size and density

An issue with the method presented thus far is the fact that the correlation peak is located with discrete pixel steps. This may not always be sufficiently accurate. One common method around it, is to apply a 3-point Gaussian curve fit to the correlation peak[14, 15] and its adjacent correlation values. See figure 2.5

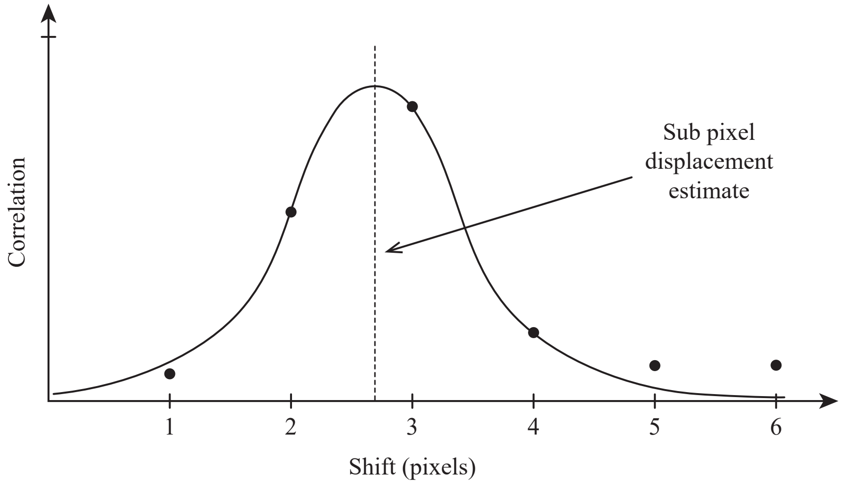

Figure 2.5: A three point Gauss-fit estimator resulting in sub-pixel displacement accuracy.

The rationale behind using a Gaussian curve is that the image of the particles themselves form so-called Airy functions which are well estimated by Gaussian functions. The spatial cross-correlation function is then a correlation of approximately Gaussian functions, which is itself again approximately a Gaussian function. With such an approach, sub-pixel accuracy in the location R_p for a given vector is possible. Through simulations using synthetic particle images, Raffel et al.[12] found the optimal particle size for an accurate Gaussian fit to be in the range of 2-3 pixels in diameter, depending on the PIV algorithm used. This particle size also help to minimize the so-called peak-locking effect, or pixel-locking effect, generally caused by particles being too small. If the particle images are of the size of 1 pixel, then the cross correlation peak can become too narrow, and clear bias towards discrete pixel displacements occur[12, 13]. This effect can be detected by inspecting the histogram of displacement estimates in a PIV FOV. An illustration of the effect is given in figure 2.6.

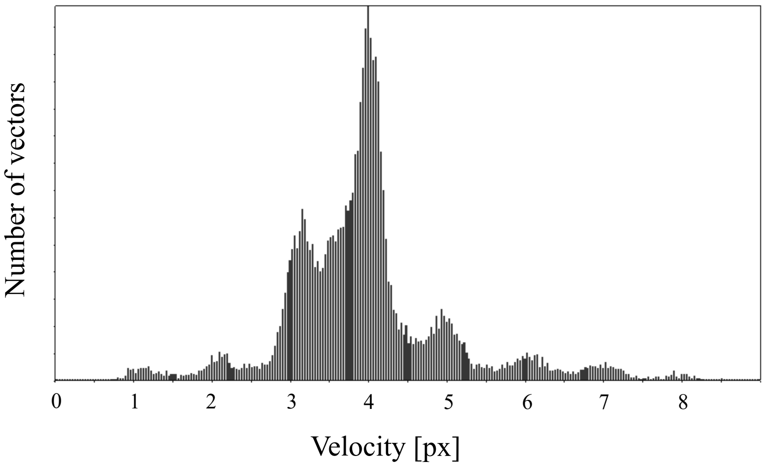

Figure 2.6: An example of vector field peak-locking. There is a clear attenuation towards vectors corresponding to integer pixel displacements.

When it comes to the density of the particles, it is clear that an increase in particle density will contribute to an increase in the cross-correlation function peak amplitude, as long as the particles are clearly distinguishable, i.e. background noise is not increased. In practice, the challenge is often to achieve a high enough, and uniform, particle seeding density. As a rule of thumb a total of 10 particles within a given interrogation window is suggested as an adequate starting point[12] in order to have a sufficient signal to noise ratio in the cross correlation peak and decrease the chance of false positives arising from in and out of plain motion of the tracer particles.

2.2.4 Multi-pass interrogation with window shifting and deformation

PIV has evolved to a point where it is now commonplace for practitioners and software providers to utilize multi-pass IW algorithms, involving both IW window shifting and adaptive IW shape, or weighting[16]. As mentioned, a constant IW size for the image frames associated with the intensity fields I_1 and I_2 is beneficial for computational purposes, but limits the traceable range of particle movements and leads to potential in-plane loss of particle pairs. Multi-pass interrogation window shifting algorithms can allow for larger particle image displacements for a given interrogation window size, and greatly reduces the risk of in-plane particle pair losses[17, 18]. Overall, the method is based on doing an initial pass to estimate the velocity field. Then a second pass shifts the second IW in relation to the first by the most likely velocity vector. Thus, particle movements larger than the size of the IW itself can be tracked, and the risk of in-plane particle pair loss is drastically reduced. Another benefit of the multi-pass procedure is the potential for iterative spatial refinement. For instance one may initiate with a relatively large IW, say 64 by 64 pixels, in order to estimate a particle image displacement, and use that predictor as a first estimate for the peak search in a concurrent evaluation pass for a smaller interrogation window, say 32 by 32 pixels.

Furthermore, as described by for instance Scarano and Riethmuller[19], the multi-pass approach allows an estimation of the relative spatial deformation of the particle distribution from the first image frame to the next. This is done through the initial estimation of the velocity field and subsequent estimation of the spatial derivatives $d\vec{u}/dx$ and $d\vec{u}/dy$. See figure 2.7 for an illustration of the effect of different degrees of multipass prosessing. The correction of the spatial deformation of the particle images greatly decreases the smearing of the cross-correlation peak in high shear and turbulent flows, where spatial gradients may be significant through all the practically obtainable IW sizes.

2.2.5 Recognition of spurious vectors

While several methods exists for the automatic detection of spurious vectors, the one that is relevant for the present work is as presented by Westerweel and Scarano[20]. The proposed method essentially considers the local velocity variations within a neighbourhood of a vector in question, and determines an allowable threshold. If the vector under consideration is outside an allowable threshold it may be discarded as an outlier, and subsequently replaced by a vector corresponding to the next highest peak in the cross-correlation function. The algorithm may be re-iterated, until all detectable spurious vectors have either been replaced, interpolated or simply deleted. The proposed outline is as follows; consider a vector in question of magnitude $|\vec{u}|_{(0)}$. For it's neighbourhood of n vector magnitudes $\{|\vec{u}|_{(1)}, |\vec{u}|_{(2)},...|\vec{u}|_{(n)}\}$ (e.g. n=8 for a 3x3 vector neighbourhood) a median, $|\vec{u}|_{med}$, is computed. Then, a residual value, $r_i = ||\vec{u}|_{(i)} - |\vec{u}|_{med}|$, is determined for each vector in the neighbourhood and a residual median, r_{med}, is computed from $\{r_1,r_2..r_n\}$. The point of using the median rather than the average is that the median is less susceptible to "blow up" due to other spurious vectors in the neighbourhood[21]. Finally the normalized residual level of the vector in question with respect to it's neighbourhood is defined as

$$r_0^* = \frac{||\vec{u}|_{(0)} - |\vec{u}|_{med}|}{r_{med} + \varepsilon'}, \tag{2.4}$$

where ε' is a small correction to avoid a division by 0 in a uniform flow field. For values in pixels, the value suggested for ε' is 0.1 px, which have been found to be a typical level of background noise in digital PIV setups. Westerweel and Scarano[20] went on to demonstrate that a residual level of $r^* < 2$ roughly corresponded to the 90-percentile for a range of PIV data from different flows, which suggested that a universal constant could be used for the detection of outliers.

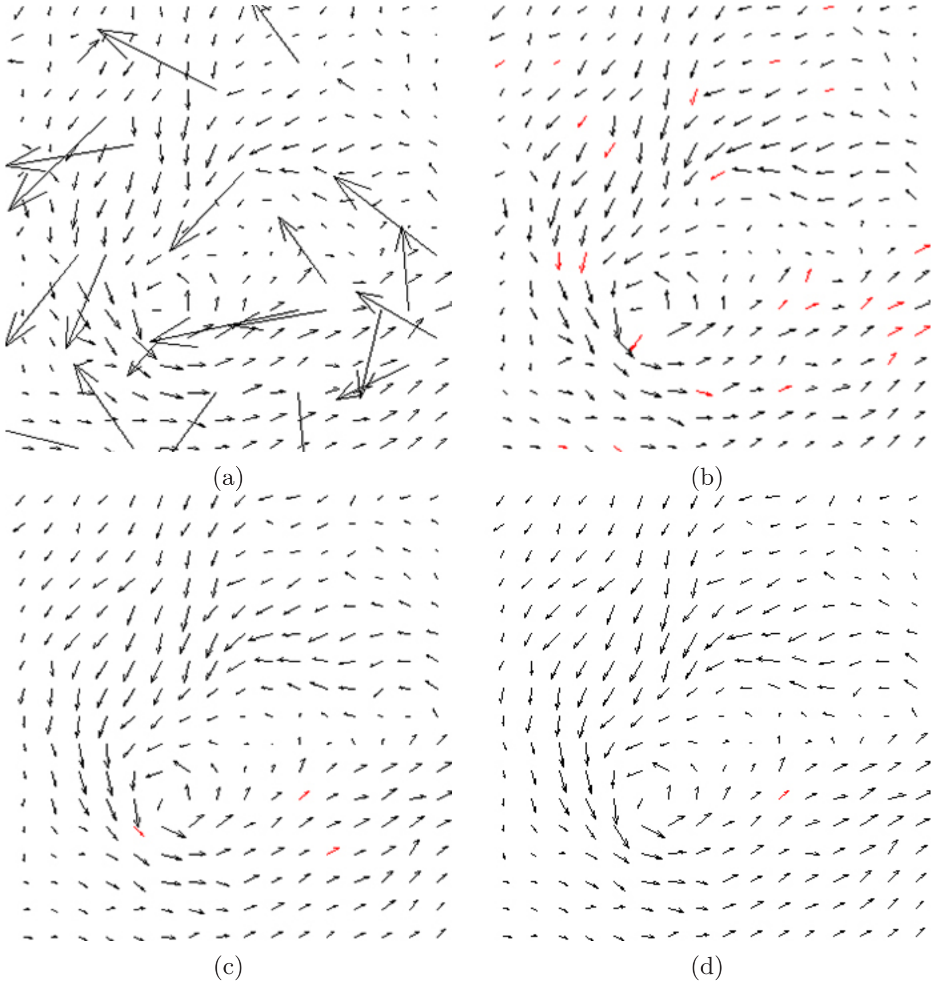

(a) (b)

(c) (d)

Figure 2.7: The same vector-field evaluated with a 16 px x 16 px IW through different approaches. a) shows the vector field with no detection and replacement of spurious vectors. b) shows the field with universal outlier detection applied and replaced vectors in red. In c) a multipass with constant IW approach has been applied, leading to a more robust estimate. d) shows the vectorfield evaluated using a mulitpass approach with decreasing IW size, going from 2 passes with a 24px x 24px to 2 passes with a 16 px x 16 px IW.

2.3 A note on near wall eddy-viscosity turbulence modelling

Through Reynolds decomposing an instantaneous velocity component, $\tilde{u}_i$, into it's mean, U_i, and fluctuating, u_i, components ($i = 1, 2, 3$), and then averaging, the Reynolds-averaged Navier-Stokes (RANS) equations for an incompressible fluid may be written[22]:

$$\frac{\partial}{\partial t}U_i + U_j\frac{\partial}{\partial x_j}U_i = -\frac{1}{\rho}\frac{\partial}{\partial x_i}P + \nabla^2 U_i - \frac{\partial}{\partial x_j}\overline{u_j u_i}, \tag{2.5}$$

$$\frac{\partial}{\partial x_i}U_i = 0, \tag{2.6}$$

representing the conservation of momentum and mass, respectively. In order to solve the set of four equations, closure must be found for the six unknowns of the Reynolds stress tensor $\overline{u_j u_i}$. The main turbulence models utilized in the present work are so called eddy-viscosity turbulence models that relates the Reynolds stress tensor to an eddy, or turbulent kinematic viscosity, ν_t, by the linear constitutive relation called the Boussinesq approximation:

$$\overline{u_j u_i} = -2\nu_t S_{ij} + \frac{2}{3}k\delta_{ij}. \tag{2.7}$$

where $S_{ij} = \frac{1}{2}\{\frac{\partial}{\partial x_i}U_j + \frac{\partial}{\partial x_j}U_i\}$ is the mean rate of strain tensor, δ_{ij} is the Kronecker delta, and $k = \frac{1}{2}\overline{u_i u_i}$ is the turbulent kinetic energy. In the following, let the velocity components be oriented such that $u_2 = v$ is along the wall normal direction, while $u_1 = u$ is along the wall-parallel stream-wise direction and $u_3 = w$ is the resulting cross stream, wall parallel component.

Jones and Launder[23] introduced what is now considered the standard $k - \epsilon$ turbulence model, which may be regarded as the prototype, or starting point, for the other turbulence models herein. In their high Reynolds number version of the model they proposed the limiting form

$$\nu_T = C_\mu \frac{k^2}{\epsilon}, \tag{2.8}$$

for the eddy viscosity. Here ϵ is the turbulent dissipation rate, and $C_\mu = 0.09$ is a model constant. The model then closes the set of equations thus far introduced by solving two transport equations, one for k and one for ϵ, hence it's name. Figure 2.8, adapted from Durbin[22], shows the predicted eddy viscosity according to equation 2.8 in a boundary layer against the "exact" value, using the relation $\nu_t = -\overline{uv}/\frac{dU}{dy}$. Both relations were computed using boundary layer data from the direct numerical simulation by Moser et. al.[24]. The over-prediction of the eddy-viscosity in the near wall region, i.e. y^+ less than roughly 50, is apparent. The additional profile with $C_\mu = 0.08$ demonstrates that the shape cannot be sufficiently altered simply by adjusting C_μ.

A number of ways of adapting the "high Reynolds number" form of the $k - \epsilon$ model to allow for more accurate near wall turbulence modelling has been proposed over the years. Jones and Launder[23] adopted a so-called wall damping function approach for ν_t in the initially proposed model, in addition to a modification of the transport equations of k and ϵ. An review of such models, often called low Reynolds number models due to the increased impact of the molecular viscosity in the near wall region of boundary layers, is provided by Patel et. al.[25]. Another method include the use of wall functions, relying on the universal law of the wall to compute the inner-most region of the boundary,

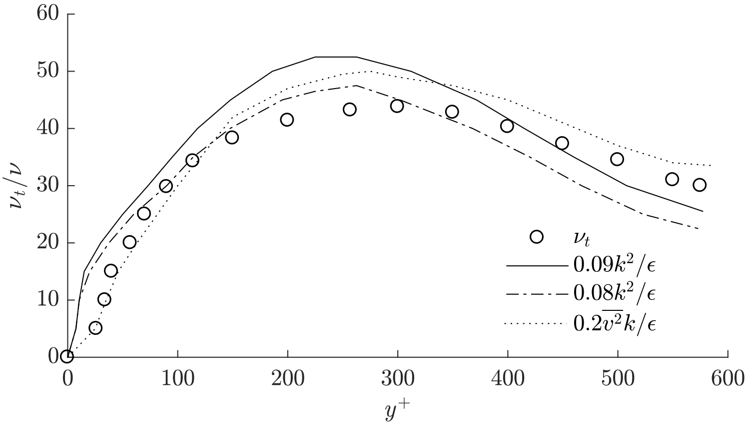

Figure 2.8: Eddy viscosity evaluated according to different relations. Figure adapted from Durbin[22].

and removing the need to spatially resolve the boundary layer below $y^+ \approx 40$. Finally, two-layer models have been developed in the strand of $k-\epsilon$ turbulence models that effectively splits the modelling approach in two; one formulation that handles the near wall region is stitched to a model that handles the rest of the flow region. One such approach is presented in the paper by Chen et. al.[26].

The relatively poor agreement between some of the older near-wall formulations of the $k-\epsilon$ strand of models and boundary layer data for flows with adverse pressure gradients led Wilcox to introduce a reformulation of the transport equations[27, 28]. He introduced the $k-\omega$ strand of turbulence models, by considering the transport of the specific turbulent dissipation rate $\omega = \epsilon/(k\beta^*)$, where β^* is a model constant. One of the notable improvements was that a reasonable distribution of the eddy viscosity was achieved all the way down to the wall, without the use of wall-damping functions. Menter sought to further improve the $k-\omega$ formulation for adverse pressure gradients and separated flows with the introduction of the now popular shear stress transport (SST) formulation[29]. An overview of the $k-\omega$ strand of turbulence models is provided in the more recent paper by Menter[30].

Durbin[31] introduced an eddy viscosity scaling based on the wall normal turbulent stress component, $\overline{v^2}$, such that

$$\nu_t = c_\mu \overline{v^2}\frac{k}{\epsilon}, \tag{2.9}$$

on the grounding that $\overline{v^2}$ is a more physically correct scaling for the turbulent transport to and from the wall. Indeed, when compared to the eddy viscosity profile in figure 2.8, the proposed scaling demonstrates a good match. Note that here a different constant c_μ (=0.2) is used. Seeking to retain some of the near wall anisotropy without the need for a full Reynolds stress transport formulation, Durbin went on to introduce the $k - \epsilon - \overline{v^2} - f$ turbulence model, where f was introduced as an elliptic function aiming to retain the "wall-echo" effects imposed on $\overline{v^2}$ close to an impermeable wall[32]. The model has been tested for a number of cases of 2D and 3D boundary layers with adverse pressure gradients and separation, with overall good results[33, 34]. An overview of the $k - \epsilon - \overline{v^2} - f$ strand of turbulence models is provided in the recent study by Billard and Laurence[35].

References

[1] *NASA Landsat 7 Online Image Library*, NASA Goddard Space Center, 1999.

[2] Strouhal, V., “Uber eine besondere art der tonerregung”, Annalen der Physik vol. 241, no. 10, 216–251 (1878).

[3] Hucho, W.-H., Hannemann, K., Martinez Schramm, J., and Williamson, C., “Aerodynamics”, en, in *Springer Handbook of Experimental Fluid Mechanics*, edited by Tropea, C., Yarin, A. L., and Foss, J. F., Springer Handbooks (Springer, Berlin, Heidelberg, 2007), pp. 1043–1155.

[4] Roshko, A., *On the drag and shedding frequency of two -dimensional bluff bodies*, NACA TECHNICAL NOTE 3169, 1954.

[5] Roshko, A., “On the Wake and Drag of Bluff Bodies”, Journal of the Aeronautical Sciences vol. 22, no. 2, 124–132 (1955).

[6] Griffin, O. M., “A universal Strouhal number for the ‘locking-on’ of vortex shedding to the vibrations of bluff cylinders”, en, Journal of Fluid Mechanics vol. 85, no. 3, 591–606 (1978).

[7] Bearman, P. W., “Vortex Shedding from Oscillating Bluff Bodies”, Annual Review of Fluid Mechanics vol. 16, no. 1, 195–222 (1984).

[8] Williamson, C. and Govardhan, R., “Vortex-Induced Vibrations”, Annual Review of Fluid Mechanics vol. 36, no. 1, 413–455 (2004).

[9] Blake, W. K., “Excitation of Plates and Hydrofoils by Trailing Edge Flows”, Journal of Vibration Acoustics Stress and Reliability in Design vol. 106, no. 3, 351 (1984).

[10] Goldwag, E., “Von Karman Hydraulic Vortexes Cause Stay Vane Cracking on Propeller Turbines at the Little Long Generating Station of Ontario Hydro”, Journal of Engineering for Power, Transactions of the ASME, 213–217 (1968).

[11] Westerweel, J., Elsinga, G. E., and Adrian, R. J., “Particle Image Velocimetry for Complex and Turbulent Flows”, Annual Review of Fluid Mechanics vol. 45, no. 1, 409–436 (2013).

[12] Raffel, M., Willert, C. E., Wereley, S., and Kompenhans, J., *Particle image velocimetry: a practical guide*, edited by Raffel, M., 3’rd ed (Springer, Heidelberg ; New York, 2007).

[13] Westerweel, J., “Fundamentals of digital particle image velocimetry”, Measurement Science and Technology vol. 8, no. 12, 1379–1392 (1997).

[14]Willert, C. E. and Gharib, M., “Digital particle image velocimetry”, Experiments in Fluids vol. 10, no. 4, 181–193 (1991).

[15]Nobach, H. and Honkanen, M., “Two-dimensional Gaussian regression for sub-pixel displacement estimation in particle image velocimetry or particle position estimation in particle tracking velocimetry”, en, Experiments in Fluids vol. 38, no. 4, 511–515 (2005).

[16]Stanislas, M., Okamoto, K., Kähler, C. J., and Westerweel, J., “Main results of the Second International PIV Challenge”, Experiments in Fluids vol. 39, 170–191 (2005).

[17]Westerweel, J., Dabiri, D., and Gharib, M., “The effect of a discrete window offset on the accuracy of cross-correlation analysis of digital PIV recordings”, en, Experiments in Fluids vol. 23, no. 1, 20–28 (1997).

[18]Scarano, F. and Riethmuller, M. L., “Iterative multigrid approach in PIV image processing with discrete window offset”, en, Experiments in Fluids vol. 26, no. 6, 513–523 (1999).

[19]Scarano, F. and Riethmuller, M. L., “Advances in iterative multigrid PIV image processing”, Experiments in Fluids vol. 29, no. 1, S051–S060 (2000).

[20]Westerweel, J. and Scarano, F., “Universal outlier detection for PIV data”, en, Experiments in Fluids vol. 39, no. 6, 1096–1100 (2005).

[21]Westerweel, J., “Efficient detection of spurious vectors in particle image velocimetry data”, Experiments in Fluids vol. 16, 236–247 (1994).

[22]Durbin, P. A. and Reif, B. A. P., *Statistical theory and modeling for turbulent flows*, 2nd ed. (John Wiley & Sons, West Sussex, United Kingdom, 2011).

[23]Jones, W. P. and Launder, B. E., “The prediction of laminarization with a two-equation model of turbulence”, en, International Journal of Heat and Mass Transfer vol. 15, no. 2, 301–314 (1972).

[24]Moser, R. D., Kim, J., and Mansour, N. N., “Direct numerical simulation of turbulent channel flow up to Re_τ=590”, Physics of Fluids vol. 11, no. 4, Publisher: American Institute of Physics, 943–945 (1999).

[25]Patel, V. C., Rodi, W., and Scheuerer, G., “Turbulence models for near-wall and low Reynolds number flows - A review”, AIAA Journal vol. 23, no. 9, 1308–1319 (1985).

[26]Chen, H. C. and Patel, V. C., “Near-wall turbulence models for complex flows including separation”, AIAA Journal vol. 26, no. 6, 641–648 (1988).

[27]Wilcox, D. C., “Reassessment of the scale-determining equation for advanced turbulence models”, AIAA Journal vol. 26, no. 11, Publisher: American Institute of Aeronautics and Astronautics, 1299–1310 (1988).

[28]Wilcox, D. C., “Comparison of two-equation turbulence models for boundary layers with pressure gradient”, AIAA Journal vol. 31, no. 8, 1414–1421 (1993).

[29]Menter, F. R., “Two-equation eddy-viscosity turbulence models for engineering applications”, AIAA journal vol. 32, no. 8, 1598–1605 (1994).

[30] Menter, F. R., “Review of the shear-stress transport turbulence model experience from an industrial perspective”, International Journal of Computational Fluid Dynamics vol. 23, no. 4, Publisher: Taylor & Francis, 305–316 (2009).

[31] Durbin, P. A., “Near-wall turbulence closure modeling without “damping functions””, en, Theoretical and Computational Fluid Dynamics vol. 3, no. 1, 1–13 (1991).

[32] Durbin, P., “Application of a near-wall turbulence model to boundary layers and heat transfer”, International Journal of Heat and Fluid Flow vol. 14, no. 4, 316–323 (1993).

[33] Durbin, P. A., “Separated flow computations with the $k-\epsilon-\overline{v^2}$ model”, AIAA Journal vol. 33, no. 4, 659–664 (1995).

[34] Parneix, S., Durbin, P., and Behnia, M., “Computation of 3-D Turbulent Boundary Layers Using the V2F Model”, en, Flow, Turbulence and Combustion vol. 60, no. 1, 19–46 (1998).

[35] Billard, F. and Laurence, D., “A robust $k-\epsilon-\overline{v^2}/k$ elliptic blending turbulence model applied to near-wall, separated and buoyant flows”, International Journal of Heat and Fluid Flow vol. 33, no. 1, 45–58 (2012).

Chapter 3

Summary of Papers

3.1 Paper I

Experiments were conducted studying the resonance region of vortex induced vibrations for a semi-blunt trailing edge hydrofoil in channel flow. The wake was studied by use of PIV. The structural vibrations were studied by embedded strain gauges located near the trailing edge tip as well as with a surface laser doppler velocimeter. Purely CFD simulations were carried out to investigate different RANS turbulence models capability to predict vortex shedding frequencies and wake velocity profiles for the geometry.

Overall, the expected behaviour was observed in the experiments, where the vortex shedding frequencies were found to lock on to the foils natural frequency for a significant range of channel bulk velocities. In addition, the wake velocity profiles were seen to vary significantly more during resonance, compared to off-resonance conditions. The different turbulence models utilized in the simulations predicted widely varying vortex shedding frequencies and wake velocity deficits. It was found that the differences in the vortex shedding frequencies could be largely attributed to differences in the predicted upper trailing edge boundary layer separation lines for the specific trailing edge tested.

3.2 Paper II

The paper presents additional CFD simulations for the same hydrofoil geometry as tested in **Paper I**, concerning the prediction of vortex shedding frequencies and hydrofoil wake velocity deficits. A comparison is made between the SST $k-\omega$ turbulence model and the v^2-f $k-\epsilon$ turbulence model, in addition to testing the impact of laminar to turbulent transition for the case. A sensitivity study with respect to inflow boundary conditions is also presented.

The case was found to be relatively insensitive to the inflow conditions with respect to turbulence levels and upstream pipe velocity profiles. Further, laminar to turbulent transition modeling gave essentially the same results as for the fully turbulent case, due to transition predicted to naturally occur very close to the leading edge for the specific hydrofoil. Both turbulence models tested under-predicted the velocity deficit in the wake compared to measurements and tended to underestimate the vortex shedding frequency.

3.3 Paper III

Paper III focuses on the flow in the vaneless space of a high head model Francis turbine geometry, studied by means of PIV measurements. The measurements were carried out with the turbine running in steady state conditions, for a fixed head and rotational speed. Several guide-vane openings was tested. For each guide-vane opening the time-average and transient wake characteristics are discussed, together with the periodic oscillations caused by the rotor-blade passing, otherwise known as the rotor-stator interaction (RSI).

It was found that in the wake of the guide-vane the dynamic energy content of the transverse velocity fluctuations from the trailing edge vortex shedding and RSI were of comparable sizes, though the energy from the vortex shedding is spread over a wider frequency range. While the measurements provide some insight, it is suggested that further measurements or numerical analysis is conducted in order to fully understand the impact of each effect.

3.4 Paper IV

Measurements were conducted studying the effect that two different trailing edge designs had on the vortex induced vibrations. The hydrofoil utilised had an identical profile to the one studied in **Paper I**, but was made with exchangeable trailing edges, which allowed a direct comparison of strain intensity levels as measured with embedded strain gauges. The two designs tested were sub-boundary layer vortex generators and rounded serrations cut into the body of the hydrofoil, both of which introduce a certain amount of stream-wise vorticity into the wake of the foil. The time-averaged and turbulent properties of the wake was measured through PIV.

Most notably, it was found that the vortex generators significantly reduced the vortex induced vibrations at resonance conditions, though at the cost of increased pressure loss associated with the geometry, compared to both the reference trailing edge as well as the serrated trailing edge. The serrations shifted the resonance range to higher flow velocities, but underwent larger vibrations once resonance occurred.

Chapter 4

Discussion

The following chapter discusses some of the main findings from the collection of papers as a whole. The findings are discussed in more detail in the individual works.

As a lead up to the trailing edge modifications presented in **Paper IV**, **Paper I** first focuses on the VIV resonant behaviour of an unmodified, generic hydrofoil serving as the reference case. Overall, the expected behaviour was found. The combination of PIV measurements in the wake and simultaneous measurements of the trailing edge strain clearly show, in figure Figure I.4, the large increase in the amplitude of the vibrations going through resonance, and the lock-on of the vortex shedding to the natural frequency of the foil for an extended velocity range. Together with previous measurements by Bergan et. al.[1] which focused on the the added damping effect from the water going through resonance, the set of data provide a substantial data-set for FSI simulations of the same case.

The eddy-viscosity turbulence models tested in the study demonstrated a significant spread in between the different models as well as a discrepancy between the simulated and measured flows, as shown here in figure Figure 4.1, reprinted from **Paper I** for convenience. This is somewhat expected, since flows over curved surfaces and gradual separation is precisely where such models tend to fail[2]. One hybrid RANS-LES model was also tested, namely the SAS approach based on the SST $k-\omega$ turbulence model. The shedding frequencies predicted are essentially the same as for the simulations with a purely RANS based approach with the same turbulence model. Since the same model still controls

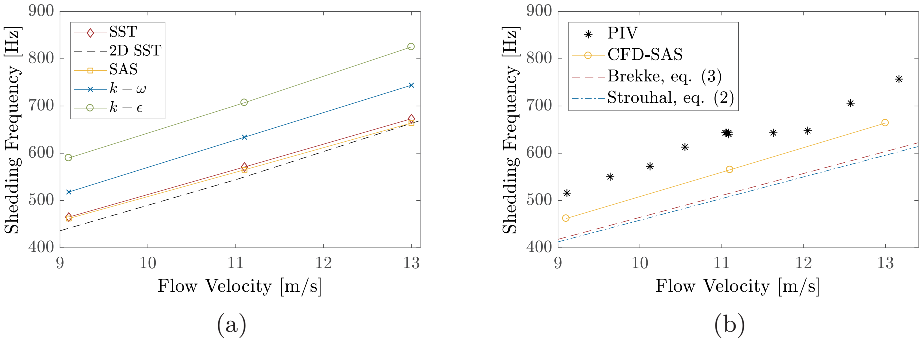

Figure 4.1: Shedding frequency versus flow velocity. (a) Effect of different turbulence models. (b) Experimental, CFD and empirical estimates. Figure from **Paper I**.

the development and separation of the boundary layer, this also underlines precisely why the turbulence model utilized in the boundary layer is so important for the case. One curious result was the significant deviation of the velocity profile in the wake compared to measurements and all the other models. It is postulated that the discrepancy in the predicted mean wake as simulated by the SAS model and the measurements is due to the transition region, where the model is gradually developing from a RANS to a LES treatment of the flow in the separated boundary layer. This "development region" is a known weakness for such hybrid RANS-LES, or DES, models, for certain spatial grids[3].

Overall, the numerical results presented in **Paper I** partly motivated the study presented in **Paper II**. The $k - \epsilon\ v^2 - f$ improved upon the predicted vortex shedding frequencies, compared to the SST $k - \omega$ turbulence model. However, as stated, without measurements of the trailing edge boundary layer it is not really feasible to accurately assess where the models have their weaknesses. As noted in the **Paper I**, there remained some uncertainties related to the slight surface roughness of the hydrofoil in the first set of measurements, as well as uncertainties related to the channel flow conditions, such as the mean velocity profiles and turbulence. The measurements presented in **Paper IV** for a fully smooth geometry essentially confirmed the previous results, and also confirmed that the inflow conditions set in the simulations with respect to turbulent parameters and pipe velocity profiles were reasonably matched with the experimental conditions.

The main results concerning the VIV for the different trailing edge designs further described in **Paper IV**, are reprinted here for convenience in figure 4.2. The VGs tested lead to a decrease of roughly 80% in the maximum peak of the strain intensity amplitudes, SI, compared to the reference. This decrease is in accordance with the overall decrease in the transverse velocity fluctuations across the hydrofoil wake, that can be seen in figure Figure IV.8. It is thought that the mechanism behind the reduction of vibration amplitudes at resonance is the effective de-correlation of the otherwise two-dimensional vortex shedding street and thus dampening of the pressure fluctuations at the trailing edge. Further analysis is needed to confirm this however. Notably these findings agree with similar measurements carried out for cylinders fitted with VGs[4].

The particular design of serrations tested are seen to lead to a shift in the resonant region towards higher velocities. The increased vibrational amplitudes are partly explained by the increased kinetic energy associated with the higher channel velocities, and partly by the change in the mechanical properties of the edge made by cutting into it. This last effect is made clear when comparing the peak to peak amplitudes occurring for the edge under forced vibrations in stationary water. Further, the power of vertical velocity fluctuations are seen to increase overall for this design. It is likely that this flow condition may be improved upon with slight changes of the serration parameters. For instance, serrations for flat trailing edges are known to be most beneficial with respect to sound reduction in certain frequency ranges when the amplitude of the serrations are twice the thickness of the boundary layer or larger[5]. While the current design is estimated to be within this criteria based on CFD results

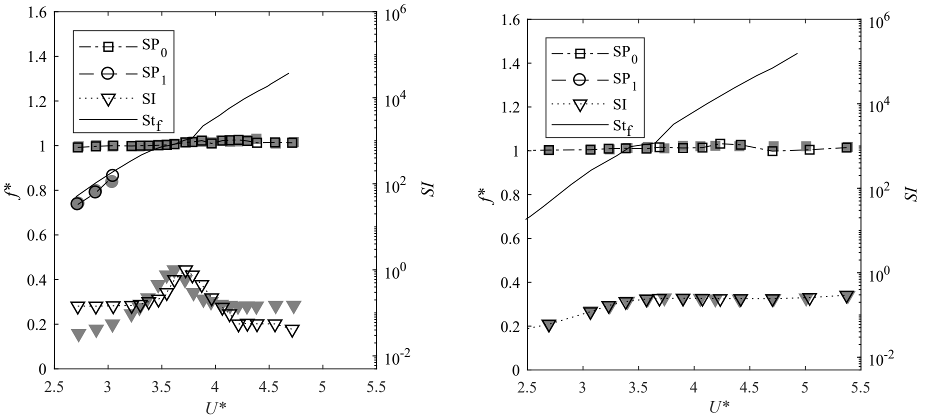

(Reference) (VG's)

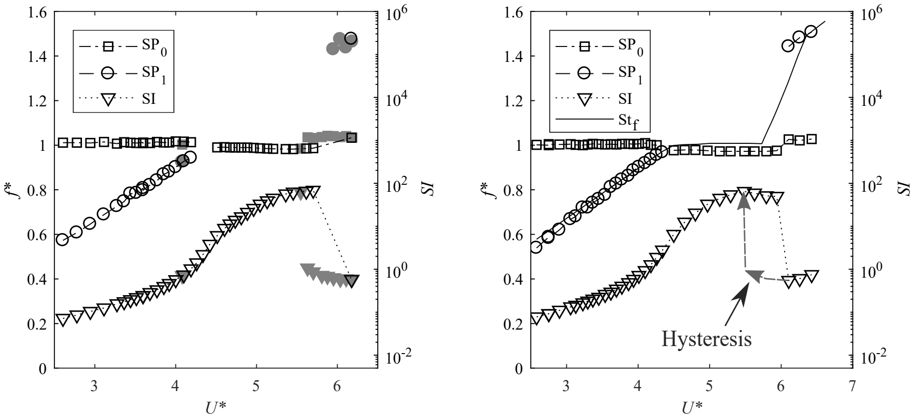

(Serrations - Set 1) (Serrations - Set 2)

Figure 4.2: Normalized vortex shedding frequencies and main strain frequencies plotted along the left vertical axis vs normalized bulk velocity, U^*, for all trailing edges tested. Note that strain intensity, SI, is plotted along the right secondary axis on a log-scale. Grey filled markers represent measurements made with a decreasing flow rate (ramp-down) as opposed to increasing flow rate (ramp-up) for the open markers. Figure from **Paper IV**.

from **Paper II**, it may well be that in order to achieve an appropriate scaling adjustments should be made for the fact it is a semi-blunt, rather than a thin, or flat edge. One interesting, but more subtle effect on the vibrations observed in the measurements with the serrated trailing edge was the presence of resonance induced cavitation, localized at the trailing edge for test section bulk velocities corresponding to $5 < U^* < 6$. The cavitation occured for the very largest amplitudes of vibrations and possibly augmented the hysteresis effect marked in the plot of figure 4.2, (Serrations - Set 2). Outside of resonance, even at higher velocities, the flow remained cavitation free. The limitations in the pressure rating of the test section and connected pipes meant that this effect could not be entirely avoided, though it does not significantly affect the results overall.

A trailing edge that performs as well as the VG's with respect to mitigating the effects of VIV, but without the inherently increased pressure losses documented in **Paper IV** along with the risk of failure due to erosion, would prove a viable candidate for the inclusion in hydraulic turbo-machines. This ties in with the discussion in **Paper III**, which focused on the flow in the vaneless space of a model Francis turbine. While VIVs are considered to be less of an issue for guide-vanes in Francis turbines in general[6], issues have been documented from stay-vanes and could potentially affect runner-blades. In closing, is notated that as indicated by the measurements in **Paper III**, figure III.6-III.7, vortex shedding from the guide-vanes is most likely to interfere with the runner blades only at guide vane openings for high loads, due to the trajectory of the wakes. It is feasible that the vortex shedding could trigger leading edge boundary layer instabilities in the runner, leading to "secondary" vibrations. Providing a passive flow control method by the introduction of stream-wise vortexes could mitigate such effects, though that is a topic for future studies.

References

[1] Bergan, C. W., Tengs, E. O., Solemslie, B. W., and Dahlhaug, O. G., "An experimental investigation of the hydrodynamic damping of vibrating hydrofoils", IOP Conference Series: Earth and Environmental Science vol. 240, 062008 (2019).

[2] Celic, A. and Hirschel, E. H., "Comparison of Eddy-Viscosity Turbulence Models in Flows with Adverse Pressure Gradient", en, AIAA Journal vol. 44, no. 10, 2156–2169 (2006).

[3] Spalart, P. R., "Detached-Eddy Simulation", Annual Review of Fluid Mechanics vol. 41, no. 1, 181–202 (2009).

[4] Tao, S.-b., Tang, A.-p., Xin, D.-b., Liu, K.-t., and Zhang, H.-f., "Vortex-induced vibration suppression of a circular cylinder with vortex generators", Shock and Vibration, 10.1155/2016/5298687 (2016).

[5] Gruber, M., Joseph, P., and Chong, T., “On the mechanisms of serrated airfoil trailing edge noise reduction”, in *17th AIAA/CEAS Aeroacoustics Conference (32nd AIAA Aeroacoustics Conference)*, Aeroacoustics Conferences (American Institute of Aeronautics and Astronautics, June 2011).

[6] Østby, P. T. K., Myrvold, E., Billdal, J. T., and Haugen, B., “Excitation of torsional modes in guide vanes”, IOP Conference Series: Earth and Environmental Science vol. 240, 062010 (2019).

Chapter 5

Conclusion and Further Work

In the following sections some concluding remarks on the individual works contained in the thesis are made as well as some suggestions for further work to be considered.

5.1 Conclusion

The numerical studies contained in **Paper I** and **Paper II** shows that even such a relatively simple geometry as the hydrofoil utilized in the present study provide a challenging case for eddy-viscosity turbulence models due to smooth curvature and gradual boundary layer separation occurring at the trailing edge. Overall the result is in accordance with existing findings in the literature, but serves as a reminder to the industry of the importance of a case to case validation, since the trailing edge geometry was specifically designed to be relevant for hydraulic turbines.

The measurement in **Paper IV** demonstrates that stream-wise vortices introduced by means of sub-boundary layer vortex generators can lead to a substantial reduction of VIVs, even at resonance. In opposition, the design of the trailing edge serrations tested here lead to increased vibrations at resonance, but introduces streamwise vorticity into the flow with no noticable increase in pressure losses. Seen in conjunction, the measurements suggests further improvements can be made towards the mitigation of VIVs, with designs relevant for use in hydraulic machinery, as well as other engineering disciplines where VIVs occur.

The initial velocity field measurements of the vane-less space in the high-head Francis turbine presented in **Paper III** provide some insight into the role of trailing edge modifications with respect to the rotor-stator interaction and potential triggering of boundary layer instabilities at the runner blade, but is largely inconclusive.

Overall is hoped that the PIV measurements and simulations may aid further numerical investigations, in particular with respect to fluid-structure interaction and further work towards mitigation of VIVs trough passive flow control geometries.

5.2 Further Work

Since optimizations of the flow control geometries introduced in this work were considered to be well outside the scope of the project, the goal was instead to obtain measurements for relevant flow geometries that could be further developed and studied numerically. As such, a numerical parameter study for the flow control concepts introduced, namely trailing edge fitted vortex generators and non-flat serrations, are considered a natural progression of the work. In addition the velocity measurements obtained in the vaneless space of the Francis turbine should support further numerical investigations of the relevance of such passive flow control methods as described above, for the use in turbines.

Part Two - Papers

Paper I

PIV measurements and CFD simulations of a hydrofoil at lock-in

K. F. Sagmo[1], E. O. Tengs[2], C. W. Bergan[1] and P.-T. Storli[1]

Published in *IOP Conference Series: Earth and Environmental Science*, March 2019, volume 240, issue 6, DOI: 10.1088/1755-1315/240/6/062006.

Abstract

As part of an ongoing investigation into the mitigation of vortex induced vibrations of hydrofoils, a combined experimental and numerical study of the fluid-structure interactions and wake of a hydrofoil at lock-in has been conducted at the Waterpower laboratory of the Norwegian University of Science and Technology. The hydrofoil has a blunt trailing edge and von Kármán vortex shedding induces a lock-in effect at a chord based Reynolds number of about $2{,}7{\cdot}10^6$. The present paper presents the initial measurements of vortex shedding frequencies going through lock-in, along with CFD simulations at lock-off conditions as well as some empirical estimates of vortex shedding. Experimentally the hydrofoil wake was studied in detail using particle image velocimetry (PIV). Hydrofoil vibration frequencies were measured by both a strain gauge positioned near the trailing edge of the foil as well as by a laser doppler vibrometer (LD-V). Numerically the phenomena was simulated using ANSYS CFX. Several different turbulence models was tested, from the two-equation standard $k - \epsilon$ model to the scale adaptive SST-SAS model, with considerably different results. It is observed that the vibrations induced at lock-in considerably shifts and reduces the hydrofoil wake velocity deficit. Further, the CFD results suggest that the driving parameter influencing the shedding frequency is the cross flow separation distance at the trailing edge.

I.1 Introduction

In order to avoid unnecessary fatigue and risk of failure when designing hydraulic turbines, it is an established guideline that the shedding frequency of guide vanes, stay vanes, and runner blades should not overlap with the natural frequencies of the blades in the range of operation [1]. According to Blake et al. [2], the recognition of the link between the trailing edge geometry and vortex shedding

---

[1] Waterpower Laboratory, Norwegian University of Science and Technology, Alfred Getz Vei 4, 7491 Trondheim, Norway.

[2] EDR & Medeso AS, Leif Tronstads Plass 4, 1337 Sandvika, Norway

became widespread in the 1960's. However, as has been indicated by several researchers, the task of predicting the shedding frequency from a blunt trailing edge strut or hydrofoil can be difficult due to it being highly sensitive to both tip geometry as well the surrounding flow conditions affecting the boundary layers [3]. Nevertheless, for trailing edges with sharp edges and clearly defined separation points modern CFD methods have proven effective [4]. In modern installments of hydraulic turbines limits are constantly being pushed with respect to increasing the performance of components, while at the same time reducing material- and manufacturing costs. Accurate prediction of component behavior becomes more important because safety and expected lifespan must be kept at acceptable levels. For components which objective is to transfer forces to or from fluids, this continuous process might push the components into designs where the structure and fluid are mutually changing the behavior of each other. This is when prediction of the behavior of the dynamics of the system becomes more involved [5]. In an effort to shed more light on the topic at hand, a combined numerical and experimental investigation is underway at the Norwegian University of Science and Technology (NTNU) for a hydrofoil under lock-in conditions. We present here some initial results.

I.2 Methods

I.2.1 Experimental Setup

I.2.1.1 PIV and frequency measurements setup

The general layout of the experimental setup is illustrated in figure I.1 a) and b). All measurements were done with the hydrofoil centerline angled parallel to the incoming flow field, i.e. 0 degrees angle of attack. The test section volumetric flow rate was measured by an ABB electromagnetic flow-meter located downstream of the test section. The maximum standard deviation in the mean flow during measurements was approximately 0.11 %, while the average temperature was 20.5±1.5 Celsius, giving an approximate chord based Reynolds number uncertainty of 3.65 %.

The hydrofoil vibration frequencies and amplitudes were measured with a strain-gauge located near the trailing edge at approximately mid-span, as well as with a surface laser doppler vibrometer (LD-V) pointing at the trailing edge. Data acquisition was managed with National Instruments (NI) LabVIEW and NI data acquisition devices (DAQ's). Sensor output voltages were sampled at 10 kHz, giving more than 10 samples per period for the frequencies investigated. For a more detailed explanation of the hydrofoil instrumentation, material properties and natural frequencies see Bergan et. al [6]. The frequency amplitude spectra later presented were obtained by performing a P.D. Welch power spectrum analysis in MATLAB with a Hanning window. As a means of smoothing the amplitude spectra the sensor signal were split into varying lengths relative to the approximate shedding frequencies measured, with a 50 % segment overlap.

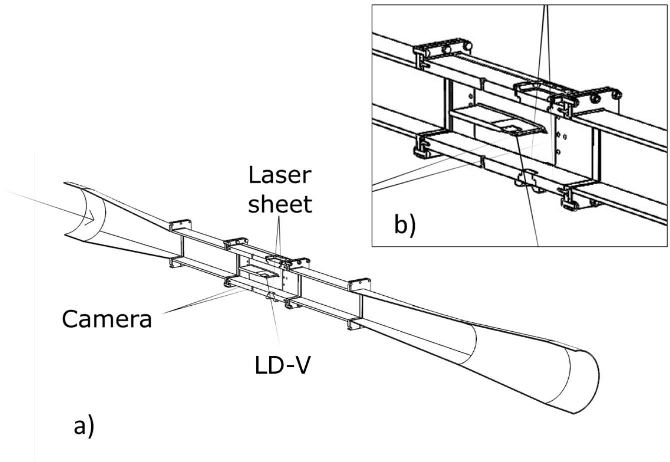

Figure I.1: Section view of the experimental test setup. b) gives an enlarged view of the rectangular test section and positioning of the hydrofoil.

The recording of the 2D PIV vector field in the wake of the hydrofoil was conducted with a high speed system provided by LaVision GmBH. Full resolution images of (1284 x 1024) pixels (px) were recorded in double frame mode at a sampling rate 2.4 kHz, with the camera oriented perpendicular to the illumination plane. The image sampling duration for each recorded image set was about 2 s. Table I.1 gives a summary of the recording parameters. The recording parameters were balanced such that the average image size of a tracer particle was about 2.4 px and the estimated particle displacement between each frame was about 5-6 px. Vector fields were evaluated using a multipass method, stepping from a 96 px x 96 px interrogation area (IA) with a 50 % overlap to a 64 px x 64 px IA with a 75 % overlap. This gave an average number of illuminated particle image pairs within each area of roughly 10. According to the synthetic PIV image generation evaluation described by Raffel et. al [7] these are image parameters that should give relatively low root mean square (RMS) random errors in the cross correlation evaluation of the vector fields. The degree of peak locking was investigated and found to be acceptably low. The image scaling calibration RMS error of the 3'rd order polynomial fit was about 0.38 px for the reported measurements.

To compute the uncertainty, $\triangle U$ in the time-averaged stream wise velocity U distributions later presented, the following estimate was applied [8];

$$\triangle U = \frac{\sigma_U}{\sqrt{N_{eff}}}, \tag{I.1}$$

where σ_U denotes the standard deviation in U across all samples during a measurement series and $\sqrt{N_{eff}}$ is the effective number of independent samples of U. $\sqrt{N_{eff}}$ involves the computation of the auto-correlation of the time-series of the instantaneous stream wise velocity vectors, $\vec{u}(x, y, t)$, and approaches

Table I.1: PIV recording parameters for the hydrofoil wake flow measurements

Field of view (FOV) / Area of interest	21.1 mm x 16.9 mm / 1280 px x 1024 px (x-y)
Interrogation volume / Interrogation area	1.06 mm x 1.06 mm x 0.5 mm / 64 px x 64 px (x-y)
Experimental velocity range	(8 - 14) m/s
Observation distance & Lens F-number	215 mm & 5.4
Recording method & Camera sensor	Double frame/Double exposure & CMOS
Exposure time & image acquisition rate	250 μs & 2.4 kHz
Image processing mode	cross-correlation
Mean tracer particle diameter d_p	13 μm
Tracer particle density δ_p	1.1 g/cm^3
Illumination source	Nd:YFL dual cavity laser, 527 nm wavelength

the total number of samples N in a signal in the case that the samples of $\vec{u}$ are completely independent. Finally, the error in U due to uncertainty in the the laser-plane span-wise position was investigated by measuring the hydrofoil wake at a parallel 10 mm offset plane. While the test clearly indicated 3D effects coming from the test section channel walls, the relative uncertainty in the positioning of the laser plane on the scale of 0.5 mm should have negligible impact on the time-averaged wake velocity distributions.

I.2.1.2 Hydrofoil Profile Geometry and Surface Roughness

To facilitate comparison with CFD simulations the hydrofoil surface roughness was measured with a profilometer at different chord-wise positions, giving a maximum arithmetic roughness average R_a of about 5.8 μm near the leading edge. Following Schlichting & Gersten [9], we approximate the technical roughness height by $k_{tech} = 3.5R_a$. For a maximum chord based Reynolds number of approximately $Re_C = 4.5 \cdot 10^6$ this gives for a fully turbulent boundary layer an estimated k^+ value of approximately 11. Hence we assume that the surface roughness height exceeds the viscous sub-layer near the leading edge and may play an important effect in the development of the boundary layer.

Figure I.2 shows the blade geometry. The hydrofoil surface position data was measured with a Leitz PMM-C 600 coordinate machine, capable of a repeatability range of less than 0.6 μm. These measurements were performed after the foil had been coated with a thin layer of matte black paint, to avoid unnecessary laser reflections in the PIV measurements. Figure I.2(b) shows the measured trailing edge along with the numerical grid points along the blade used in the CFD simulations. A noticeable difference is only visible at the steepest part of the trailing edge, where the flow is assumed to be separated. Hence any considerable differences in between the results from the measurements and the simulations are assumed not to stem from differences in the profile geometry.

I.2.2 Numerical Setup

A numerical study was performed to investigate how well the shedding phenomena is predicted in the lock-off region. The numerical simulations was purely Computational Fluid Dynamics (CFD), i.e. no structural response. The

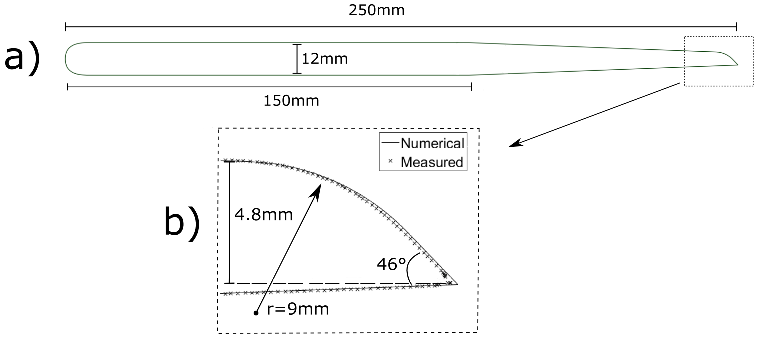

Figure I.2: a) Blade geometry. b) Measured trailing edge geometry plotted along the numerical grid wall cells.

simulations was performed in ANSYS CFX. The numerical domain and computational grid is illustrated in figure I.3. The channel extends $>> 10D_h$ upstream of the blade to ensure that the flow entering the test section is fully developed [10]. The domain was also extended downstream to minimize the risk of back-flow and outlet conditions affecting the blade vortex dynamics. The inlet boundary condition was static pressure, and the outlet condition was a mass flow corresponding to the different flow velocities. The turbulence intensity at the inlet was tested in the range $TI \in [0\% - 10\%]$, with no noticeable difference in the turbulence levels in the test section.

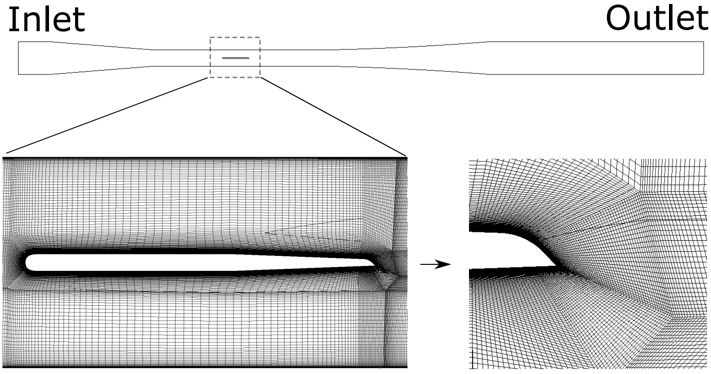

Figure I.3: Numerical flow domain and mesh around blade

The mesh was created in ANSYS ICEM CFD, and contained about 13 million, all hexahedral elements. When refining the mesh, it was observed that the coarser mesh simulations under-predicted the shedding frequency. On the final mesh, for a typical flow velocity tested in this article, U_{ref}=11 m/s, the maximal y^+ value was 1 and ≤ 0.5 at the leading and trailing edge, respectively. As an implicit numerical solver was used the time-step was chosen to be 8e-5 s, giving a corresponding Courant number of 3. Shedding frequencies in the order of $f = 500$ Hz were expected, and the time-step used corresponded to about 25 points per period. For the Reynolds Averaged Navier-Stokes based simulations several different turbulence models have been tested in order to investigate the effects on the predicted shedding dynamics. The standard $k - \epsilon$ model [11, 12], was expected in this case likely to struggle to give an accurate result, due to the known problems with separation and streamline curvature. Another two-equation model, the Wilcox $k - \omega$ model [13, 14], was also tested, along with the $k - \omega$ SST [15], a combination of the two. Additionally, the scale-adaptive SAS-SST model [16] was tested. Given an adequate computational grid the SAS model resolves the larger turbulent structures, at increased computational costs. Further, 2-dimensional simulations was performed on a simplified, shortened test section to investigate means of speeding up the simulations.

I.2.3 Empirical estimates for vortex shedding

It may be interesting to compare the measured and CFD predicted shedding frequencies with some empirical estimates. The first empirical approach utilized in the present study is the traditional Strouhal shedding frequency [17], f_s, here defined as

$$f_s = \frac{St \cdot U_\infty}{D}, \tag{I.2}$$

where D in this case is approximated as the blade thickness at the trailing edge, St denotes the Strouhal number and U_∞ is the free stream velocity. For the chord based Reynolds number range encountered in this study, the Strouhal number was chosen to be $St = 0.22$, a commonly used value [18]. The thickness of the trailing edge, $D = 4.8$ mm, is measured at the point where the curved surface starts, see figure I.2(b).

An empirical formula more specific for the Francis turbine and different trailing edge geometries is described in the paper by Brekke [1], where the frequency of the vortex shedding is approximated by:

$$f_s = 190 \frac{B}{100} \frac{U_\infty}{(t + 0.56)} \tag{I.3}$$

Here B is a constant linked to the trailing edge geometry, U_∞ is the free stream velocity, and t is the blade thickness in [mm]. The constant $B = 131$ is chosen from [1], and is related to a trailing edge geometry very close to the one tested here. Note however that in Brekke's considerations, all blade geometries had parallel upper and lower surfaces. This is not the case for the blade geometry in this study which has tapered surfaces toward the trailing edge. Hence, strictly $t \neq D$. Nevertheless equation I.3 is used here in its current form.

I.2.4 Wall effects

The hydrofoil tested in this study has a front section area to test section area blockage ratio of 8 %, and requires a correction for the measured Strouhal number, St_{meas}, due to added wall effects[19, 20]. Following the considerations of Ota et al. [20] for incompressible flow over a 2D-geometry experimental setup, we estimate the correction factor, ε, by the following relation for the free stream Strouhal number St,

$$St = St_{meas}(1 - \varepsilon\frac{t}{h}). \tag{I.4}$$

Here t denotes the height of the hydrofoil (12mm) and h the height of the measuring section (150mm), giving $t/h = 8\%$. The observed correction factor ε is here estimated by the assumed free stream Strouhal number of 0.22, and the measured Strouhal number outside the range of lock-in. Note that for the rough empirical estimates for the shedding frequencies later presented the free stream velocity is approximated as the average velocity across the undisturbed test section, such that $U_\infty = U_{ref}$, since, to the authors knowledge there is no reliable way to estimate the correction factor a-priori for the geometry tested in this study.

I.3 Results

Experimental results

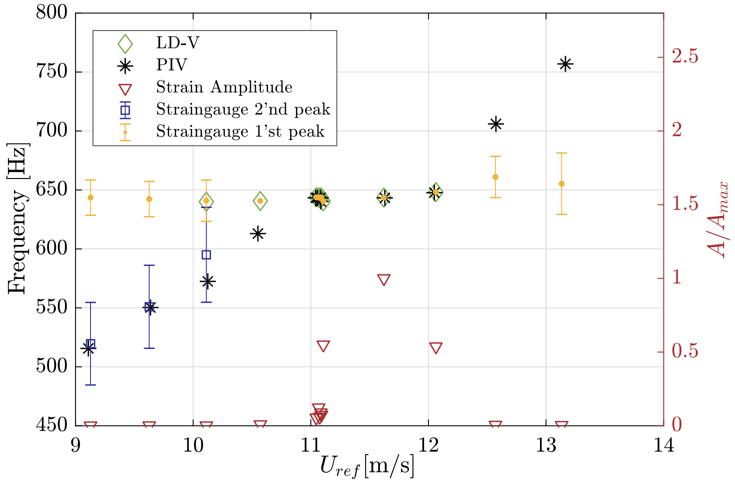

Figure I.4: Hydrofoil vibration frequencies and shedding frequencies measured by PIV, strain-gauges and LD-Vibrometer. The relative hydrofoil vibrational amplitude is plotted along the right y-axis.

Figure I.4 presents the hydrofoil vibration frequencies and shedding frequencies measured by PIV, strain-gauge and LD-Vibrometer. There is a precise agreement between the measuring techniques in lock-in, with resonance starting to occur at around 11.1 m/s as indicated by the sharp rise in the vibrational amplitude. The first, standing peak found in the strain-gauge frequency amplitude spectrum, presented for some velocities outside lock-in in figure I.5, is identified as the hydrofoil natural frequency [6]. The second, broad ranged traveling peak found in the frequency spectrum in the strain measurements can be identified as the shedding frequencies in lock-off conditions, as indicated by the agreement with PIV measurements in the wake. Since the shedding frequency is assumed to be inherently gaussian about it's mean value, the size of the error bars given in figure I.4 in the strain-gauge 2'nd peak was estimated by the half width at half maximum (HWHM) for the smoothed frequency distribution curves given in figure I.5. In lock-in, the uncertainty in the hydrofoil vibrational frequency was estimated by the standard deviation in peak frequency from repeated measurements at 11.1 m/s and found to be approximately 1.6 Hz.

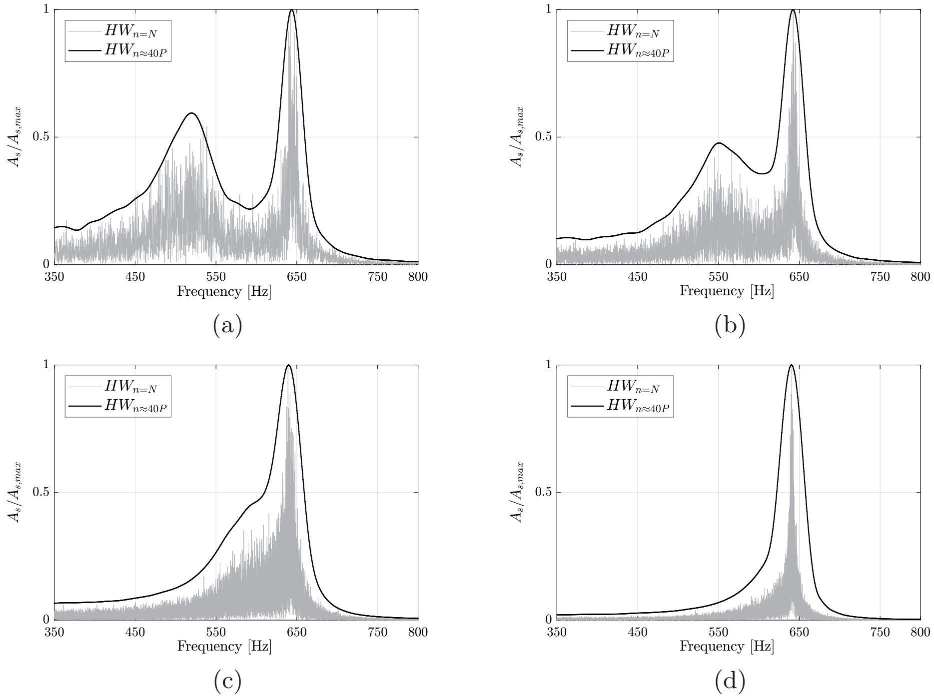

(a)

(b)

(c)

(d)

Figure I.5: Amplitude frequency spectra for increasing reference velocities from strain-gauge voltage signal, showing the traveling shedding frequency peak (left peak) approaching the natural (standing) frequency peak of the hydrofoil. (a) $U_{ref} = 9.1$ m/s. (b) $U_{ref} = 9.6$ m/s. (c) $U_{ref} = 10.1$ m/s. (d) $U_{ref} = 10.6$ m/s.

The average observed Strouhal number, as found from frequency estimates by the PIV measurements given in figure I.4 for reference velocities between 9.1 m/s and 10.6 m/s, is 0.274, with a standard deviation of about 1.3 %. The ratio between the assumed and the measured Strouhal frequency is ≈0.794, and from equation I.4 this gives an average correction factor $\epsilon \approx 2.57$.

Figure I.6 gives the normalised time-averaged streamwise velocity distribution in the hydrofoil wake measured by PIV at two downstream positions $x_1 = 9.9D$ and $x_2 = 13.3D$, measured from the trailing edge tip. Sets of varying reference velocities are included, both for lock-off (I.6(a)-(b)) and lock-in conditions (I.6(c)-(d)). It is noted that the wake velocity distributions varies considerably more during lock-in.

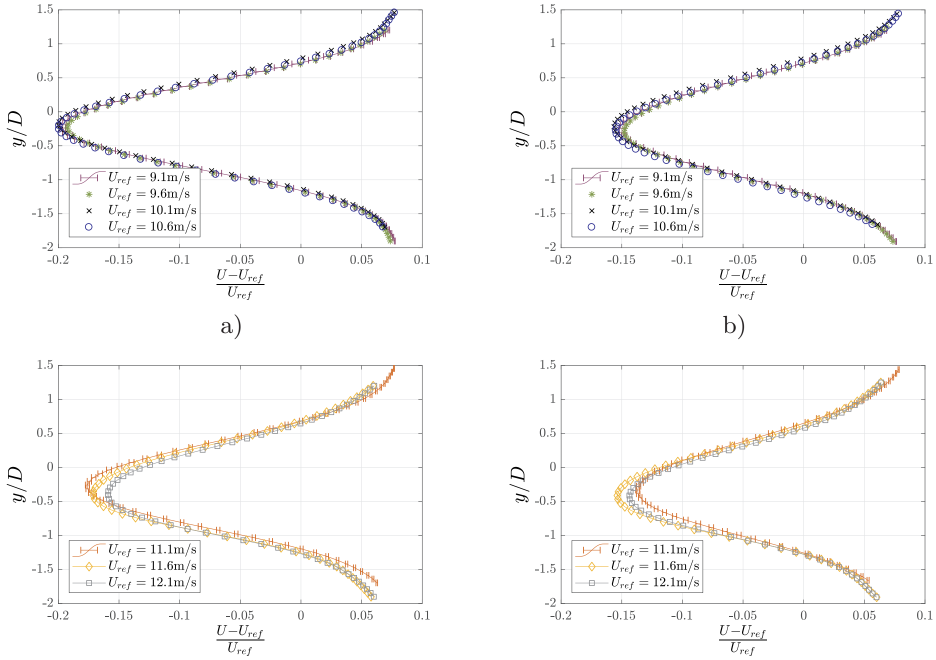

a)

b)

c)

d)

Figure I.6: Time-averaged PIV measured velocity distributions normalised with respect to the mean channel velocity for different downstream positions. Height normalised by trailing edge thickness, with $y = 0$ set at the hydrofoil center line. In (a) and (c) x = $9.9D$. In (b) and (d) x = $13.3D$. Uncertainty error bars are only plotted for reference velocities of 9.1 m/s and 11.1 m/s, for clarity.

Numerical results

Figure I.7 shows the stream-wise velocity at two vertical lines, $x_1 = 9.9D$ and $x_2 = 13.3D$, downstream of the blade at $U_{ref} = 9.1$ m/s. The velocities are time averaged over 2 s and ≈ 100 shedding periods in the experiment and simulations, respectively.

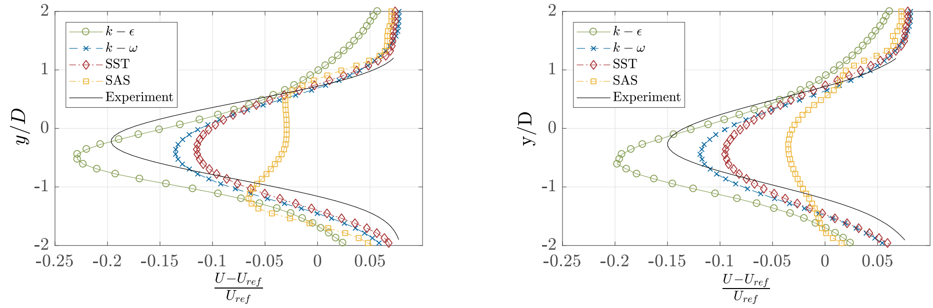

(a)

(b)

Figure I.7: Experimental and numerical comparison of the time-averaged velocity profile downstream of the trailing edge. (a) $x = 9.9D$. (b) $x = 13.3D$.

Next, the frequency of the shedding is compared in figure I.8(a). The uncertainty in the fast Fourier transform of the simulated time-signal is estimated to be $\xi \approx 5$ Hz. We observe that a linear trend is found for all turbulence models, as is reported by most sources e.g. [1, 17], and thus it is assumed that the general vortex shedding phenomena is captured. For ease of comparison figure I.8(b) shows the experimental and numerical results from the SAS simulations together, along with empirical estimates for vortex shedding. Finally, figure I.9 gives a comparison of the instantaneous velocity fields obtained with the different numerical schemes. The vertical black lines denotes one of the spatial locations of the PIV profile measurements ($x = 9.9D$)

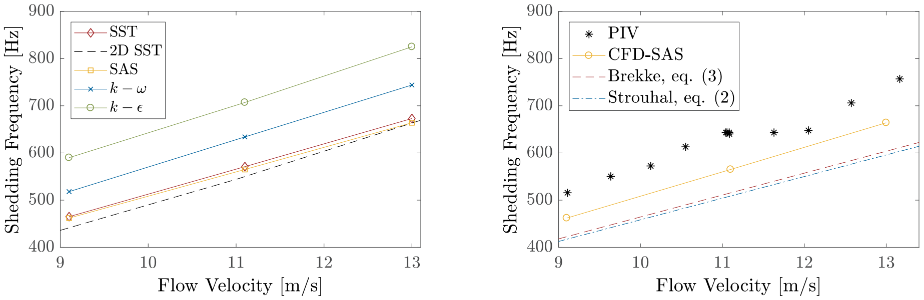

(a)

(b)

Figure I.8: Shedding frequency versus flow velocity. (a) Effect of different turbulence models. (b) Experimental, CFD and empirical estimates.

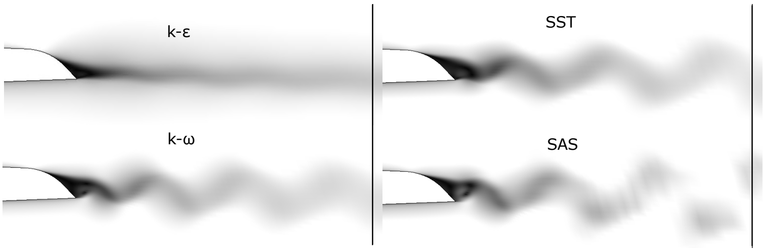

Figure I.9: Trailing edge wake comparison using different turbulence models, $U_{ref} = 9.1$ m/s. Coloring according to fluid velocity with $u = 0$ m/s being black and $u = 9.1$ m/s being white.

I.4 Discussion

From Heskestad and Olberts [3] we note that according to their measurements, 3 geometries all similar in design to the foil under investigation here, gave a relative standard deviation in the shedding frequency Strouhal number of about 12%. This indicates that the trailing edge shedding frequency is quite sensitive to small changes in the geometry. Hence the error in the rough empirical estimates (equation I.2 & equation I.3) for the shedding frequencies of about 20% and the wall correction factor estimated to $\epsilon = 2.46$ is assumed to contain both wall effects as well as boundary layer separation effects specific to the hydrofoil and trailing edge geometry tested here. The level of the error is sobering, and illustrates the need for either model measurements or accurate case dependent numerical tools in the design phase of hydraulic turbine blade components, even in lock-of conditions.

Comparing experimental and numerical results in figure I.7 we observe that the wake center is consistently shifted slightly below the hydrofoil center line, with about $0.2D$ in the experiments at lock-off conditions. It is believed that this is due to the asymmetry of the trailing edge, as the upper separation point is allowed to travel closer to the hydrofoil's centerline due to the relatively gentle curvature, effectively shifting the wake profile. In the simulations points of zero wall shear stress was investigated in order to study the separation points impact on the wake and shedding frequencies obtained. When different flow velocities are compared, the separation occurs later the higher the flow velocity. Correspondingly, the "perceived" thickness of the trailing edge is also thinner at higher speeds. When comparing the results from different turbulence models at a fixed reference velocity it was also found that a delayed separation point corresponded to an increase in the shedding frequency. This indicates that the differences in the turbulence models lie in the simulated boundary layer and subsequently the numerical prediction of the boundary layer separation points. As an example, comparing results in figure I.7-I.9, the $k - \epsilon$ model separated latest along the trailing edge, resulted in the highest shedding frequency and the most vertically shifted wake.

As an overall trend, the numerical simulations tended to underestimate the velocity deficit, except for the $k-\epsilon$ model, where the deficit was overestimated. The wake is considerably different depending on which turbulence model is used. From figure I.9 we can start to understand why the different velocity profiles in figure I.7 look like they do. In the SAS model, the wake breaks down into smaller vortexes, and thus the mean flow in the wake is higher and flatter. This corresponds to the lower velocity deficit in figure I.7. Similarly, it can seem like the $k-\epsilon$ model have the strongest velocity deficit and widest wake. It is also observed that the oscillations in the $k-\epsilon$ wake are very small. Compared to the PIV measurements, the SAS model performs qualitatively best (not shown), while interestingly, figure I.7 indicates that the mean velocity distribution is farthest from the experimental values for this model.

Figure I.8 (a) show the trends of the shedding frequency for different turbulence models. A linear best fit is performed and the slopes are used as comparison. The slope is varying with $\approx 22\%$, from $k-\epsilon$ to SAS. The SST and the SAS model perform very similarly. 2-dimensional simulations with the SST turbulence model is also included in figure I.8 (a). Clearly, they provide some predictive value while also providing a significant speedup factor, in this case, of $\approx 70\times$. When comparing the numerical and experimental results in figure I.8 (b), it is seen that there is a general under prediction of the shedding frequency by the numerical simulations. Based on the slope of the experimental results after a linear best fit the offset between the SST and SAS model compared to the experimental values are $< 4\%$, while the numerically observed Strouhal number is about 10 % lower than the comparatively obtained experimental Strouhal number of 0.274 in lock-off conditions. A closer investigation of the possible reasons for the relative offset between the CFD calculations and the experimentally obtained results are part of future work, along with simulations utilizing a fluid-structure interaction coupling for numerical investigation of the hydrofoil behaviour in lock-in.

I.5 Conclusion

The wake and shedding frequencies from a hydrofoil with a blunt, asymmetrical trailing edge has been investigated for free-stream velocities where turbulent von Kármán vortexes incites a lock-in effect. At lock-in we observe larger streamwise velocity fluctuations in the hydrofoil wake, than in lock-off conditions, likely due to wandering of the upper separation point at the trailing edge tip. Experimentally obtained shedding frequencies has been compared to numerical simulations as well as empirical estimates. The relative differences between simulations with different turbulence models clearly indicate the difficulties in the modelling of the separation points and subsequent wake characteristics crucial to estimating the risk of lock-in at the design phase for a hydraulic turbine blade component. The numerically obtained results for the trend in the shedding frequencies are in relative agreement with previous studies for similar trailing edge geometries [3], indicating that a delayed separation point leads to increased shedding frequencies.

Acknowledgements. Magne Tveit Bolstad is gratefully acknowledged for his assistance during measurements and help in design of the experimental setup. Thanks also to Prof. Knut Sørby for his assistance in measuring the hydrofoil surface roughness and geometry.

References

[1] Brekke, H., “A review on oscillatory problems in francis turbines and simulation of unsteady flow in conduit systems”, in Proceedings of the 17th iahr symposium, beijing, china (1994), pp. 15–19.

[2] Blake, W. K., “Excitation of Plates and Hydrofoils by Trailing Edge Flows”, Journal of Vibration Acoustics Stress and Reliability in Design vol. 106, no. 3, 351 (1984).

[3] Heskestad, G. and Olberts, D. R., “Influence of Trailing-Edge Geometry on Hydraulic-Turbine-Blade Vibration Resulting From Vortex Excitation”, Journal of Engineering for Power vol. 82, 103–09 (1960).

[4] Do, T., Chen, L., and Tu, J., “Numerical study of turbulent trailing-edge flows with base cavity effects using urans”, Journal of Fluids and Structures vol. 26, no. 7, 1155–1173 (2010).

[5] Liaghat, T., Guibault, F., Allenbach, L., and Nennemann, B., “Two-Way Fluid-Structure Coupling in Vibration and Damping Analysis of an Oscillating Hydrofoil”, ASME 2014 International Mechanical Engineering Congress and Exposition vol. 4A (2014).

[6] Bergan, C., Solemslie, B., Østby, P., and Dahlhaug, O. G., “Hydrodynamic damping of a fluttering hydrofoil in high-speed flows”, International Journal of Fluid Machinery and Systems vol. 11, no. 2, 146–153 (2018).

[7] Raffel, M., Willert, C. E., Wereley, S., and Kompenhans, J., *Particle image velocimetry: a practical guide*, edited by Raffel, M., 3’rd ed (Springer, Heidelberg ; New York, 2007).

[8] LaVision GmbH, *Lavision software davis 8.4 product-manual, item-number: 1105xxx*, Document name: 1003001 DaVis D84.pdf, Feb. 2017.

[9] Schlichting, H. and Gersten, K., *Boundary-layer theory*, 9th ed. (Springer-Verlag, Berlin Heidelberg, 2017).

[10] Cengel, Y. A. and Cimbala, J. M., *Fluid mechanics fundamentals and applications* (International Edition, McGraw Hill Publication, 2006).

[11] Launder, B. E. and Spalding, D. B., “The numerical computation of turbulent flows”, in *Numerical prediction of flow, heat transfer, turbulence and combustion* (Elsevier, 1983), pp. 96–116.

[12] ANSYS Inc, *Ansys 18.2 documentation, the k-epsilon model in ansys cfx* (2017).

[13] Wilcox, D. C., “Multiscale model for turbulent flows”, AIAA journal vol. 26, no. 11, 1311–1320 (1988).

[14] ANSYS Inc, *Ansys 18.2 documentation, the k-omega models in ansys cfx* (2017).

[15] Menter, F. R., “Two-equation eddy-viscosity turbulence models for engineering applications”, AIAA journal vol. 32, no. 8, 1598–1605 (1994).

[16] Menter, F. and Egorov, Y., “A scale adaptive simulation model using two-equation models”, in 43rd aiaa aerospace sciences meeting and exhibit (2005), p. 1095.

[17] Strouhal, V., “Uber eine besondere art der tonerregung”, Annalen der Physik vol. 241, no. 10, 216–251 (1878).

[18] Hartog, D. and Pieter, J., *Mechanical vibrations* (Courier Corporation, 1985).

[19] West, G. S. and Apelt, C. J., “The effects of tunnel blockage and aspect ratio on the mean flow past a circular cylinder with Reynolds numbers between 10^4 and 10^5”, Journal of Fluid Mechanics vol. 114, 361 (1982).

[20] Ota, T., Okamoto, Y., and Yoshikawa, H., “A Correction Formula for Wall Effects on Unsteady Forces of Two-Dimensional Bluff Bodies”, Journal of Fluids Engineering vol. 116, no. 3, 414–18 (1994).

Paper II

A test of the v^2-f k-ϵ turbulence model for the prediction of vortex shedding in the Francis-99 hydrofoil test case

K. F. Sagmo[1] **and P.-T. Storli**[1]

Published in *Journal of Physics: Conference Series*, August 2019, volume 1296, pp 012004, DOI: 10.1088/1742-6596/1296/1/012004.

Abstract

A test of the $v^2 - f\ k - \epsilon$ turbulence model for the flow around the Francis-99 hydrofoil geometry is conducted in order to assess it's accuracy of trailing edge vortex shedding prediction. The model is based on the $k - \epsilon$ turbulence model, but needs no wall damping function, and also allows near-wall turbulence anisotropy. For reference, the model results are compared with the the SST $k - \omega$, in addition to preliminary experimental results previously published. It is indicated that the $v^2 - f\ k - \epsilon$ model gives at least as good, or better results than the more commonly used SST $k - \omega$ model for the present case, though further measurements are needed in order to make a proper conclusion.

II.1 Introduction

One step towards an accurate fluid structure interaction (FSI) simulation is an accurate modeling of the computational fluid dynamics (CFD) domain. Typically, eddy resolving simulations are considered too expensive for an FSI simulation, so instead a Reynolds-averaged Navier-Stokes (RANS) approach with an accurate turbulence closure model is sought. For the present case in particular, accurate prediction of separation is important. The $v^2 - f\ k - \epsilon$ turbulence model has previously proven effective for such problems[1, 2]. The model allows for near wall turbulence anisotropy, by setting the appropriate boundary condition for the elliptic function f near a wall, ensuring that the velocity scalar $\overline{v^2}$ behaves like the wall normal Reynolds stress component as the wall normal distance goes to zero. The benefit of the model's ability to capture the suppression of the normal component of the turbulence near a wall relative to the tangential components eliminates the need to dampen the modeled eddy viscosity in this

---

[1] Waterpower Laboratory, Norwegian University of Science and Technology, Alfred Getz Vei 4, 7491 Trondheim, Norway.

region. This is demonstrated by excellent agreement of the model near wall eddy viscosity compared with DNS data for the eddy viscosity in channel flow[3].

II.2 Methods

II.2.1 Computational domain and boundary conditions

The numerical simulations were carried out on a trimmed, semi-regular hexahedral 3D grid, set up in accordance with the experimental geometry to allow for direct comparison of the results. No-slip conditions were specified at all walls, and y^+ values were kept below 1 in order to resolve the sub-viscous boundary layer and avoid the use of wall functions. A cross section view of the computational domain and grid, along with the position of the velocity inlet and the environmentally specified atmospheric pressure outlet is presented in figure II.1. Also defined is the foil trailing edge thickness $D = 4.8$ mm, and the foil chord length $c = 250$ mm. All simulations were carried out at a test section bulk velocity of 9.1 m/s, or a Reynolds number of about $2.3 \cdot 10^6$, matching the experimental conditions described by Sagmo et. al[4] and Bergan et. al[5]. The hydrofoil goes through vortex induced resonance at bulk velocities of around 11.6 m/s, which is deemed sufficiently far away for a purely computational fluid dynamics simulation to be accurate at the present test section inflow conditions.

In the experimental test rig, the straight circular pipe leading into the test section, seen in the top view of figure II.1, extends about 21 diameters upstream before encountering a 90 degree bend with stationary vanes. As such, the incoming pipe flow is assumed to be nearly fully developed, though measurements are needed in order to confirm this. During setup of the simulations several positions of the velocity inlet was tested with steady state RANS calculations, in order to check the sensitivity of the test section velocity profile as a function of the incoming pipe velocity profile. Figure II.2 give the results for three different inlet positions; A - at the beginning of the quadratic test section, B - the inlet position shown in figure II.1 and C - a further 6 m upstream of position B. It was found that a flow development length of about 20 diameters upstream of the convergent section lead to a slightly more developed test section velocity profile with a center line velocity increase of roughly 2 % (evaluated about $1.5c$ upstream of the hydrofoil) compared to a uniform velocity profile set at the start of the test section. The near fully developed pipe velocity profile extracted from inlet position C was therefore specified at the velocity inlet shown in figure II.1 for the simulations later presented. The location of the pressure outlet was also varied to ensure that the positioning had negligible impact on the simulation results.

A uniform turbulence intensity, TI of 5% was specified at the inlet, along with a turbulent length scale, L, of 1/6 times the pipe radius of 150 mm. The necessary model turbulence parameters, the turbulent kinetic energy k, the turbulent dissipation rate ϵ, the velocity scalar $\overline{v^2}$ and the specific dissipation rate ω, were then derived by the relations[6]:

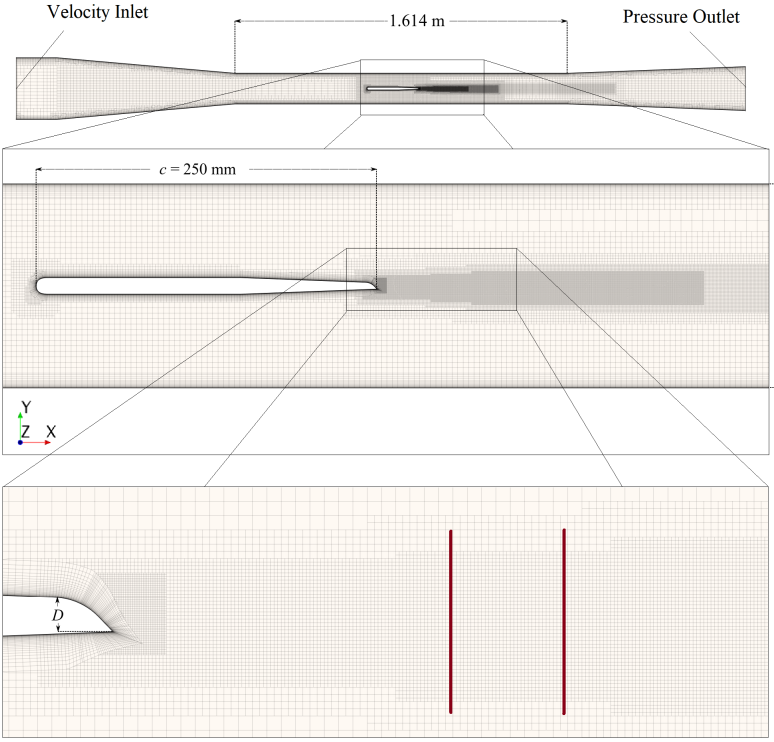

Figure II.1: Mid section of computational domain grid in successively enlarged views. The orientation of the coordinate system is also indicated. The two bold red vertical lines in the bottom enlargement from left to right indicates the velocity sampling positions at X=9.9D and X=13.3D downstream of the trailing edge tip, respectively.

$$k = \frac{3}{2}(TI|\mathbf{u}|)^2, \quad \epsilon = C_\mu \frac{k^{3/2}}{L}, \quad \overline{v^2} = \frac{2}{3}k, \quad \omega = \beta^{*-1/4}\frac{\sqrt{k}}{L}. \tag{II.1}$$

Above, $|\mathbf{u}|$ denotes the local velocity magnitude, and C_μ as well as β^* are model coefficients.

Unfortunately, experimental values for the turbulence intensity and turbulent length scale are not yet available for the test section. In order to give some indication of the sensitivity of the model results on the turbulence intensity, another set of simulations were conducted with a 20% inlet TI. To give some indication of the modeled decay of the turbulence table II.1 shows the specified turbulence intensities at the inlet, along with corresponding turbulence intensities both upstream of the hydrofoil and at the trailing edge, just outside the boundary layer.

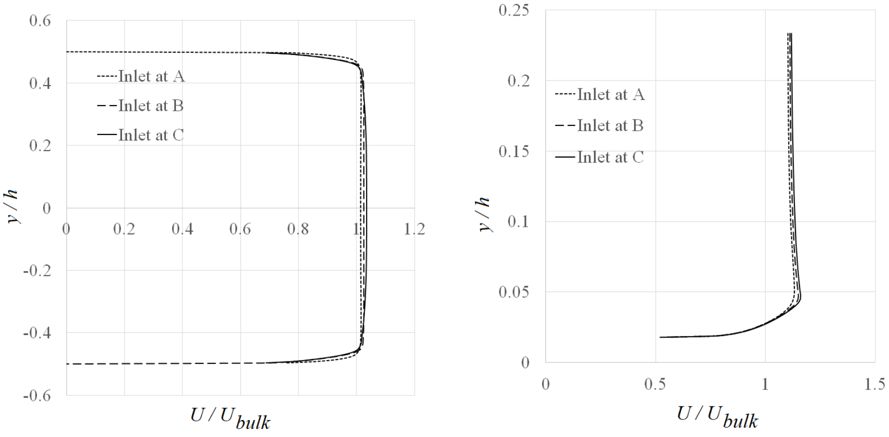

(a) (b)

Figure II.2: Effects of moving the velocity inlet upstream from position A to B and C. (a) Resulting test section velocity-profile approximately 1.5c upstream. (b) Resulting trailing edge velocity profiles at X=0.96c

Table II.1: Turbulence intensity levels (TI) at different stream-wise positions in the computational domain, relative to the hydrofoil leading edge (X=0).

Inlet	X=-1.5c	X=0.95c
5%	1.8%	1.2%
20%	4.7%	3%

II.2.2 Turbulence models and solvers

The present work focuses on the v^2-f k-ϵ turbulence model, with the model transport equations as described by Durbin[2] as well as Parneix et al.[7].

The second turbulence model utilised, for reference, is the widely used Shear Stress Transport (SST) k-ω turbulence model, presented by Menter[8]. In addition, in order to investigate the effect of laminar to turbulent transition on the case, the Langtry-Menter γ-Re$_\theta$ transition model[9] was run with the SST k-ω turbulence model. This model put the strictest constraints on the design of the mesh, such as limiting the wall cell layer thickness growth rate to 1.2, preferably 1.1, according to recommended practice[10]. This resulted in a wall cell layer growth rate of 1.15 over the hydrofoil surface. The γ-Re$_\theta$ transition model requires the definition of a free stream function. For simplicity, and from inspection of preliminary results with the steady state RANS simulations this function was specified as a step function going from zero to unity outside a 8 mm wall distance. The model coefficients as implemented in Star-CCM+ are described in the paper by Malan et al.[11]

All models were run with a segregated velocity-pressure correction solver, according to the SIMPLE algorithm. For comparability, the upwind flow convection scheme was set to second order, as was the solvers for the turbulence equations. All turbulence models constitutive relations were linear, i.e. according to the classic Boussinesq approximation. Further, a realizability constraint was set for both models, according to Durbin's scale limiter presented in [12].

II.2.3 Sampling periods and temporal discretization

The transient simulations were initiated from steady state solutions converged to normalized residuals of order 10^{-4} or less of all transported variables. For each successive time step, 6 inner iterations were run, which again ensured that all normalized residuals had reached values of order 10^{-4} or less. All simulations were run approximately 50 trailing edge vortex shedding periods before sampling of mean quantities were initiated and run for a successive 100 shedding periods.

An implicit temporal solver of 2'nd order was used and the time-step was set to $2.5 \cdot 10^{-5}$ s, such that the convective Courant number, C_n, achieved was around 1 in the wake of the trailing edge, and less than 2 for the vast majority of the computational domain. This further ensured around 80 time-steps per shedding period. For the coarse and fine grids used in the calculation of the grid discretization error the time-steps were adjusted in order to keep the C_n comparable for all 3 grids.

The trailing edge shedding frequency Strouhal number, St, was computed using Welch's method to obtain the power spectra of the cross stream velocity fluctuations sampled in the wake. The mean stream-wise velocity was sampled at positions indicated in figure II.1.

II.2.4 Discretization error estimation and iterative errors

The grid convergence index, GCI was calculated by the procedure recommended by Celik et. al.[13]. The simulations with the v^2-f k-ϵ turbulence model were run at 3 different grids, with a refinement rate of roughly 1.5 in between each grid. The results from the grid refinement study are presented in the next section.

Further, temporal iterative errors were investigated for all simulations by checking results at sampling periods corresponding to roughly 50 and 100 shedding periods, showing negligible differences compared to the differences in the solutions on the different grids.

II.3 Results

II.3.1 Grid discretization error estimates

Figure II.3 illustrates the grid dependency for both the velocity profile at $9.9D$ and the obtained Strouhal numbers for the present Reynolds number of $2.3 \cdot 10^6$. The cell count for each grid, going from coarse to fine were; $11.66 \cdot 10^6, 20.88 \cdot 10^6$ and $52.05 \cdot 10^6$. Results are for the v^2-f k-ϵ turbulence model. All results given below are with the medium grid, due to the computational expense of having

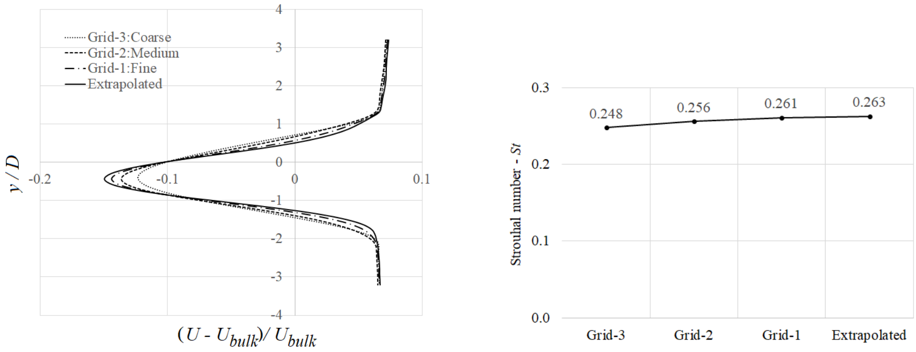

(a) (b)

Figure II.3: Solutions for different grids with the v^2-f model (a) Wake profiles for X=9.9D (b) Strouhal numbers based on bulk velocity and D.

to run all turbulence models on the fine grid, for comparison. From the wake profiles, an average observed numerical order, p_{obs}=1.9 was calculated. This was used to calculate the GCI plotted with the below results for the velocity profiles. From the obtained Strouhal numbers, a p_{obs}=2.7 was calculated, and subsequently used for the GCI plotted with the Strouhal numbers in figure II.5. Seen in conjunction, the calculated numerical orders are in good agreement with the selected 2'nd order numerical schemes.

II.3.2 Comparison of Models and Measurement

Figure II.4 presents the simulated wake profiles at the two locations indicated in figure II.1. Finally figure II.5 compares the obtained Strouhal numbers from all models.

II.4 Discussion and Conclusion

In figure II.4 a and b the small variation in the free stream TI close to the trailing edge of 3% compared to 1.2%, obtained from specifying a high turbulence inlet value of 20%, is seen to have negligible impact on the wake profile at both downstream positions. Still, it may well be that a larger TI variation, hitting some critical value could give substantially different results. In addition, transition from laminar to turbulent flow modeled with the γ-Re$_\theta$ formulation is seen to have little impact on the wake profiles. Though not shown, this is due to the model predicting transition quite close to the leading edge, at about X=0.03c.

Overall the v^2-f model again agrees somewhat better with experimental values than the other models. It is assumed that a slightly better prediction of the upper separation point is the root cause of this, though experiments are needed to confirm this. It is noted a small variation in the free stream turbulence

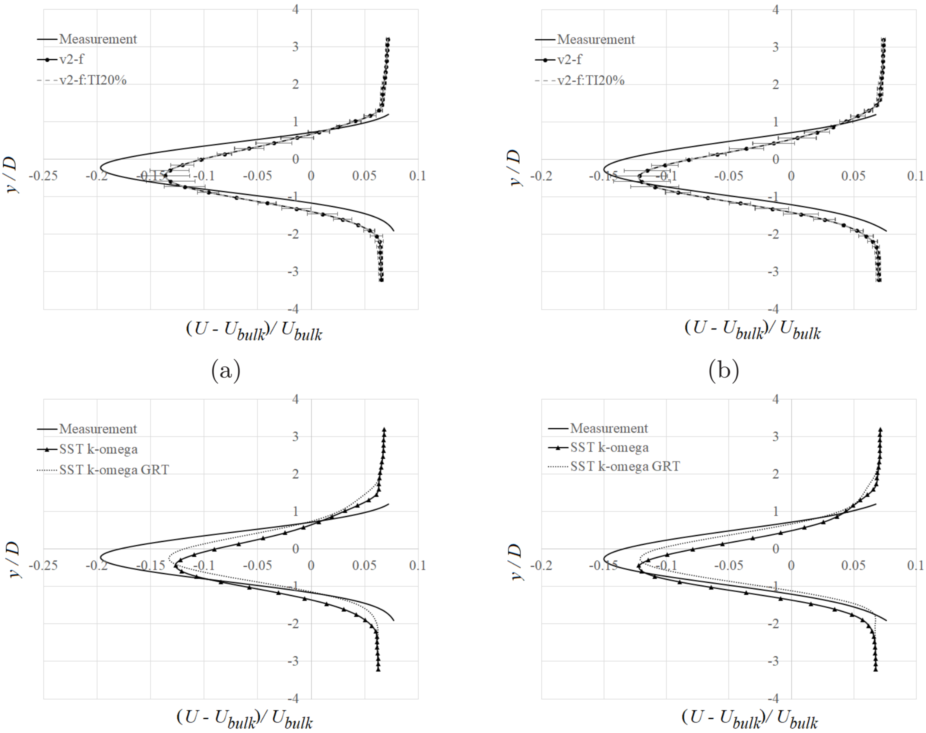

(a) (b)

(c) (d)

Figure II.4: Velocity profiles downstream of the trailing edge for different models compared to experiment. In the left column (a and c) sampled at X=9.9D. In the right column (b and d) sampled at X=13.3D. The error bars represent one GCI to each direction.

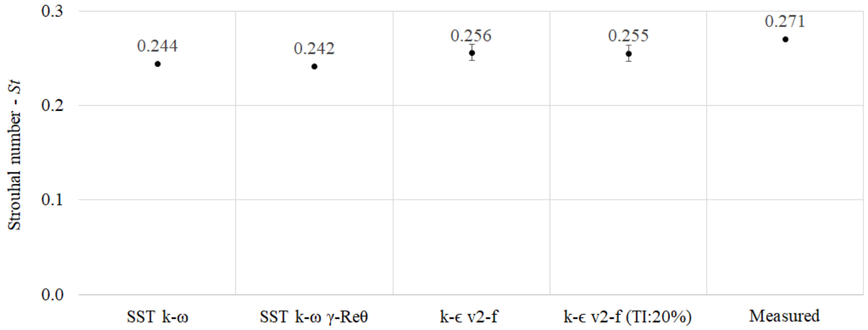

Figure II.5: Strouhal numbers obtained for all models on the medium grid.

intensity, has only a negligible effect on the velocity profile downstream of the trailing edge, though without a proper assessment of the test section turbulence levels and upstream velocity profile, this may still be incidental. Nevertheless, considering the sensitivity tests carried out with respect to the free stream turbulence intensity and transition, the results indicate that the v^2-f model does give at least as good results, or better, compared to the SST k-ω turbulence model for the present test case.

Acknowledgements. This work was supported with computational resources provided by UNINETT Sigma2. The measurement work previously presented was made with support from the HiFrancis project.

References

[1] Iaccarino, G., “Predictions of a Turbulent Separated Flow Using Commercial CFD Codes”, en, Journal of Fluids Engineering vol. 123, no. 4, 819 (2001).

[2] Durbin, P. A., “Separated flow computations with the $k-\epsilon-v^2$ model”, AIAA Journal vol. 33, no. 4, 659–664 (1995).

[3] Durbin, P. A. and Reif, B. A. P., *Statistical theory and modeling for turbulent flows*, 2nd ed. (John Wiley & Sons, West Sussex, United Kingdom, 2011).

[4] Sagmo, K. F., Tengs, E. O., Bergan, C. W., and Storli, P. T., “PIV measurements and CFD simulations of a hydrofoil at lock-in”, IOP Conference Series: Earth and Environmental Science vol. 240, 062006 (2019).

[5] Bergan, C., Solemslie, B., Østby, P., and Dahlhaug, O. G., “Hydrodynamic damping of a fluttering hydrofoil in high-speed flows”, International Journal of Fluid Machinery and Systems vol. 11, no. 2, 146–153 (2018).

[6] Siemens/CD-Adapco, *Starccm+ user guide*, Code version 12.02.010 (CD-adapco).

[7] Parneix, S., Durbin, P. A., and Behnia, M., “Computation of 3-D Turbulent Boundary Layers Using the V2f Model”, en, Flow, Turbulence and Combustion vol. 60, 19–46.

[8] Menter, F. R., “Two-equation eddy-viscosity turbulence models for engineering applications”, AIAA journal vol. 32, no. 8, 1598–1605 (1994).

[9] Langtry, R. B. and Menter, F. R., “Correlation-based transition modeling for unstructured parallelized computational fluid dynamics codes”, AIAA Journal vol. 47, no. 12, 2894–2906 (2009).

[10] Langtry, R. B., “A correlation-based transition model using local variables for unstructured parallelized cfd codes”, PhD thesis (University of Stuttgart, May 2006).

[11] Malan, P., Suluksna, K., and Juntasaro, E., “Calibrating the $\gamma-Re_\theta$ Transistion Model for Commercial CFD”, the 47th AIAA Aerospaces Sciences Meeting, 10.2514/6.2009-1142 (2009).

[12] Durbin, P., “On the k-3 stagnation point anomaly”, en, International Journal of Heat and Fluid Flow vol. 17, no. 1, 89–90 (1996).

[13] Celik, I. B., Ghia, U., Roache, P. J., Freitas, C. J., Coleman, H., and Raad, P. E., “Procedure for Estimation and Reporting of Uncertainty Due to Discretization in CFD Applications”, Journal of Fluids Engineering vol. 130, no. 7, 078001–078001–4 (2008).

Paper III

Particle image velocimetry measurements in the vaneless space of a model Francis turbine under steady state operation

K. F. Sagmo[1], A. Mærlie [2] and [1]P.-T. Storli

Accepted for publication in *IOP Conference Series: Earth and Environmental Science* as part of the (postponed) 30th IAHR Symposium of Hydraulic Machinery and Systems.

Abstract

Two-dimensional, two component particle image velocimetry (PIV) measurements of the guide-vane wake and vaneless space for a high head Francis model turbine are presented. Measurements have been carried out with a fixed head and rotational speed for a set of guide-vane openings representative of part load, high load and best efficiency operating points. The measured trajectory and strength of the guide vane wake for the different operating points is discussed in conjunction with the periodic velocity oscillations . It is hoped that the present measurements will aid in further analysis as well as provide an additional set of data for validation of numerical analyses.

III.1 Introduction

Intermittent renewable energy sources, such as solar and wind power, has become increasingly widespread in recent years due to their promising potential of mitigating climate change by replacing fossil fuels [1]. This increase in intermittent energy sources into the global electrical power grid has raised questions related to grid stability, energy supply and demand, and so called integration costs[2, 3]. Unlike solar and wind power, hydropower is not strictly dependent on the weather conditions and offers more continuous power delivery while maintaining high energy conversion rates [4]. In response to the increase of intermittent energy sources in the power grid, hydraulic turbines such as the Francis turbine, are expected to be operated at off-design conditions more

---

[1] Waterpower Laboratory, Norwegian University of Science and Technology, Alfred Getz Vei 4, 7491 Trondheim, Norway.

[2]

frequently [5]. This causes the need for a thorough understanding of the fluid flow inside a Francis turbine at different operating conditions.

Several of the undesirable phenomena in medium to high load Francis turbines have been linked to the rotor stator interaction (RSI)[5–7] and in general terms the flow in the vaneless space can be said to mediate this interaction[8]. While many numerical studies of the velocity field in the vaneless space of Francis turbines have been published (e.g.[9, 10]), fewer public experimental studies are known to the authors. One recent study that included both numerical and experimental investigations of the flow in the vaneless space of a low specific speed pump turbine was conducted by Hasamatuchi[11].

The turbine test rig at the Waterpower Laboratory at NTNU has been modified for optical access to allow for particle image velocimetry (PIV) measurements in the vaneless space. The Francis-99 turbine, on which the measurements have been carried out, has been part of the both the Francis-99 and HiFrancis workshop series and the turbine geometry is open to the public[12]. Together with previously published measurement data of the turbine efficiency hill chart[13], pressure pulsation amplitudes[14] and draft tube flow velocities[15, 16], the current measurements may serve as a complementary data set for comparison against numerical analyses of the same turbine.

III.2 Experimental setup and methods

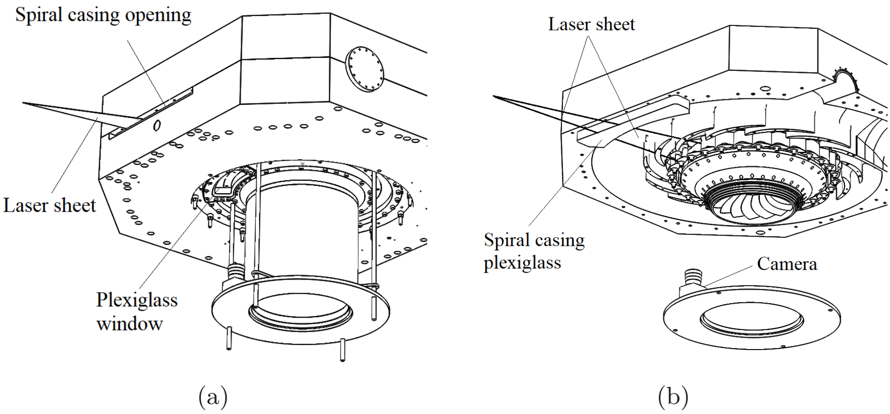

(a) (b)

Figure III.1: (a); Overview of the experimental setup. (b); View of setup with lower half of spiral casing removed.

The overall experimental setup is illustrated in figure III.1. A Photron MiniUX 100 digital CMOS high speed camera was used for image capture, while a dual cavity Litron LDY 301 PIV laser was used for illumination. Optical access was granted by a set of plexi-glass windows, as well as plexi-glass stay-vanes and guide-vanes. The two-dimensional (2D), two component velocity field in the vane-less space was obtained by positioning the camera as illustrated with an orientation perpendicular to the laser sheets coming in from the side of the spiral casing.

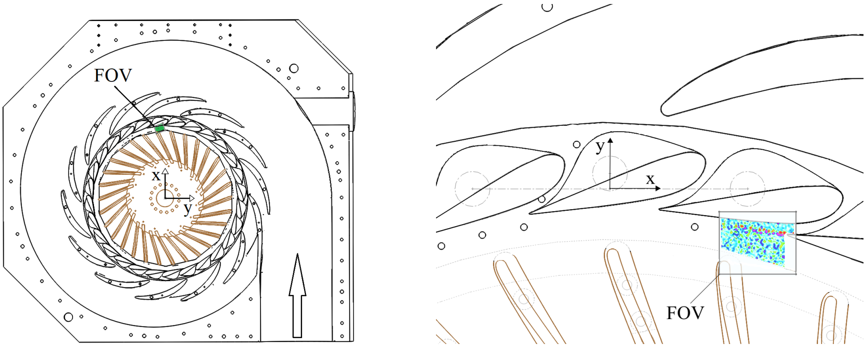

(a) (b)

Figure III.2: Location of field of view (FOV) with respect to the global turbine frame of reference, illustrated in view (a). In view (b); closer view of the FOV and orientation of the local reference frame.

III.2.1 Location of the measurement plane in the turbine

The position and reference frame orientation of the full resolution field of view (FOV) with respect to the turbine rotational axis are illustrated in figure III.2(a)-(b). As can be seen, the region of interest was the wake of the guide-vane, leading into the runner. Although a group of guide-vanes adjacent to the measurement area were of plexi-glass material for optical access, the measured wake was of a standard, stainless steel guide-vane, with a trailing edge thickness, d, measured to about 1.3 ± 0.1 mm. An enlarged camera image also indicating the full resolution FOV is illustrated in figure III.3(a), while figure III.3(b) shows a photo with the calibration plate installed. The images further serve to show the leading and trailing edges of the plexi-glass guide-vanes working as diverging and convergent lenses, creating gaps in the illuminating laser plane outside the FOV. Without optical index matching, this inherently limited the options of suitable FOV positions, but the current setup was deemed sufficient for the purpose of the measurements. Note that the calibration grid does not cover the complete guide vane passage, and consequently the uncovered parts of the measured vector fields later presented are deemed uncertain.

III.2.2 Turbine operating parameters

All tests were conducted with the Francis-99 model turbine operating in steady state, for an average head of 11.97±0.036 mWc with the runner rotating at 333.1±0.52 rpm across all operating points. Measurements included guide-vane openings of 4° ;6.7° (part load, PL);10°(best efficiency point, BEP);12.4° and 14°(high load, HL). In order to test for statistical convergence and hysteresis,

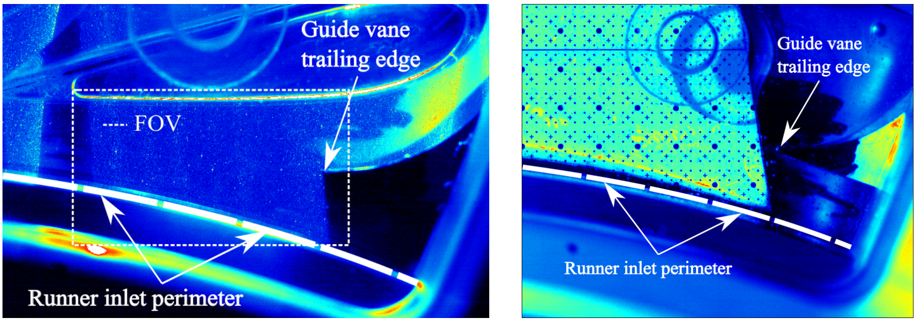

(a) (b)

Figure III.3: (a): An enlarged image indicating the approximate full resolution 1280 px x 1024 px field of view (FOV) utilised for the experiment by small white dashes. (b): Enlarged picture of the calibration plate positioning for overview.

two sets of measurements were taken at each guide vane angle starting from PL going to HL (ramp-up), as well as going from HL to PL (ramp-down). This gave a total of 4 image sets per guide-vane angle of operation.

III.2.3 PIV recording parameters

Table III.1: Summary of PIV recording parameters.

Resolution	1280 x 1024 pixels	1280 x 600 pixels
FOV	43.8 mm x 35.1 mm	43.8 mm x 20.5 mm
Vector field capture rate	0.2 kHz	4.166 kHz
Duration per vector set	21.84 s	1.79 s
Experimental velocity range	(3 - 12.4) m/s	
Image processing mode	Multi-pass cross-correlation	
Initial IA	64 x 64 pixels with 50% overlap	
Final IA	24 x 24 pixels with 50% overlap	
Mean tracer particle diameter	15.5 μm	
Tracer particle density	1.1 g/cm^3	

A summary of the PIV recording parameters are given in table III.1. All image acquisition and PIV evaluation was handled with LaVisions imaging software DaVis 8.4. The recorded images were in a flow field with an average velocity of around 9.8 m/s. In order to obtain a particle shift of 5-6 px between successive images for the optical setup and field of view later described, the time delay, dt, between two particle images were varied between 15-17μs. Each particle image pair was illuminated by separate light pulses from the dual cavity laser. Laser light sheet overlap was checked and found adequate by cross correlation of particle images in a nearly stationary fluid. The full resolution images at 1280 px x 1024 px used for the time-averaged velocity fields later presented lasted for 1.79 seconds. This corresponded to roughly 300 runner blade passing's, or about 10 runner rotations. The vector fields evaluated from the low resolution images at 1204 px x 600 px were used in the frequency analysis later presented, due to the higher acquisition rate. All measurements were taken at a horizontal plane lying at a z-position corresponding to a vertical span position in the guide-vane passage of approximately 28.3 mm ± 1 mm, measured from the lower guide vane passage wall. The thickness of the laser sheet itself was estimated to approximately 0.8 mm. The calibration of images were done with a 3'rd order polynomial mapping function, and the RMS fitting value obtained was 0.29 px with an average image scale of 29.2 px/mm.

The closed water loop was homogeneously seeded with tracer particles prior to conducting the measurements and average particle count was about 10 for the largest IA and about 5 for the smallest IA. Post processing of the evaluated vector fields with the universal outlier detection median filter proposed by Westerweel [17] showed only a negligible number of spurious vectors to be contained in the final vector field when the normalized residual threshold value for discarding a vector was set to 2. A set of vector fields were inspected for each of the operating points and the average cross correlation value of each vector field was generally found to be above 0.85. For the cross correlation evaluation DaVis 8.4 uses a 3 point Gaussian fit to estimate particle displacement and the observed particle size estimated by visual inspection was about 2-4 px for the results later presented. As such, this method should give sub-pixel accuracy in the estimation of the particle displacement[18, 19], and hence vector evaluation, thus minimizing any peak-locking effect. As a check the probability density function of the velocity components was inspected and the degree of peak-locking was found to be acceptable.

Further an uncertainty estimation for the instantaneous velocity fields was checked according to the method due to Wienke [20]. Overall, for the results later presented, this gave a maximum uncertainty in the order of 10% while generally the uncertainty observed to be in the range of 4%-6% relative to the approximate average velocity in the vaneless space. Finally, in order to estimate the uncertainty in the time-averaged velocity field magnitude, $<|\tilde{V}|>$, the following relation was applied [18];

$$<|\tilde{V}|> = \frac{\sigma_{|V|}}{\sqrt{N_{eff}}}. \tag{III.1}$$

Here, $\sigma_{|V|}$ denotes the standard deviation in $|V|$ evaluated across all samples N of a measurement series. N_{eff} denotes the effective number of independent samples of $|V|$, evaluated through computation of the auto-correlation of the time-series of the instantaneous velocity amplitudes. In the case of the samples being completely independent, the number N_{eff} approaches the number of total samples N.

III.2.4 Frequency analysis and energy maps as a function of frequency range

In an effort to look at the dominant frequencies in the measured velocity fields, the power spectra for both the x- and -y velocity components have been investigated. The spectra were obtained through discrete fourier transforms of the velocity fields, after a subtraction of the average velocity field for each operating point. A hanning weight function was used for windowing the data. Further, the power spectra profiles presented are spectrum averages over a 3x3 vector area around the specified points. Finally, energy fraction (EF), maps were plotted by evaluating the kinetic energy fraction on a per point basis;

$$EF = \frac{E_{f_1 - f_2}}{E_{total}}, \tag{III.2}$$

where $E_{f_1-f_2}$ denotes the sum of energy contained within the frequency range f_1 to f_2, and E_{total} is the total energy contained in the complete spectrum at a given point.

III.3 Results and discussion

III.3.1 Instantaneous velocity field and frequency analysis

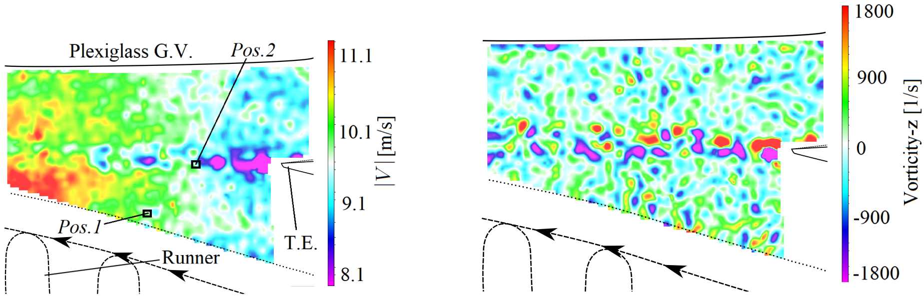

(a) (b)

Figure III.4: The resulting 2D velocity field from PIV measurements, colored according to (a); absolute velocity and (b); vorticity-z. $Pos.1$ and $Pos.2$ mark the approximate cross stream velocity sampling positions. T.E. denotes the guide-vane trailing edge position.

The instantaneous velocity field for best efficiency point operation is shown in figure III.4(a). The wake of the guide vane is clearly visible, and the width of the velocity deficit zone near the trailing edge corresponds well with a trailing edge thickness of about 1.3 mm, though this is more clear in the time-averaged velocity profiles later presented. Figure III.4(b) shows the vector field colored according to vorticity. Though clearly turbulent, a distinct vortex shedding street is visible, with alternating vortexes extending several trailing edge diameters downstream.

Also indicated in figure III.4(a) are two positions, $Pos.1$ and $Pos.2$, from which the frequency spectra presented in figure III.5 were obtained. The y-component, which is nearly perpendicular to the mean flow direction for the given guide-vane angle, was sampled with a reduced field of view for an increased

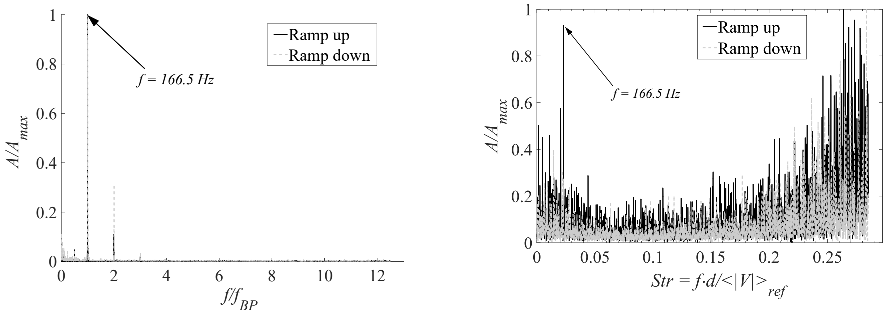

(a) (b)

Figure III.5: Amplitude spectra for different measurement samples obtained through FFT of the velocity component V_2 along the y-axis. from the calculated velocity fields. The samples in (a) are spectra obtained from *Pos*.1, while the samples in (b) are obtained from *Pos*.2.

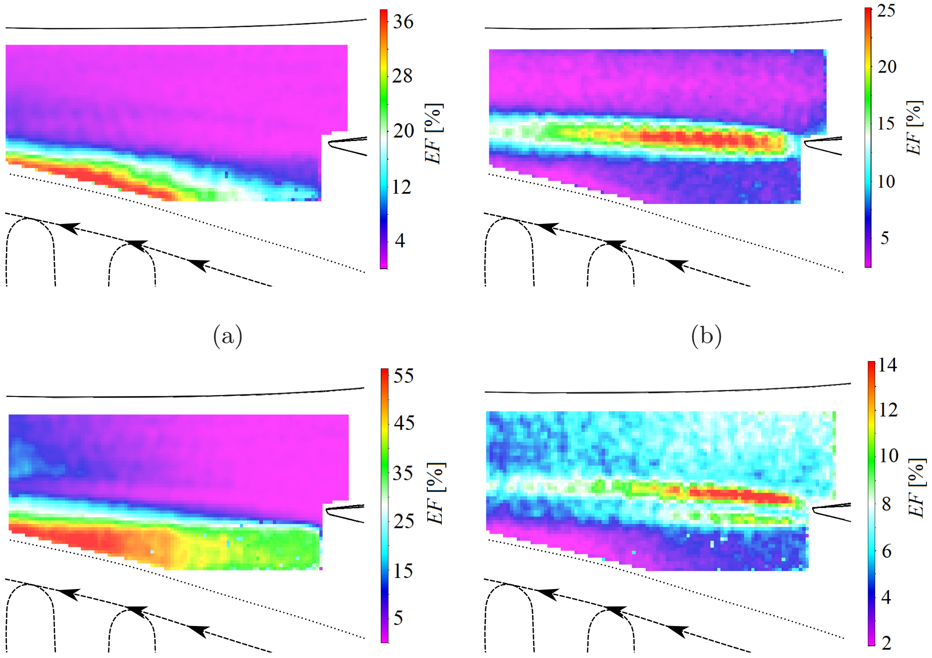

(a) (b)

(c) (d)

Figure III.6: Energy fraction in frequency ranges corresponding to (a) 165-169 Hz and (b) 1870-2070 Hz for the velocity component along the y-axis, followed by corresponding fields for the velocity component along x-axis in (c) and (d). Results for BEP.

image rate of 4.166 kHz. While the runner blade passing frequency, f_{BP}, of 166.5 Hz is present in both spectra, the spectrum obtained at $Pos.1$, close to the runner, shows the peak most clearly. The spectrum obtained at $Pos.2$, plotted in figure III.5(b), show what resembles a normal distribution of frequency peaks around a Strouhal number of roughly 0.27 or a range of 1870-2070 Hz. Here the trailing edge thickness and the local average velocity in the vicinity of the trailing edge was used for scaling the Strouhal number. The result is in good agreement with previous in-house measurements for shedding frequencies for a isolated hydrofoil in lock-off conditions[21], as well as measurements conducted by Heskestad and Olberts[22] for a similar trailing edge geometry. Further, one may argue that the broad range of peaks indicate no lock-in effect is present for the guide-vane investigated. In addition, the agreement between the two measurement sets indicate no marked hysteresis effects whether one is opening or closing the wicket gates.

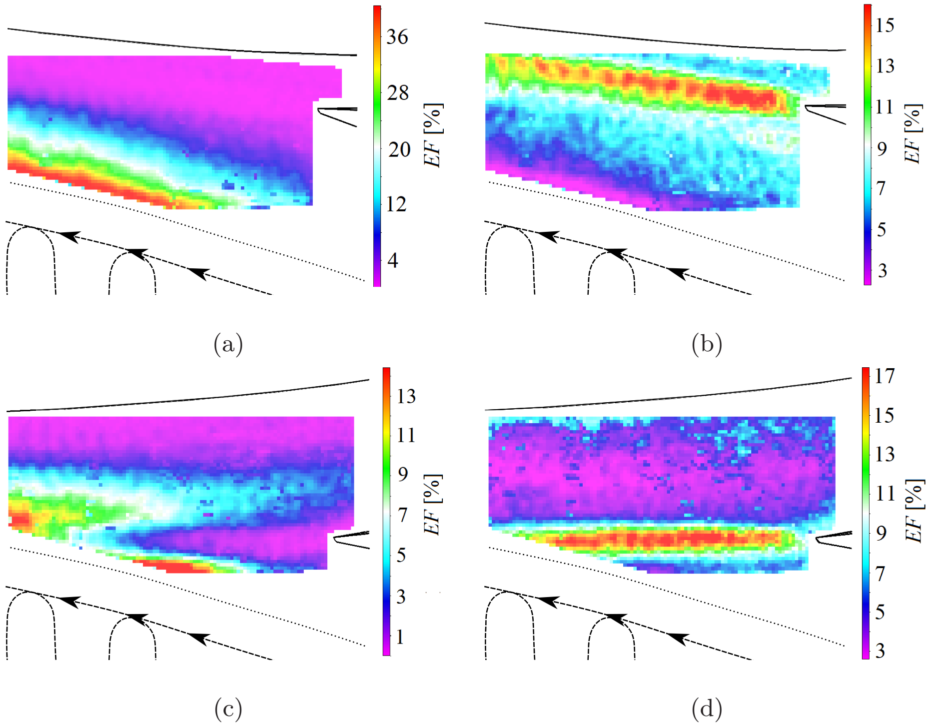

(a) (b) (c) (d)

Figure III.7: Energy fraction in frequency ranges corresponding to (a) 165-169 Hz, and (b) 1650-1850 Hz for velocity component along y-axis at PL operation. (c) and (d) give the corresponding fields for HL operation between frequency ranges of 165-169 Hz and 1844-2044 Hz, respectively.

Figure III.6 shows field plots for the energy fraction contained within the fluctuating velocity components along the x- and y-axes at BEP, evaluated according to equation III.2. The frequency ranges associated with the wake, figure III.6(b) and (d), and runner blade passing characteristic frequencies, figure III.6(a) and (c), were selected based upon the previously presented amplitude spectra. As is indicated by figure III.6(c), a relatively large amount of the fluctuating energy in the x-velocity component is associated with the runner blade passing frequency. From the velocity fields themselves it may seem that this energy content stems from a throttling effect occurring as the runner blade is passing close to the guide-vane. This periodic reduction in the cross section as seen by the fluid is enough to cause a significant pulsation in the velocity field, both radially and tangentially. While not explicit, this observation is inferred from the fluctuations along the x-and y-axis, which is oriented nearly tangentially and radially to the turbine's rotational frame of reference, respectively.

Analogously to figure III.6, figure III.7 show the same field plots for PL and HL operating points, though only for the velocity components along the y-axis. Figure III.7(a) show the energy fraction associated with the runner blade passing frequency, while figure III.7(b) show the energy fraction contained within the vortex shedding frequency range, both at PL operation. Figure III.7(c) and (d) show the corresponding fields for HL operation. Note that, in order to extract the appropriate range of frequencies associated with the vortex shedding, the second sampling position indicated in figure III.4 a) was moved to stay within the guide vane wake for these operating conditions. Interestingly, the effect of the runner blade passing is seen to be largely contained within the region circumferentially drawn by the guide-vane wake. The exception is for HL operation, as shown in figure III.7(c), where the interaction between the guide vane wake and the runner blade passing pulsations is more visible. Though not directly compared, this interaction implies that the kinetic energy contained within the wake of the guide vane, is similar in magnitude to the kinetic energy stemming from the apparent throttling effect, at least to some distance downstream of the guide vane trailing edge.

III.3.2 Time-averaged velocity fields

The following figures plot the time-averaged velocity fields for the range of guide-vane openings tested. An estimation of uncertainty in $< |V| >$, as quantified by equation III.1 gave a range of uncertainties everywhere less than 0.4 %, with the largest uncertainty associated with the trailing edge wake.

The time-averaged velocity field for BEP is given in figure III.8. In order to take a closer look at the guide-vane wake recovery velocity magnitude profiles were extracted from the lines located at x-positions, $x_1 - x_3$, as shown. Here, x_1 is located approximately $3.6d$ downstream of the trailing edge tip, with x_2 and x_3 being successively shifted $9.7d$ downstream. The results are plotted for measurements both at ramp up, and ramp down. Error-bars plotted for measurements during ramp-down represent the uncertainty estimate according to equation I.1, but with the field average value of the effective number of samples. The slight shift between the respective velocity profiles at ramp-up versus ramp-down measurements are readily explained by the uncertainty in the runner tip speed velocity, c_{tip}, used for normalization, as well as the uncertainty

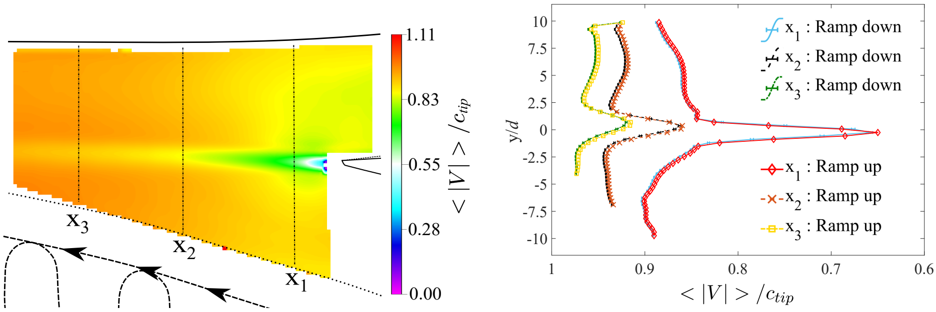

Figure III.8: Time-averaged velocity measurements for a guide-vane opening of $\alpha = 10°$. The three vertical lines at $x_1 - x_3$ marked on the left hand side illustrates the location for the velocity profiles plotted on the right.

in the guide-vane opening angle. At x_3, corresponding to approximately $23d$ downstream of the trailing edge tip, the wake is seen to be nearly recovered, with the maximum velocity deficit being around 5 %.

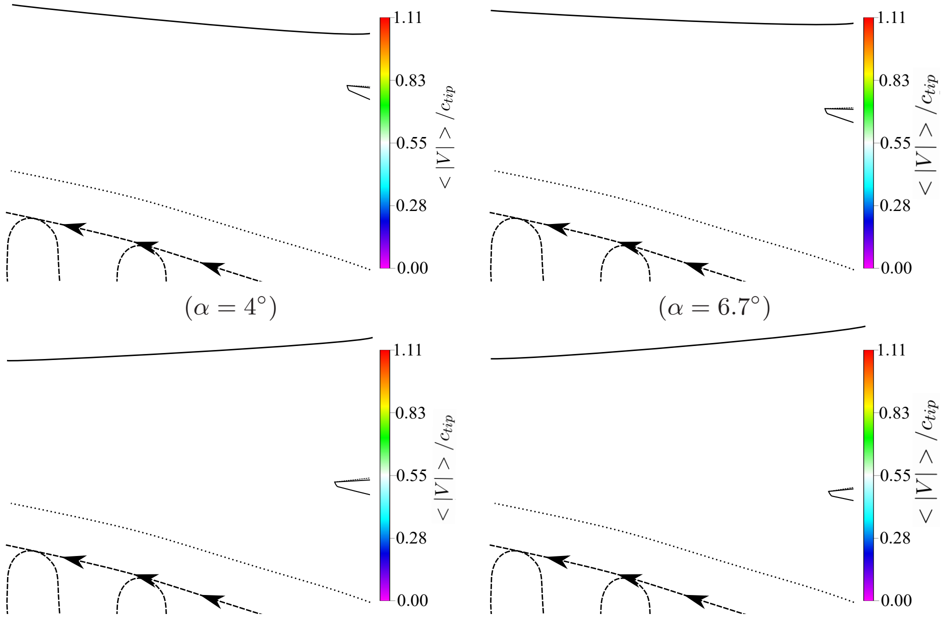

$(\alpha = 4°)$

$(\alpha = 6.7°)$

$(\alpha = 12.4°)$

$(\alpha = 14°)$

Figure III.9: Time average velocity fields indicating wake trajectory for increasing guide vane angles.

Figure III.9 show the remainder of the time-averaged velocity fields at increasing guide-vane openings. The guide-vane wake trajectory is generally observed to be closely aligned with the direction of the chord-line, as expected. Given the observed rate of recovery and trajectory for the different operating points, one may argue that the guide-vane wake will be largely recovered by the time it interacts with the runner leading edge, and so should induce only a small shift in the standing pressure field felt by the runner, for all operating points below a guide-vane opening angle of 12.4°. What the impact of the wake will be on the rotor-stator interaction effect is not clear however, since the complex interaction between vortices and inherent turbulence originating from the guide-vane could still play a part in for instance triggering boundary layer instabilities at the runner blades.

III.4 Conclusion and future work

2D PIV measurements of the vaneless space flow field in the Francis-99 model turbine have been performed for a range of operating conditions. For the present model turbine, the average vector fields obtained clearly indicate the trajectory of the guide-vane wakes and suggest that due to the rate of recovery, any shift in the standing pressure field felt by the runner due to the wakes should be small for all guide-vane opening angles below 12.4°. Even so, further quantification is needed for a proper conclusion.

A time-correlation for the PIV data with the runner blade position and pressure amplitudes in the channel would be interesting, to allow a more detailed investigation of the runner blade passing influence on the velocity field in the vane-less space. Further, transient measurements from very low guide vane angles up to PL, BEP and HL is suggested as part of future work.

Acknowledgements. Einar Agnalt, Magne Tveit Bolstad and Steinar Gilberg Straume is gratefully acknowledged for their assistance during the first set of measurements and help in design of the experimental setup. Thanks to Igor Iliev for valuable feedback during the preparation of the document. Also, the help of the skilled technicians at the Waterpower laboratory is acknowledged. This study was made possible, in part, by funding from the HiFrancis research project and the Research Council of Norway.

References

[1] IPCC, “Climate change 2014: mitigation of climate change: working group iii contribution to the ipcc fifth assessment report: energy systems”, in (Cambridge University Press, 2015), pp. 511–598.

[2] Acker, T. L., Robitaille, A., Holttinen, H., Piekutowski, M., and Tande, J. O. G., “Integration of wind and hydropower systems: results of iea wind task 24”, Wind Engineering vol. 36, no. 1, 1–17 (2012).

[3] Sorknæs, P., Andersen, A. N., Tang, J., and Strøm, S., “Market integration of wind power in electricity system balancing”, Energy Strategy Reviews vol. 1, no. 3, 174–180 (2013).

[4] Omar, E., Abu-Rub, H., and Blaabjerg, F., “Renewable energy resources: current status, future prospects and their enabling technology”, Renewable and Sustainable Energy Reviews vol. 39, 748–764 (2014).

[5] Goyal, R. and Gandhi, B. K., “Review of hydrodynamics instabilities in francis turbine during off-design and transient operations”, Renewable Energy vol. 116, 697–709 (2018).

[6] Seidel, U., Hübner, B., Löfflad, J., and Faigle, P., “Evaluation of RSI-induced stresses in francis runners”, IOP Conference Series: Earth and Environmental Science vol. 15, no. 5, 052010 (2012).

[7] Egusquiza, E., Valero, C., Huang, X., Jou, E., Guardo, A., and Rodriguez, C., “Failure investigation of a large pump-turbine runner”, Engineering Failure Analysis vol. 23, 27–34 (2012).

[8] Zuo, Z., Liu, S., Sun, Y., and Wu, Y., “Pressure fluctuations in the vaneless space of high-head pump-turbines—a review”, Renewable and Sustainable Energy Reviews vol. 41, 965–974 (2015).

[9] Li, Z., Wang, Z., Wei, X., and Qin, D., “Flow Similarity in the Rotor–Stator Interaction Affected Region in Prototype and Model Francis Pump-Turbines in Generating Mode”, Journal of Fluids Engineering vol. 138, no. 6, 061201, 10.1115/1.4032298 (2016).

[10] Trivedi, C., “Compressible Large Eddy Simulation of a Francis Turbine During Speed-No-Load: Rotor Stator Interaction and Inception of a Vortical Flow”, Journal of Engineering for Gas Turbines and Power vol. 140, no. 11, 112601, 10.1115/1.4039423 (2018).

[11] Hasmatuchi, V., “Hydrodynamics of a pump-turbine operating at off-design conditions in generating mode”, PhD thesis (IGM, Lausanne, 2012), p. 188.

[12] Trivedi, C., Gunnar Dahlhaug, O., Selbo Storli, P.-T., and Kristian Nielsen, T., “Francis-99 workshop 3: fluid structure interaction”, Journal of Physics: Conference Series vol. 1296, no. 1, 10.1088/1742-6596/1296/1/011001 (2019).

[13] Trivedi, C., Cervantes, M. J., Gandhi, B. K., and Dahlhaug, O. G., “Experimental and Numerical Studies for a High Head Francis Turbine at Several Operating Points”, Journal of Fluids Engineering vol. 135, no. 11, 111102, 10.1115/1.4024805 (2013).

[14] Agnalt, E., Solemslie, B. W., and Dahlhaug, O. G., “Onboard measurements of pressure pulsations in a low specific speed francis model runner”, IOP Conference Series: Earth and Environmental Science vol. 240, 022040 (2019).

[15] Bergan, C., Goyal, R., Cervantes, M. J., and Dahlhaug, O. G., “Experimental investigation of a high head model francis turbine during steady-state operation at off-design conditions”, IOP Conference Series: Earth and Environmental Science vol. 49, 062018 (2016).

[16] Sundstrom, L. R. J., Amiri, K., Bergan, C., Cervantes, M. J., and Dahlhaug, O. G., “LDA measurements in the francis-99 draft tube cone”, IOP Conference Series: Earth and Environmental Science vol. 22, no. 2, 022012 (2014).

[17] Westerweel, J. and Scarano, F., "Universal outlier detection for PIV data", Experiments in Fluids vol. 39, no. 6, 1096–1100 (2005).

[18] LaVision GmbH, *Lavision software davis 8.4 product-manual, item-number: 1105xxx*, Document name: 1003001 DaVis D84.pdf, Feb. 2017.

[19] Raffel, M., Willert, C. E., Wereley, S., and Kompenhans, J., *Particle image velocimetry: a practical guide*, edited by Raffel, M., 3'rd ed (Springer, Heidelberg ; New York, 2007).

[20] Wienke, B., "Piv uncertainty quantification from correlation statistics", Measurement Science And Technology vol. 26, no. 2, 074002 (2015).

[21] Sagmo, K. F., Tengs, E. O., Bergan, C. W., and Storli, P.-T. S., "Piv measurements and cfd simulations of a hydrofoil at lock-in", IOP Conf. Ser.: Earth Environ. Sci. vol. 240, no. 062006, 10.1088/1755-1315/240/6/062006 (2019).

[22] Heskestad, G. and Olberts, D. R., "Influence of Trailing-Edge Geometry on Hydraulic-Turbine-Blade Vibration Resulting From Vortex Excitation", Journal of Engineering for Power vol. 82, 103–09 (1960).

Paper IV

An experimental study regarding the effect of streamwise vorticity on trailing edge vortex induced vibrations of a hydrofoil

K. F. Sagmo[1] **and P.-T. Storli**[1]

To be submitted.

Abstract

A set of experiments testing the effect on vortex induced vibrations from three different trailing edge designs on a generic hydrofoil has been carried out at the Waterpower laboratory of NTNU. One of the designs are part of the Francis-99 workshop series on fluid-structure interaction and serves as a reference. The other two, a trailing edge with boundary layer vortex generators and a trailing edge with rounded serrations cut into the blade, both introduce stream-wise vorticity in the wake of the hydrofoil, as shown by particle image velocimetry measurements. The trailing edge of the hydrofoil is made exchangeable, so that a direct comparison of strain intensity levels measured with an embedded strain gauge bridge located close to the trailing edge can be made. It is shown that the vortex generators are effective at mitigating the lock-in state of resonance and significantly reduces the maximum strain intensity compared to the more conventional reference design.

IV.1 Introduction

The industrial implications of vortex induced vibrations are far ranging and a vast number of research has been devoted towards understanding the sometimes complex behaviour arising from this classic class of fluid-structure interaction problems. While it is well known that regular von Karman vortex shedding can lead to devastating vibrations during resonance, much effort is still dedicated towards its mitigation.

This study focuses on the effect that the introduction of stream-wise vorticity has on the resonance range for vortex induced vibrations. The two different

---

[1] Waterpower Laboratory, Norwegian University of Science and Technology, Alfred Getz Vei 4, 7491 Trondheim, Norway.

designs utilized are counter-rotating vortex generators embedded within the boundary layer close to the trailing edge, and a set of rounded serrations cut into the body of the trailing edge itself.

Both of the above mentioned passive flow control devices have been a topic of study for some time in the literature. In 1934, in a note to the Royal Aeronautical Society, Graham[1] stated that to "ignore birds as a guide" for aerodynamical improvements, would likely be a mistake. He then went on to highlight some of the then known peculiarities of silent flying Owl’s feathers, such as the leading edge comb, and the trailing edge fringe, or serrations.

Trailing edge serrations has had a significant research interest even in recent years. While much of the motivation has been directed towards flat plate trailing edge geometries allowing a reduction of self induced-broadband noise[2–5], some studies have also been concerned with so-called non-flat trailing edge serrations, as is the case in the present study. Chong et. al[6] showed that non-flat trailing edges cut into the body of the airfoil, could be used to decrease the span-wise coherence of the trailing edge vortex shedding compared to a blunt trailing edge. In a follow-up study Vathylakis and Chong[7] introduced porous media into the troughs of the serrations, and showed effective mitigation of the associated vortex shedding noise. Nedić and Vassillicos[8] studied the effect of adding fractal patterns to trailing edge serrations, and found that vortex shedding intensities could be decreased for certain chevron angles. Direct numerical simulations were carried out by Thomareis and Papadakis[9], giving a detailed view of the flow in the trough of the serrations.

Though typically used for passive control of premature boundary layer separation[10], Kuethe[11] showed at an early stage that vortex generators, or more generally, wall mounted devices introducing streamwise vorticity in the boundary layer, could be used to reduce trailing edge noise levels associated with regular von Karman vortex shedding. In addition, Tao et. al[12] recently showed that vortex generators can be used to suppress vortex shedding induced vibrations for a cylinder.

IV.2 Experimental Setup

IV.2.1 Overview

An overview of the test section geometry and experimental setup is given in Figure IV.1. A circular channel with a radius of 0.15 m leads up to a convergent section before entering a square channel constituting the test section. The test section itself is of length $L = 1.5$ m, and has a height and width of 0.15 m. We denote the channel half height, H=0.075 m. In order to measure the pressure drop across the test section, static pressure taps were sampled upstream, p_1, and downstream, p_2. The distance across the the sampling of static pressures is denoted L_{dp} and is equal to 6.67 m. The static pressures at both p_1 and p_2 was averaged over 4 circumferential pressure taps, and the pressure drop measured using a Fuji Electric differential pressure transducer. The channel bulk velocity, U_{bulk} was derived from volumetric flow rate measurements using an

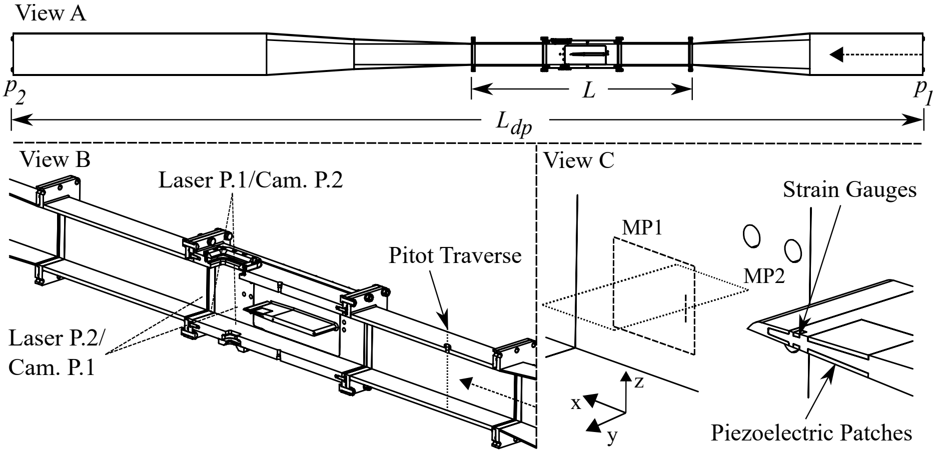

Figure IV.1: An overview of the experimental setup with three levels of increasing magnification from view A to C.

electromagnetic flow-meter located downstream the sampling point of p_2 (not shown). The flow-meter was calibrated using a weighing tank. In view B, the position of the high speed CMOS camera and the sheet optics for the laser light source used for the PIV system is indicated. Note that for the two perpendicular measurement planes, MP1 and MP2, illustrated in View C, the camera and sheet optics locations are interchanged. The orientation of the chosen coordinate system is also indicated, though offset. We choose the origin such that x=0 at the trailing edge, and y=0, z=0 at the test section center-line.

In addition, for the trailing edge with the serrations and the trailing edge with the vortex generators (VGs) further measurements were made in offset planes, parallel to MP1, but shifted half a characteristic period relevant for the designs in the span-wise directions. Also shown in View C are the locations for the strain gauges as well as the piezo-electric patches embedded into the hydrofoil main body. The Kulite strain gauges were wired in a half bridge configuration, one at the top and another symmetrically placed at the bottom, with their orientation along the span direction. This allowed for a high degree of sensitivity towards bending motions of the blade. The piezoelectric patches, from PI Ceramics, also mounted at both top and bottom of the foil, were used for sinusoidal excitation of the blade, in order to measure natural frequencies of the foil. The layout of the strain gauges and the piezoelectric patches is an adaptation of an instrumented hydrofoil used in the Francis-99 workshop series on fluid structure interaction phenomena, described in more detail in the paper by Bergan et. al[13]. All sensor data, except from imaging, was aquired using 12 bit analog to digital modules from National Instruments (NI), and handled in NI LabView. All pressure sensors, including the ones later described, were calibrated using dead weight calibrators.

IV.2.2 Trailing edge designs and mounting

The three different trailing edge designs utilized in the study are shown in figure IV.2. A rounded blunt trailing edge tip serves as the reference. This trailing edge blends a 9 mm radius into a 45° cut, giving it a generic Donaldson type profile. The thickness of the trailing edge, h_{TE}, as indicated in figure IV.3 is 4.8 mm. This reference profile is the same hydrofoil profile as used in the Francis-99 FSI workshop and more details can be found in [13].

The design of the 'vane' type counter-rotating vortex generator pairs was largely based on the review by Lin[10] as well as the findings by Brandner and Walker[14] who investigated the performance of vortex generators in a hydrodynamic setting. For accuracy, the vortex generators themselves as well as the trailing edge was milled from one block of aluminium. A height, h_{VG}, of 1.92 mm was chosen, resulting in a height to boundary layer thickness ratio in the range of 0.5-0.6. Here the boundary layer thickness of about 3-4 mm at the corresponding chord-wise location was estimated by CFD at a channel flow rate of around 9 m/s [15, 16]. Further, the vortex generators had a length $b_2 = 5.75$ mm ($3h_{VG}$), a inner pair spacing of $b_0 = 2.9$ mm ($1.5h_{VG}$), a period between the vortex pairs of $b_0 = 11.62$ mm ($6h_{VG}$), and an inclination with respect to the stream-wise axis of $\psi = 20°$.

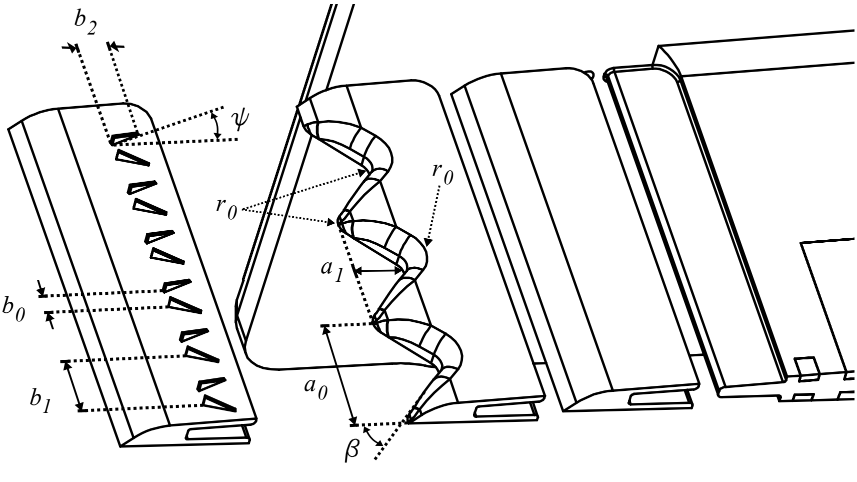

Figure IV.2: The different trailing edge tip designs and the tongue and grove joint connecting the tips to the main body of the hydrofoil. The drawing is cut at the symmetry plane, at 75 mm from the sidewall of the test section.

The generic serrated profile also shown in figure IV.2 was generated by keeping the original reference profile, but cutting a saw-tooth profile into the edge. In an effort to mitigate local concentration of stresses and consequent cracking during vibrations the troughs were then rounded, given a radius r_0= 3 mm. For completeness the peaks were given an equal radius. The rounding of the upper edge was done in an effort to minimize risk of cavitation while also blending well into the original, asymmetric profile. This left a design with a peak to peak distance, $a_0 = 23.4$ mm ($\approx 4.9 h_{TE}$), and a through depth, $a_1 = 9$ mm ($\approx 1.9 h_{TE}$). The resulting serration, or undulation angle β was about 45.8° in the xy - plane. Chong et. al. [6] reported for a non-flat, but sharp serrated trailing edge, that for β angles in the range of 7°-25° the narrow-band vortex shedding intensity decreased as the serration angle increased, a finding that supports using a large serration angle for suppressing the associated narrow-band vibrations. We re-iterate however that the present design should be viewed as generic since little data exists, to the authors knowledge, on the use of serrations for non-sharp trailing edges.

For accurately mounting the trailing edges a tapered tongue and groove joint was carefully machined so that the horizontally oriented surfaces would meet in a press fit. The trailing edges were secured with a two component epoxy glue produced by Valtron. The glue, AD4180-A/B (Shore D hardness ≈ 65) is a heat release system, allowing the trailing edges to be dismounted by heating the foil in a water bath to ≈ 95 degrees Celsius. This method of fitting the trailing edges allowed, after some surface treatment, a fully flush joint so as not to disturb the flow. The downside of such an approach is of course the risk of introducing some additional damping to the vibrations of the hydrofoil, due to the glue being less stiff than the aluminium (Certal AA 7122) used for both the trailing edges and the hydrofoil body. However, since the approach is identical for all the designs tested, the results should be comparable.

IV.2.3 Hydrofoil Profile

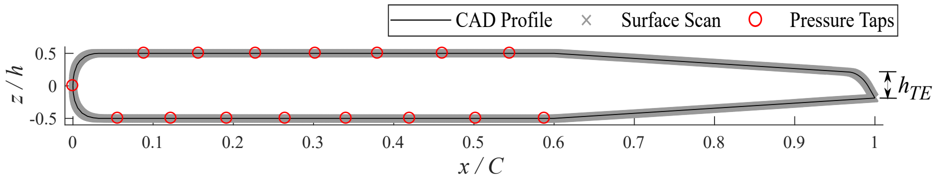

Figure IV.3: A comparison between the measured hydrofoil profile and the original CAD generated profile. The location of the pressure taps are also indicated, as well as the trailing edge thickness, h_{TE}. Note that the x and y axes are not to scale.

A plot comparing the original and the measured profile is shown in figure IV.3. The height of the foil, h, is 12 mm and it has a chord-length, C, of 250 mm. Given the scales of the experimental setup for the present case, particular attention is given to the accuracy of the machining and surface finish of the foil. The the fully assembled and surface treated hydrofoil was surface scanned with a Leitz PMM-C coordinate machine in order to check that the new hydrofoil with the exchangeable trailing edge tip retained the original profile design. After a closer inspection around the trailing edge only negligible differences were found. Surface roughness was also measured, conducted with a Mahr Perthometer

M2. From multiple samples, the profilometer gave an average surface roughness value, $R_a = 0.64\mu\text{m} \pm 0.76$, for an approximate 95% confidence interval. As per recommendation of Gersten [17], we estimate the equivalent technical roughness $k = 3.5 \cdot R_a$. Using, say, flat plate theory estimates for a turbulent boundary layer, as per White [18], we find for the vast majority of the Reynolds numbers investigated here a $k^+ < 4$ across the entire length of the blade, such that the surface may be considered hydraulically smooth.

IV.2.4 PIV recording parameters

The high speed, 2D, two velocity component PIV system utilized for the measurements is from LaVision. Details of the system and recording parameters are given in table IV.1.

Table IV.1: Summary of PIV recording parameters. Image acquisition and processing software, timing and synchronization hardware supplied from LaVision. Images was taken with a Photron FASTCAM Mini UX100 CMOS digital camera, fitted with a Tokina 100mm Macro Zoom lens, set to an aperture opening of f/2.8. The light source was a dual head Nd:YFL LDY300-PIV series laser from Litron Lasers.

Resolution	1280 x 1024 pixels	1280 x 600 pixels
FOV	47 mm x 37 mm	47 mm x 25 mm
Vector field capture rate	0.2 kHz / 2.441 kHz	3.551 kHz
Duration per vector set	21.84 s / 1.79 s	1.79 s
Experimental velocity range	(6 - 21) m/s	
Image processing mode	Adaptive multi-pass cross-correlation	
Initial IA	64 x 64 pixels with 50% overlap	
Final IA	32 x 32 pixels with 50% overlap	
Mean tracer particle diameter	13 μm	
Tracer particle density	1.1 g/cm^3	

As mentioned above, PIV measurements were conducted in 4 different planes in the aft of the hydrofoil; two perpendicular planes (MP1/MP2) and three parallel planes (MP1 and offset planes). Note that average numbers are given for the sizes of the field of views (FOV) in table IV.1 since the dimensions vary slightly between images captured in the horizontal and the vertical planes. The thickness of the laser sheet was measured to approximately 0.7 mm, such that the estimated uncertainty in the positioning of the image plane is estimated to ±0.35 mm.

Figure IV.4 shows an image of the hydrofoil fitted with the serrated trailing edge tip as well as a view of the image calibration target positioned for measurements in the horizontal measurement plane. An adaptive multi-pass interrogation area (IA) algorithm, described in detail by Wieneke and Pfeiffer[19], was used to process the images, with a final interrogation area size of 32 px x 32 px. The adaptive IA approach stretches the IA into a mildly elliptic shape in the direction of smaller velocity gradients, in an effort to capture coherent structures in the flow. Roughly 10 particles were located within the final interrogation area on average, as is generally recommended[20]. The tracer

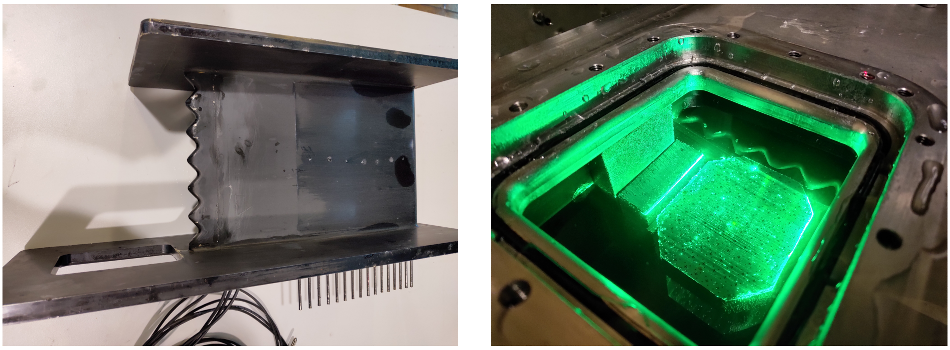

(a) (b)

Figure IV.4: Image a) shows the instrumented hydrofoil fitted with the serrated trailing edge design after surface treatment. Image b) shows the foil mounted in the test section with PIV calibration target set up for measuring in the horizontal, xy plane (MP2).

particles had an observed size of 3-4 pixels on average, while the typical range was 2-5 pixels. The timing between two subsequent laser pulses was adjusted in order to obtain an image pair particle shift of 5 pixels on average. Correlation peak location estimation was handled by a Gaussian three point estimator fit, giving sub-pixel accuracy in the calculated particle displacement. No significant degree of peak-locking was found upon inspection of the velocity probability density function. Random uncertainty in the instantaneous velocity fields, as estimated by the procedure described by Wieneke[21], was generally below 3% and typically around 1.7%. During processing of the vector fields this degree of uncertainty was subtracted from the Reynolds stresses later presented, in order to give a less biased estimate[22]. Finally, spurious vectors were evaluated by the universal outlier method described by Westerweel[23] and the final vector field estimated from the multi-pass IA algorithm was found to contain less than 0.1% replaced/interpolated outliers when a threshold residual of 3 over a 5x5 local vector neighbourhood was applied.

Estimates of the uncertainty in time-averaged variables were made from calculation of the standard error from a minimum of three repeated measurements, assuming a student-t distribution and given a 95% confidence level. In order to test for sensitivity of sampling frequency, image capture was conducted with both full resolution images and reduced resolution images for an increased image rate. Some data was also captured with a low image rate over longer sampling times, in order to obtain better statistical convergence. Where data samples were added to obtain a mean and standard deviation, the different data were given appropriate weights according to the approximate number of independent vector fields within each sample.

IV.2.5 Test section Velocity profile and turbulence

The test section velocity profile was measured with a wedge pitot-static probe from United Sensors at about two channel heights upstream of the hydrofoil. See figure IV.1, view B. The resulting profile, normalized against the channel bulk velocity, U_{bulk}, is plotted in figure IV.5. Note that for $|z/H| > 0.5$ the profile deviates significantly from symmetry, due to wall interaction effects of the probe and stem. The measurements are therefore only considered accurate within $|z/H| < 0.4$.

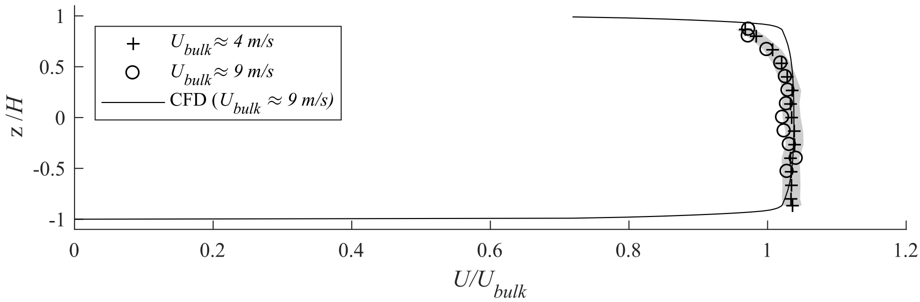

Figure IV.5: The test section velocity profile measured with a wedge pitot probe, normalized against the bulk velocity measured with the downstream flow meter.

For reference, CFD estimates from previous work by the authors[15] are also plotted, which were generated by RANS simulations assuming a 15 diameter development length upstream of the convergent section leading into the test section, which is also the case in the laboratory model. As can be seen, the measured profile is nearly flat, and a good match with CFD simulations for a bulk velocity of 4 m/s, while the profile appear slightly less developed for a bulk velocity of 9 m/s. The difference is only barely significant however. On average, the test section center-line velocity appear to be between $1.02U_{bulk}$ and $1.04U_{bulk}$. For simplicity, the bulk velocity is used as the reference velocity in the results presented later.

To give some indication of the turbulence intensity and the turbulent length scales present in the undisturbed flow in the test section a separate set of measurements were made with a FOV positioned in the top half of the measurement plane MP1. Several different IA sizes was tested during post processing of the particle images, but an adaptive multi-pass cross-correlation with a final IA of 24px by 24px was found to give the best trade-off between spatial attenuation and accuracy. Average stream-wise turbulence intensities, TI_{uu} plotted for a horizontal line at z=$0.25H$, outside the wake of the foil, along with measurement of the longitudinal auto correlation function with respect to a point x=$4.6h_{TE}$, z=$0.25H$, is included in the appendix. Overall, a turbulence intensity of 0.6% was found with respect to the bulk velocity, while the integral length scale, L_{uu}, was estimated to 7.6 mm, or about 5% of test section hydraulic diameter. The measurements were conducted for a bulk velocity of about 9 m/s, and a sliding average was subtracted from the vector fields in order to smooth out the low frequency oscillation present in the test section. These low frequency oscillations, on the timescale of several seconds typically only contributed to a standard deviation in stream-wise velocity on the order of 0.1% however, so that this bias is neglected for measurements of the turbulence in the hydrofoil wake later presented.

IV.3 Results and Discussion

IV.3.1 Natural Frequencies

The measured natural frequencies, f_n, of the first bending mode of the hydrofoil fitted with the tested trailing edges are presented in table IV.2. These frequency measurements, carried out in still water, are used for normalizing the results later presented. As can be seen, both the Reference trailing edge and the trailing edge with the vortex generators have natural frequencies of about 620 Hz, while the Serrated trailing edge yields a slightly higher frequency of 650 Hz. We note also that the peak to peak amplitudes of the measured strain is significantly higher for the serrated profile. As these variations are believed to be inherent to the mechanical design of the trailing edges, no correction to the strain-intensity levels later presented has been made.

Table IV.2: Natural frequencies, f_n and maximum peak to peak strain response amplitudes, A_{p2p}, of the hydrofoil in still water undergoing sinusoidal frequency sweep excitations of the piezoelectric patches for the different trailing edge designs tested. Strain amplitudes are normalized against the reference design. Natural frequency for the original Francis-99 hydrofoil is also included, to loosely indicate impact of the trailing edge glue joint on this parameter. 95% confidence intervals are estimated to ±1% and ±15% for the natural frequencies and strain response amplitudes, respectively.

	Reference	VG's	Serrations	Francis-99
f_n	624	620	650	649*
$A_{p2p}/A_{p2p-Ref}$	1	1.06	3.14	-

IV.3.2 Wake measurements - vertical xz planes

The following section described the flow characteristics as measured in the vertically oriented xz-planes. All measurements were conducted for a channel bulk velocity of roughly 9.1 m/s, which is below resonance for all the trailing edges tested. These measurements are meant as a study of the wake characteristics without the influence of the larger foil vibrations, which is presented in section IV.3.4. Throughout, we adopt the notation of the Reynolds decomposition such that $u = u' + U$, where u is the instantaneous velocity component, u' is the

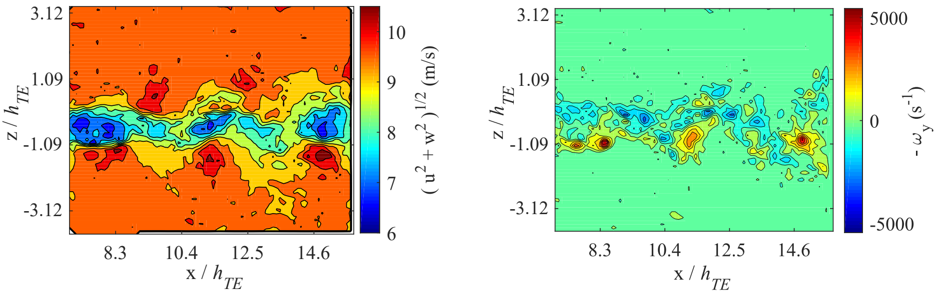

Figure IV.6: Measurements in the aft of the reference trailing edge. At left; contour plots of instantaneous velocity magnitude in the xz plane (MP1, symmetry plane). At right; corresponding contours of vorticity (negative).

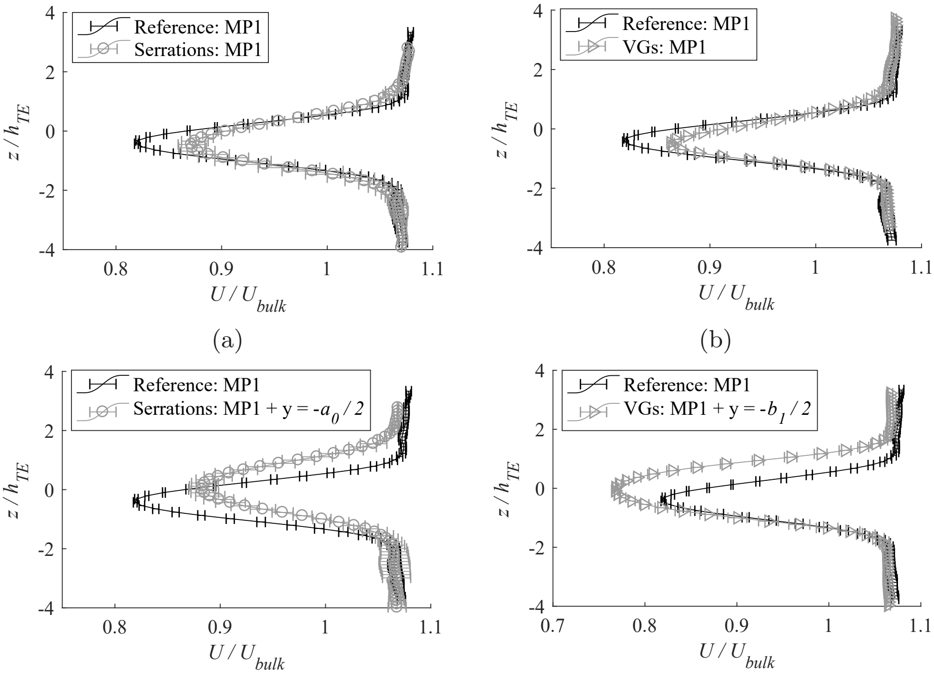

(a) (b) (c) (d)

Figure IV.7: Comparison of wake profiles for x=10.4·h_{TE}. a) and b) show the profile for the respective trailing edges measured at the vertical symmetry-plane, MP1. c) and d) show the profiles for the respective trailing edges at offset planes parallel to MP1, but shifted half a characteristic period in the negative y direction.

fluctuating velocity component and U is the time-averaged component. Further u, v and w are used to denote velocity components along the x, y, z axes, respectively.

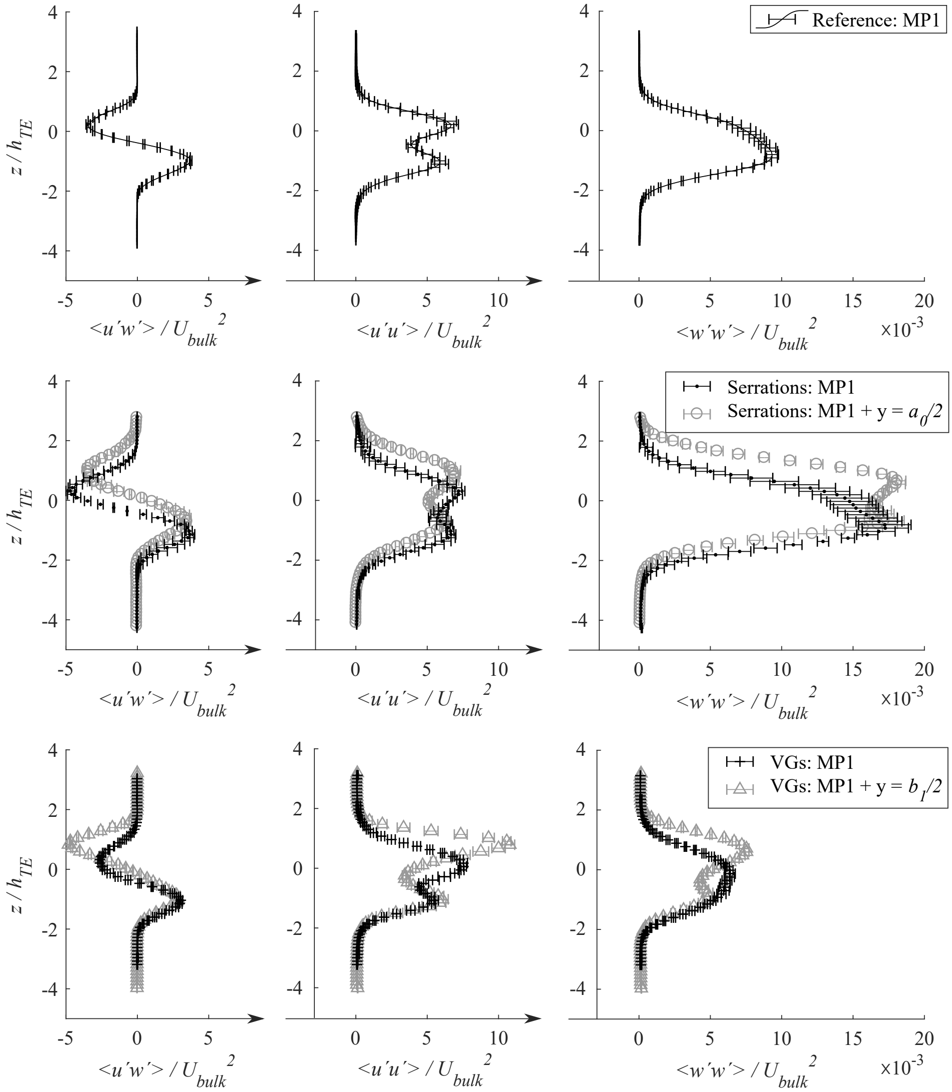

Figure IV.8: Comparison of normalized Reynolds stresses in the MP1 vertical symmetry plane as well as for the offset planes.

Measurements of the instantaneous flow velocity magnitude in the wake of the reference trailing edge is presented in figure IV.6. Iso-contours are indicated as a rough indication of the sizes of coherent structure and level of detail captured. Due to the 50% overlap of the interrogation areas the average vector to vector spacing is about 0.5 mm, though the size of the IA itself is on the order of 1 mm.

Figure IV.7 presents the time-averaged stream-wise velocity profiles at a downstream position of x=$10.4h_{TE}$, or 50 mm. Results are presented both for the symmetry plane (MP1) as well as parallel offset planes. The center wake is seen to be slightly shifted below the middle height of the test section, due to the asymmetrical trailing edge profiles. The offset plane measurements corresponds to a plane cutting the through of the serrations, and a plane cutting in between the closest spacing of the VG's, respectively. Note that the vortex generator trailing edge velocity profile displays a larger velocity deficit overall compared to the other two designs. The serrations on the other hand, appear to aid the momentum recovery in the stream-wise velocity components. Recently Thomareis and Papadakis[9] presented some direct numerical simulations for a similar serration design as studied here, though theirs was sharp. They noted that the velocity deficit downstream of the blunt troughs of the serrations was less than for downstream of peaks. Upon closer inspection, the same is actually true in the present study, although the difference is within the uncertainty of the measurements. Even so, a velocity deficit equal in magnitude downstream of the throughs as well as the peaks is somewhat surprising. It is assumed that the increased mixing stemming from the induced stream-wise vorticity aids the recovery of the velocity profile.

Normalized Reynolds stresses are compared in figure IV.8. Row by row the plot presents the shear, stream-wise and the cross-stream stresses, respectively. While the velocity deficit previously presented for the serrated trailing edge appear comparable or even less when compared to the reference design, turbulence levels are however increased. Most visibly the vertical velocity fluctuations are larger, both downstream of the peak and the through of the serrations, likely due to the narrow-band vortex shedding associated with the bluntness of the troughs. Interestingly, the opposite is true of the trailing edge with the VG's, where cross-stream velocity fluctuations are seen to decrease overall compared to the reference.

IV.3.3 Wake measurements - xy plane

Herein is described the span-wise velocity measurements (MP2) for both of the modified trailing edges. Figure IV.9 presents from top to bottom both the instantaneous velocity magnitude, as well as time-averaged velocities along x and y. The height of the measurement plane is located in the middle of the channel, at z=75 mm. The contour plots of the time-averaged stream-wise velocities agree well with the measurements in the vertically oriented planes, and display the expected periodicity.

The time-averaged velocity along y indicate the presence of the stream-wise vorticity, also showing the expected periodicity. At y=0, we observe a shift in the sign of the velocity component, due to the anti-symmetry condition set up by the design of the trailing edges. Depending on the height of the location of the apparent time-averaged vortex cores, these periodic shifts in the sign of the velocity component will correspond to clockwise and counter-clockwise, or vice versa, stream-wise vortexes when looking at the flow in a yz cross section plane.

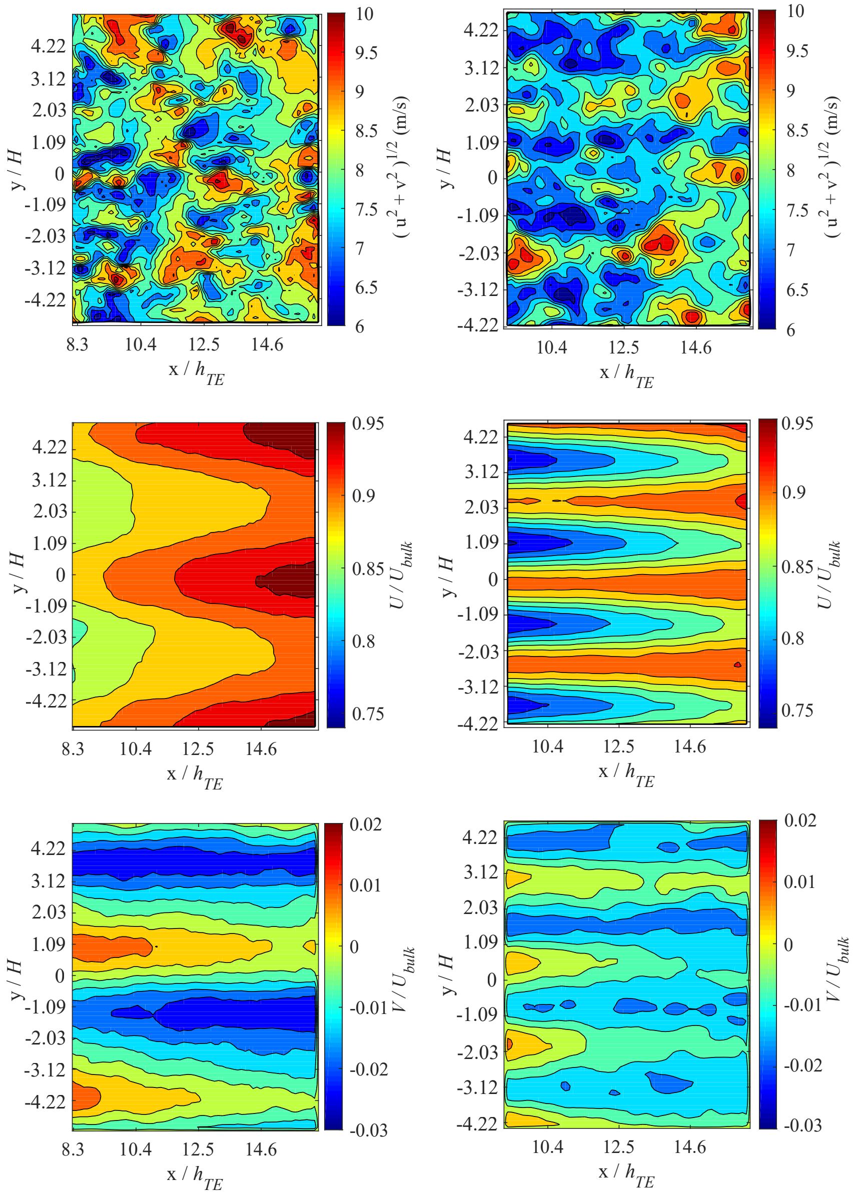

Figure IV.9: Velocity measurements for both the serrated trailing edge, in the left column, as well as the trailing edge fitted with the VGs, in the right column. From top to bottom the contour plots show the instantaneous velocity magnitude, the normalized time-averaged stream-wise velocity and the normalized time-averaged span-wise velocity, respectively.

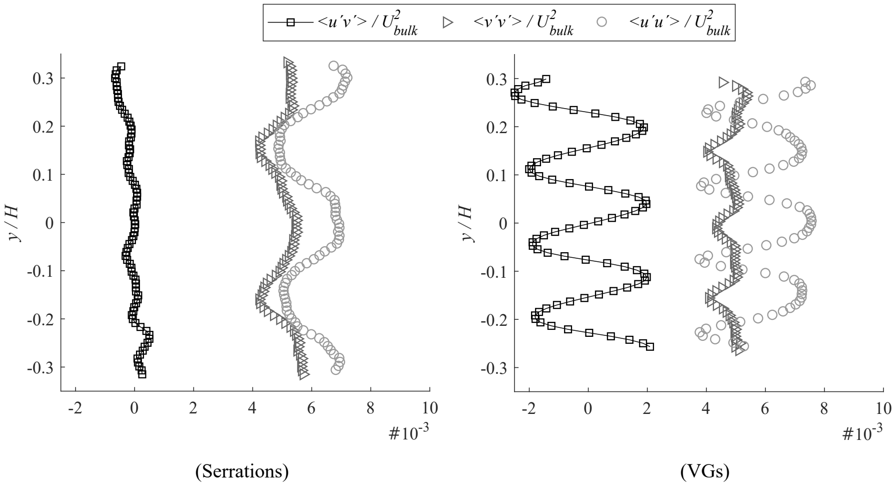

Figure IV.10: Reynolds stresses in the xy plane. Error bars, generally on the order of the size of the markers, are omitted for clarity.

The analogy is somewhat simplistic though, since the wake of non-flat serrated trailing edges have been shown to form intricate horseshoe vortexes[24], rather than steady stream wise vortexes, such as in the case of wing-tip vortices.

Figure IV.10 present the Reynolds stresses in the span-wise plane, extracted at a distance of x=10.4h_{TE} from the trailing edges. Again, we observe the expected periodicity and symmetry/anti-symmetry for a line about the mid-span, y=0. This is indicative of reasonable convergence in the statistics. The exception is the shear-stresses for the serrations, which are close to zero at this particular height of the measurement plane. In comparison the VGs give rise to strong free shear layers also in this plane, which may be taken as an indication of the relative stability of the stream-wise vortexes for this design. Finally longitudinal Reynolds stresses are seen to agree well with the measurements previously presented, at the intersection of MP1 and MP2.

IV.3.4 Strain response through resonance

This section focuses on the results relating the vortex shedding from the different trailing edges, and the mechanical vibrations measured with the strain gauges. First, figure IV.11 shows the power spectral density function of the vertical Reynolds stress component, against the Strouhal number, $St = fh_{TE}/U_{bulk}$, measured for the reference trailing edge tip at U_{bulk}=9.1 m/s. The sample was taken from a point corresponding to x=10.4h_{TE}, z=0. In order to extend the range of scales, this particular measurement was conducted with an image pair rate of 3.551 kHz at reduced resolution. However the shedding frequency was low enough that an image rate of 2.441 kHz was sufficient for most measurements in the following analysis. The Strouhal number, as indicated in the figure, is 0.28

for the reference trailing edge. Figure IV.12 shows the corresponding amplitude spectrum for the strain sensors, normalized against it's natural frequency as measured in stationary water, such that $f^* = f/f_n$. The strain signal is seen to contain both a broad peak corresponding to the vortex shedding, SP_1, as well as an excitation very close to it's natural frequency, SP_0. A small peak at about $f^* = 1.68$ is also observed, estimated to be the natural frequency of the second bending mode of the hydrofoil.

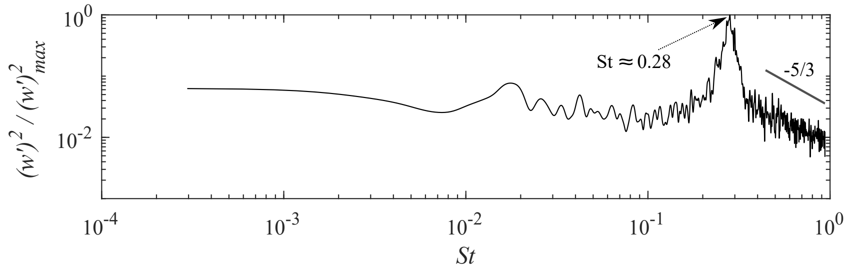

Figure IV.11: Power spectrum of fluctuating part of vertical velocity component in the wake of the reference trailing edge for a bulk velocity of 9,1 m/s. Slope of -5/3 exponent indicated for reference.

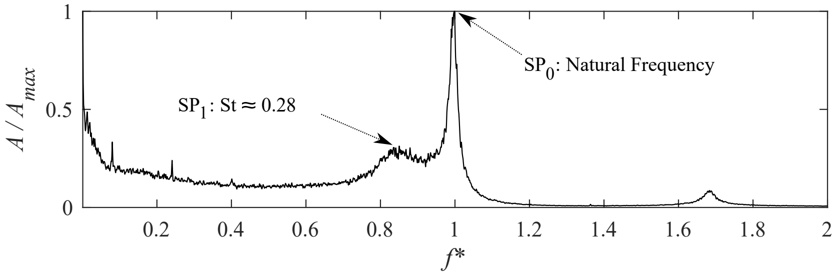

Figure IV.12: Amplitude spectrum of strain signal for bulk velocity of 9.1 m/s for the reference trailing edge. Normalized against natural frequency of the first bending mode measured in stationary water.

In the following presentation, the two peaks indicated in figure IV.12, SP_0 and SP_1 are tracked for increasing channel flow rates, along with shedding frequencies measured in the wake by PIV, denoted St_f. Further the flow rate, U^*, is normalized according to $U^* = U_{bulk}/(f_n \cdot h_{TE})$. In addition, the strain intensity, SI, is tracked, defined as the root mean square (rms) level of the strain fluctuations, normalized against the maximum rms level of the reference at resonance.

Figure IV.13 shows the vibrations of the reference trailing edge tip plotted against the other two designs tested. SI is plotted along the right vertical axis, while frequencies are plotted along the left axis. No excitations were made during these measurements, the only exciting force being the turbulent fluctuations and

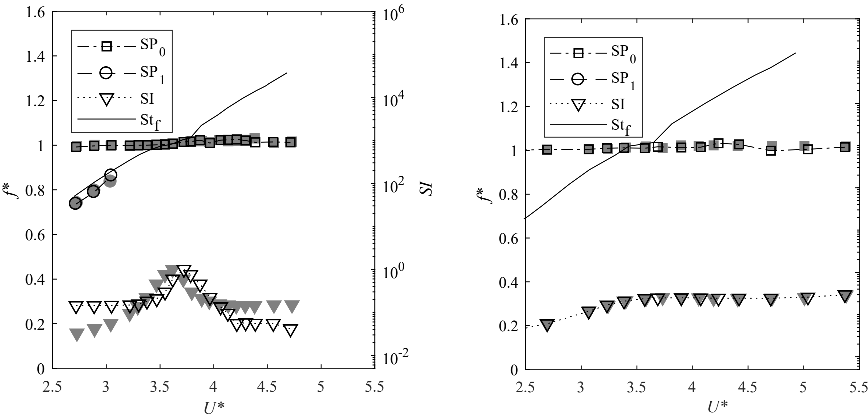

(Reference)

(VG's)

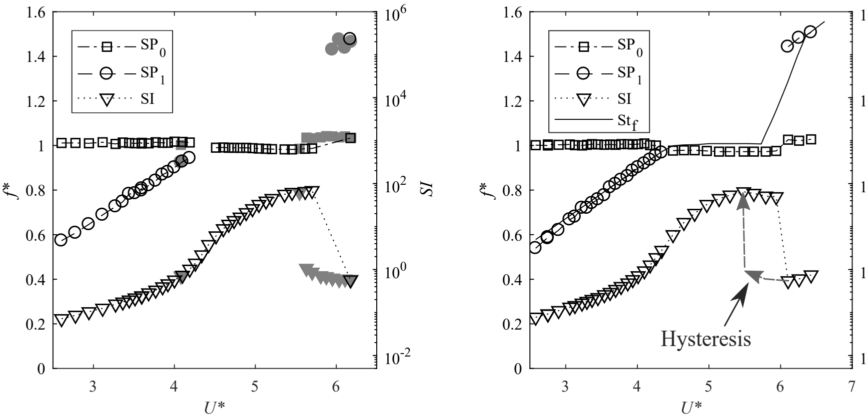

(Serrations - Set 1)

(Serrations - Set 2)

Figure IV.13: Normalized vortex shedding frequencies and main strain signal frequencies plotted along the left vertical axis vs normalized bulk velocity, U^*, for all trailing edges tested. Note that strain intensity, SI, is plotted along the right secondary axis on a log-scale. Grey filled markers represent measurements made with a decreasing flow rate (ramp-down) as opposed to increasing flow rate (ramp-up) for the open markers.

trailing edge vortex shedding from the hydrofoil itself.

The observed behaviour of the reference is as expected. Resonance is observed to occur at $U^* \approx 3.6$ where the measured vortex shedding, as indicated by St_f in the plot, overlaps with the foil natural frequency and maximum vibrations occur. Plots comparing the strain response of the reference with the identical Francis-99 hydrofoil, barring the glue-joint, is included in the appendix. Let us now, for the sake of discussion, choose an arbitrary SI threshold value of 80% relative to the maximum SI for the reference trailing edge design. With this value, we observe that the reference trailing edge enters a threshold exceeding range for normalized flow velocities, U^*, of around 3.5-3.8. Interestingly, the trailing edge with the VG's never exceeds this threshold value for the entire velocity range tested. In fact, the maximum SI level measured for this design is only about 20 % of the maximum level of the reference, and there is virtually no sign of any vortex induced resonant behaviour. The vortex shedding frequency, even though highly 3-dimensional for this case, is seen to increase nearly linearly straight through the natural frequency band of the foil. This is in opposition to the behaviour of both the reference trailing edge and the serrated trailing edge, which display clear resonant behaviour.

The bottom two plots in figure IV.13 show repeated measurements, set 1 and set 2, of the serrated trailing edge. Set 2 was made after a complete disassembly and subsequent re-assembly of the trailing edge. Hence, the two sets are an indicator of the repeatability of the fitting mechanism. The repeated measurements agree well, and both show that serrations shifts the resonance range, or lock-in, to higher channel velocities compared to the reference. The strain intensity is seen to reach 80% of the maximum level of the reference at about $U^* = 4$, resulting in a 10 % relative increase. This shift is largely explained by the decrease in the Strouhal number for this design, which is likely an effect of the increased bluntness caused by cutting the serrations into the body. Moving to higher discharges, the serrations enter a prolonged interference region, of large amplitudes. These large amplitudes are due in part to the structural change in the trailing edge, which was previously shown (table II.1) to lead to peak to peak amplitudes in strain of 3 times the size of the other two designs at resonance. In addition, it is natural to assume that the pressure fluctuations, and thereby the forcing function due to the vortex shedding, scales with the square of the velocity in the test section.

As is indicated in the plot for the second set, hysteresis in the vibrations was observed going trough lock-in for the serrated trailing edges. Upon visual inspection it was found that the large vibrations induced cavitation locally at the trailing for the velocity range above $U^* = 5$. The cavitation was entirely vibration triggered, and was only maintained for the largest vibrations, such that moving out of resonance the cavitation would immediately collapse, restoring a cavitation free wake even for increased discharges. It is likely this secondary resonance effect prolonged the range of the hysteresis. Unfortunately, the pressure rating of the test section would not allow further submergence of the tunnel, to further test the extent of the impact. Since these effects were constrained to such a small range however the overall results remain largely unaffected.

IV.3.5 Pressure loss

Pressure loss measurements for different channel discharges for the reference trailing edge is shown in figure IV.14. Here, the pressure loss coefficient is plotted against the test section bulk velocity Reynolds number. For clarity, a power curve fit is extracted from the data and compared against pressure loss measurements of the other two trailing edges in figure IV.15. Overall, though with a small

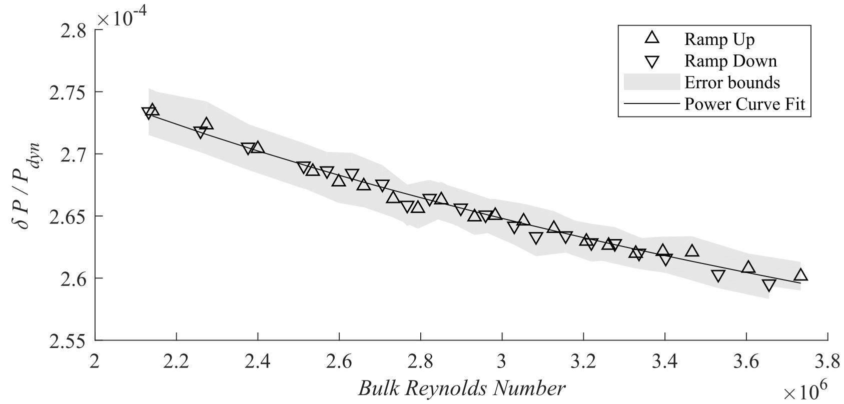

Figure IV.14: The reference design pressure loss coefficient across the entire test section, from the location of p_1 to p_2.

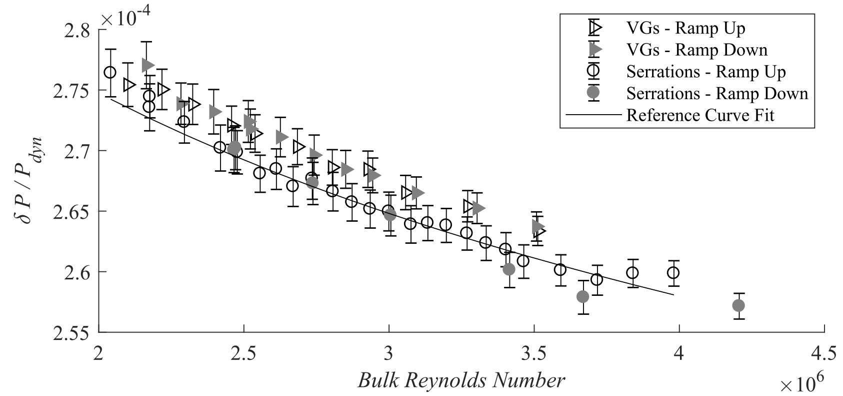

Figure IV.15: A comparison of the pressure loss coefficient measured for the different trailing edge designs.

margin, the VGs are seen to lead to an increased pressure loss, compared to the reference as well as the serrated trailing edge. This is as expected, and agrees well with the overall increased momentum deficit found in the wake of the VGs. Meanwhile the pressure loss from the serrated trailing edge is indistinguishable from the reference.

IV.4 Conclusion and further work

Three different trailing edge designs have been tested and the turbulent stresses in the wake at lock-off conditions as well as vibrations measured through vortex induced resonance has been presented. The results indicate that vortex generators significantly reduce vibrations at resonance conditions, though with a cost of increased drag for the design tested here. In opposition, the serrated trailing edge design tested here show no increase in drag, but results in large vibrations at resonance. An ideal design for engineering purposes would of course be one managing to combine the two effects.

Relative to the reference trailing edge, the vortex generators are seen to lead to an increase in the momentum deficit overall, but a dampening of the vertical velocity fluctuations. This is in contrast to the case of the serrated trailing edge, which leads to increased vertical velocity fluctuations, particularly down stream of the relatively blunt troughs. Further, a relatively strong span-wise alternation of the Reynolds shear stress is observed in the wake of the vortex generators. This could imply that the overall strength of the stream-wise vortexes is larger for the trailing edge fitted with the vortex generators, than for the serrated trailing edge in the present case. It is postulated that the potentially increased strength of the stream-wise vortexes aids in the span-wise de-correlation of the regular vortex shedding.

Regarding the increase in the vibrations observed for the serrations, it is unclear at this point, how much of the increase can be attributed to a change in the effective forcing function, i.e. pressure fluctuations, of the fluid, and how much is due to the structural change of the trailing edge. Further structural analysis of the individual designs both in stationary, as well as non-stationary water is needed. As the methodology shows some promise in the mitigation of vortex induced vibrations at resonance, a parametric study of the design approaches involved is suggested as part of future work.

Acknowledgements. The work of the lab-technicians is greatly acknowledged for assisting the measurements. In particular, thanks to Halvor Haukvik for his work in mounting the embedded sensors. Thanks also to Hasan Besirovic for suggesting the design of the vortex generators. These measurements were made with financial support from the HiFrancis project.

References

[1] Graham, R. R., “The silent flight of owls”, The Journal of the Royal Aeronautical Society vol. 38, no. 286, 837–843 (1934).

[2] Jones, L. E. and Sandberg, R. D., “Acoustic and hydrodynamic analysis of the flow around an aerofoil with trailing-edge serrations”, en, Journal of Fluid Mechanics vol. 706, 295–322 (2012).

[3] Avallone, F., Velden, W. C. P. van der, Ragni, D., and Casalino, D., “Noise reduction mechanisms of sawtooth and combed-sawtooth trailing-edge serrations”, en, Journal of Fluid Mechanics vol. 848, 560–591 (2018).

[4] Llorente, E. and Ragni, D., “Trailing-edge serrations effect on the performance of a wind turbine”, Renewable Energy vol. 147, 437–446 (2020).

[5] Moreau, D. J. and Doolan, C. J., “Noise-reduction mechanism of a flat-plate serrated trailing edge”, AIAA Journal vol. 51, no. 10, 2513–2522 (2013).

[6]Chong, T. P., Vathylakis, A., Joseph, P. F., and Gruber, M., “Self-Noise Produced by an Airfoil with Nonflat Plate Trailing-Edge Serrations”, en, AIAA Journal vol. 51, no. 11, 2665–2677 (2013).

[7]Vathylakis, A., Chong, T. P., and Joseph, P. F., “Poro-Serrated Trailing-Edge Devices for Airfoil Self-Noise Reduction”, en, AIAA Journal vol. 53, no. 11, 3379–3394 (2015).

[8]Nedić, J. and Vassilicos, J. C., “Vortex Shedding and Aerodynamic Performance of Airfoil with Multiscale Trailing-Edge Modifications”, en, AIAA Journal vol. 53, no. 11, 3240–3250 (2015).

[9]Thomareis, N. and Papadakis, G., “Effect of trailing edge shape on the separated flow characteristics around an airfoil at low reynolds number: a numerical study”, Physics of Fluids vol. 29, no. 1, 014101 (2017).

[10]Lin, J. C., “Review of research on low-profile vortex generators to control boundary-layer separation”, Progress in Aerospace Sciences vol. 38, no. 4, 389–420 (2002).

[11]Kuethe, A. M., “Effect of streamwise vortices on wake properties associated with sound generation.”, en, Journal of Aircraft vol. 9, no. 10, 715–719 (1972).

[12]Tao, S.-b., Tang, A.-p., Xin, D.-b., Liu, K.-t., and Zhang, H.-f., “Vortex-induced vibration suppression of a circular cylinder with vortex generators”, Shock and Vibration, 10.1155/2016/5298687 (2016).

[13]Bergan, C., Solemslie, B., Østby, P., and Dahlhaug, O. G., “Hydrodynamic damping of a fluttering hydrofoil in high-speed flows”, International Journal of Fluid Machinery and Systems vol. 11, no. 2, 146–153 (2018).

[14]Brandner, P. and Walker, G., “Hydrodynamic performance of a vortex generator”, Experimental Thermal and Fluid Science vol. 27, no. 5, 14th Australasian Fluid Mechanics Conference, 573–582 (2003).

[15]Sagmo, K. F. and Storli, P. T., “A test of the v^2-f k-ϵ turbulence model for the prediction of vortex shedding in the francis-99 hydrofoil test case”, Journal of Physics: Conference Series vol. 1296, 012004 (2019).

[16]Sagmo, K. F., Tengs, E. O., Bergan, C. W., and Storli, P. T., “PIV measurements and CFD simulations of a hydrofoil at lock-in”, IOP Conference Series: Earth and Environmental Science vol. 240, 062006 (2019).

[17]Gersten, K., *Fluid mechanics of flow metering* (Springer Berlin, Heidelberg, 2005).

[18]White, F. M., *Viscous fluid flow* (McGraw Hill, 2006).

[19]Wieneke, B. and Pfeiffer, K., “Adaptive PIV with variable interrogation window size and shape”, in 15th int symposium on applications of laser techniques to fluid mechanics (2010).

[20]Raffel, M., Willert, C. E., Wereley, S., and Kompenhans, J., *Particle image velocimetry: a practical guide*, edited by Raffel, M., 3’rd ed (Springer, Heidelberg ; New York, 2007).

[21] Wieneke, B., “PIV uncertainty quantification from correlation statistics”, Measurement Science and Technology vol. 26, no. 7, 074002 (2015).

[22] Sciacchitano, A. and Wieneke, B., “PIV uncertainty propagation”, Measurement Science and Technology vol. 27, no. 8, 084006 (2016).

[23] Westerweel, J. and Scarano, F., “Universal outlier detection for PIV data”, Experiments in Fluids vol. 39, no. 6, 1096–1100 (2005).

[24] Wang, J., Zhang, C., Wu, Z., Wharton, J., and Ren, L., “Numerical study on reduction of aerodynamic noise around an airfoil with biomimetic structures”, Journal of Sound and Vibration vol. 394, 46–58 (2017).

IV.5 Appendix

Turbulence characteristics measured by PIV outside the wake of the hydrofoil is presented in figure IV.16.

Figure IV.17 shows the vibrations of the reference trailing edge tip plotted against the Francis-99 hydrofoil. The comparison serves as indication of the structural impact of the glue joint on the otherwise identical hydrofoils. SI is plotted along the right vertical axis, while frequencies are plotted along the left axis. For this particular plot the SI for the Francis-99 hydrofoil is plotted against its own maximum, since different locations of the strain sensors mean that the strain levels are not directly comparable. Overall, we observe very similar results. The maximum to minimum levels of vibration do indicate some light damping present, which is as expected.

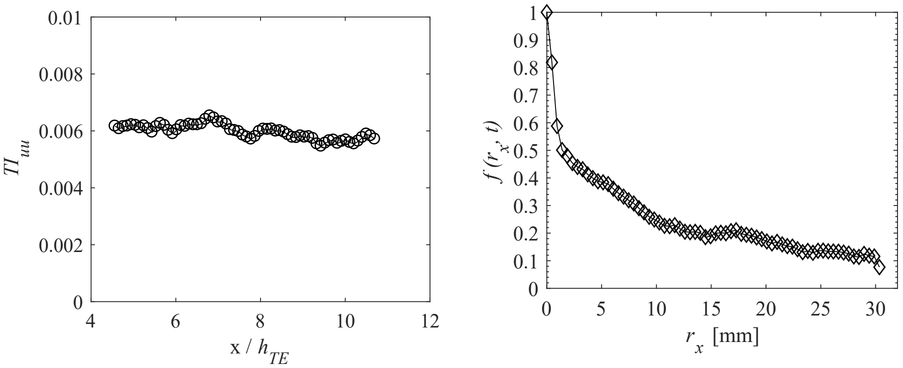

(a) (b)

Figure IV.16: In a); The stream-wise turbulence intensity, TI_{uu} with respect to the channel bulk velocity, U_{bulk} for a line at z= 94 mm. In b) the longitudinal auto-correlation function for the stream-wise velocity fluctuations, with respect to a point at x = 22 mm (x/$h_{TE} \approx 4.6$), z= 94 mm.

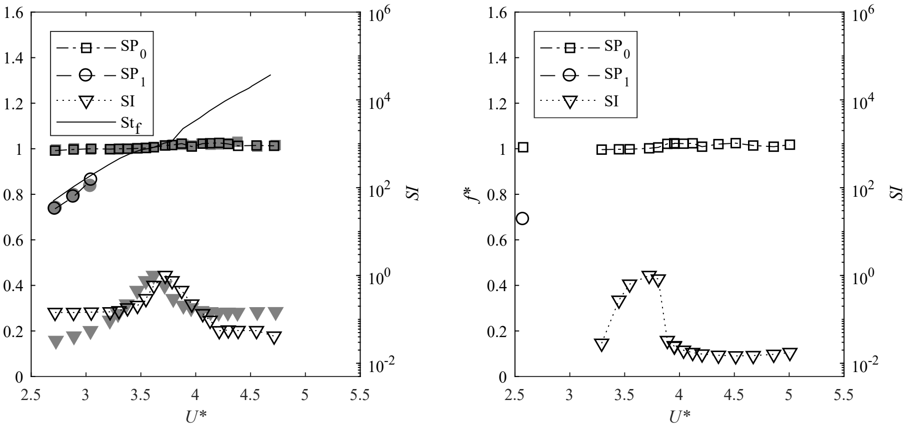

(Reference) (Francis-99)

Figure IV.17: Strain response to normalised bulk velocity, U^*, for the reference trailing edge designs. In (a) the foil with the exchangeable trailing edge, and (b) the Francis-99 hydrofoil.